Summer 2023

HF Radar: Shining a Light on Ocean Currents

Douglas Cahl

Recommended Citation

Cahl, D.(2023). *HF Radar: Shining a Light on Ocean Currents.* (Doctoral dissertation). Retrieved from https://scholarcommons.sc.edu/etd/7434

HF RADAR: SHINING A LIGHT ON OCEAN CURRENTS

by

Douglas Cahl

Bachelor of Science
Rutgers University, 2005

Masters of Science
University of Maine, 2012

Submitted in Partial Fulfillment of the Requirements

For the Degree of Doctor of Philosophy in

Geological Sciences

College of Arts and Sciences

University of South Carolina

2023

Accepted by:

George Voulgaris, Major Professor

Alexander Yankovsky, Committee Member

Michael Bizimis, Committee Member

Dana K. Savidge, Committee Member

Ann Vail, Dean of the Graduate School

DEDICATION

Dedicated to those have helped me on my path; my family (my parents, my brother, and my wife) and my advisors for my Masters' and PhD degrees, Charles T. Hess and George Voulgaris, respectively.

ACKNOWLEDGEMENTS

Here, I would like to acknowledge those that have made this work possible. Since as early as I can remember, my mother (Anne Cahl) would sit with me and teach me mathematics. My grandfather (Douglas Guest) would build me go-karts (while I was still a small child) where I could see all the moving parts. My father (Louis Cahl) did not object to when me and my brother would take apart out skateboards and build luges for the steep hills in my neighborhood. As I grew older, the math turned to physics and the go-karts turned to radio controlled cars, which also broke and required soldering to fix them. After we moved stateside, to New Jersey, I discovered that winters can be cold and long. Fortunately my father was a software engineer and so me and my brother had front row seats to early computers, video games (i.e., Test Drive, Doom), and the birth of the internet (except we didn't have AOL). My first programming experiences were some light modding of computer games, Duke Nukem, Quake, spending countless hours perfecting some scripts, etc.

This provided me with a solid foundation as my science career began, and after completing a degree in Physics from Rutgers, I moved on to complete a Masters' degree in physics at the University of Maine. Although I had always loved physics, I felt quite jaded with physics research after my Masters'. Perhaps I started remembering the waves crashing on the beaches near Cape Town, where I grew up. Or perhaps it was memories from the family vacations to Kasuga, also starting at waves, on the warmer Indian Ocean side of South Africa. Perhaps it was memories of a teenager spent at the Jersey Shore, or other beaches along the east coast. Or it could have even sailing on the frigid ocean off the coast of Maine when I had some free time during my Masters' studies. In any event, soon after I completed my Masters' degree, I found myself studying ocean waves at the University of South Carolina under George Voulgaris… and this time, I was excited!

As my PhD progressed, my love for the ocean seemed to only increase. My focus on ocean wave physics, and remote systems that exploit ocean wave physics to study the ocean itself, seems to have endless possibilities. Additionally, during the time spent pursuing my PhD, we have witnessed a revolution in ocean observational techniques, from gliders, autonomous boats, radars, satellites, etc. My advisor, George Voulgaris, not only encourages exploring these new systems, but to always explore new ideas. His love of physical oceanography is evident everyday I have been the Lab with him (the Coastal Processes and Sediment Dynamics Lab). In his Lab I have met not only great colleagues, but also great friends, which have brought new ideas to the science I study and new ideas about life as well.

My colleagues and friends, in no particular order; the late (and great) Nirnimesh Kumar, Timothy Nelson, Zaid Al-attabi, Xiaodong Wu, Conor Ofsthun, Alexander Frank and Dee Tianyi.

With the patience, understanding, and a lot of encouragement from my wife (Danielle Fahey), and with the guidance and mentorship of my advisor (George Voulgaris), my research has been both successful and enjoyable.

ABSTRACT

High Frequency (HF) radar systems are commonly used to estimate surface ocean currents over the coastal ocean. Their range depends on their operational frequency and low frequency systems (≤ 10 MHz) can reach distances up to 200 km from the coastline. These systems are used to estimate surface currents by measuring the phase speed of wind-driven waves and comparing the measured speed with that expected theoretically; deviations from the theoretical still-water phase speed are attributed to ocean surface currents. Although HF radar systems are considered a mature technology and the accuracy of the radar-derived surface current estimates is well studied, the theoretical phase speed of wind-driven waves and its dependence on sea state is still unresolved. Additionally, the algorithm widely used for estimating surface currents for compact cross loop systems, the most commonly used HF radar systems, has not been adopted for use with beamforming linear array systems. Lastly, although different large scale HF radar networks have publicly available data (e.g., HFRnet in the USA hosts measurements from over 100 operational HF radar sites), there is a lack of openly available toolsets (such as eddy identification routines) to exploit these data sets for ocean research.

A 7-month data set from two HF radar sites [CSW and GTN, located on the coastline surrounding Long Bay, SC (USA)] is used to assess the performance of three different algorithms for estimating surface ocean currents from two linear array HF radar

systems. The delay-and-sum beamforming algorithm, commonly used with beamforming systems, is compared with two direction finding algorithms, MUltiple Signal Classification (MUSIC) and direction finding using beamforming (Beamscan). While all three algorithms perform well along the radar boresight directions $(R^2 \approx 0.8)$, at $\approx 40°$ from their boresights, a baseline comparison between the two HF radar sites results in Beamforming performing poorly $(R^2 = 0.01)$, MUSIC $(R^2 = 0.37)$ performing better, while Beamscan $(R^2 = 0.76)$ performed well.

Although use of the Beamscan algorithm can increase the accuracy of HF radar measured ocean wave phase speeds at high angles from the radar boresight directions, conversion of this information to sea surface currents requires understanding the nature of this measurement. If the phase speed of the ocean waves the radar is measuring is modified by the sea state itself, we need to account for it. Recent efforts to quantify the phase speed dependency of wind driven waves in different sea states have led to the development of three approaches that describe the fraction of the Stokes drift contributing to wave phase speed modification: a nonlinear weighted and depth averaged Stokes drift (effective Stokes drift), the Stokes drift mostly from longer waves than the wave in question (filtered Stokes drift), and half the surface Stokes drift.

Using the same 7-month data set from the two HF radars in 2017, filtered Stokes drift shows the best correlation to the difference between the radar and in situ current measurements (accounting for >60% of the variance between the two) and it could be used to correct HF radar derived surface velocities. With that in mind, a neural network method is developed that uses the amplitude of the four Bragg peaks from these two radar systems to predict the filtered Stokes drift terms. The filtered Stokes drift prediction correlates to the difference between the radar and in situ measurements with $R^2 > 0.6$, reducing the difference between the in situ measurements and HF radar measurements significantly.

Finally, an optimized eddy identification routine (the winding-angle method) is presented for use with HF radar surface current data. Using data from the same two radar sites collected over 2013 the new method was utilized. It successfully identified over 1000 eddies with more than 200 of them being able to be tracked for periods in excess of 6 hours. All but 1 of the eddies tracked for over 48 hours were cyclonic upwelling eddies on the shelf break, representing the Charleston Gyre. We detail the passage of an anticyclonic eddy near the shelf moving equatorward and its associated momentum flux across the shelf break. We also find that the shelf break eddies contribute to momentum flux across the shelf and are most commonly spun up during times when wind is from the north, which induces Ekman transport in the preferred propagation direction of these anticyclonic shelf break eddies.

All codes developed as part of this dissertation described in the relevant chapters are publicly available at zenodo.org.

TABLE OF CONTENTS

LIST OF TABLES

LIST OF FIGURES

CHAPTER 1

INTRODUCTION

1.1 Background

HF radar systems estimate surface ocean currents by measuring the phase speed of ocean waves that have a wavelength equal to half the electromagnetic (EM) wavelength transmitted by the radar (Crombie, 1955), these ocean waves are known as Bragg waves. For monostatic radar systems (where the transmitter and receiver are located near each other) the EM waves transmitted by the radar towards the ocean are scattered from ocean Bragg waves travelling directly towards or away from the radar, so that the radar signal is scattered back to the receiving antennas, where this return signal (EM waves) is recorded (see figure 1.1).

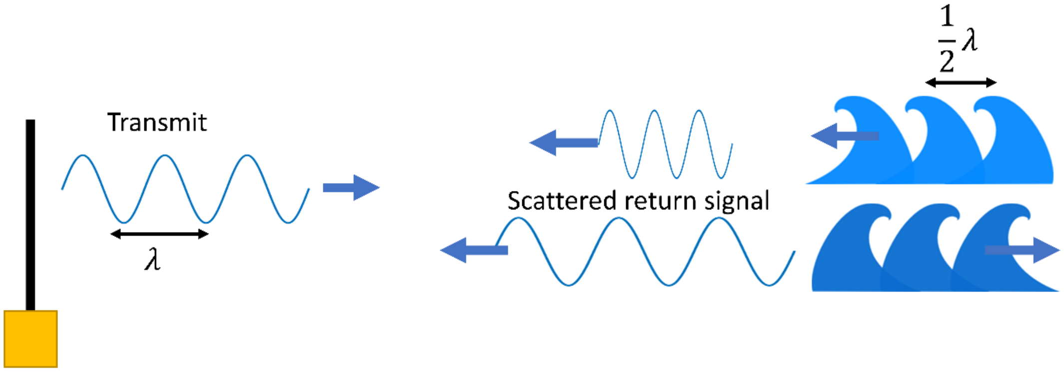

Figure 1.1: HF radar transmit signal scattering from ocean waves (Bragg waves) going towards or away from the radar. Note: figure is not to scale.

When the radar EM waves are scattered from the Bragg waves, they are Doppler shifted by the phase speed of the Bragg wave (see figure 1.1), which to a first approximation is determined by the surface current and the wavelength of the Bragg wave (e.g., Paduan and Washburn, 2013). The power spectrum of the received radar signal exhibits two large peaks at frequencies corresponding to the phase speed of the Bragg waves traveling directly towards or away from the radar system (figure 1.2). The frequency shift (Δf in figure 1.2) from the still-water Bragg frequency (marked as f_B in figure 1.2) is used to estimate the surface current (u) in the direction directly towards or away from the radar site as: $u = \Delta f \cdot \lambda_B$ where λ_B is the Bragg wave wavelength.

Scattering of the radar signal off multiple waves, results in the second-order spectrum (see lighter shaded regions in figure 1.2) which is used for sea state estimation (e.g., Alattabi et al., 2019). This dissertation focuses on surface current measurements from HF radars which is their primary use.

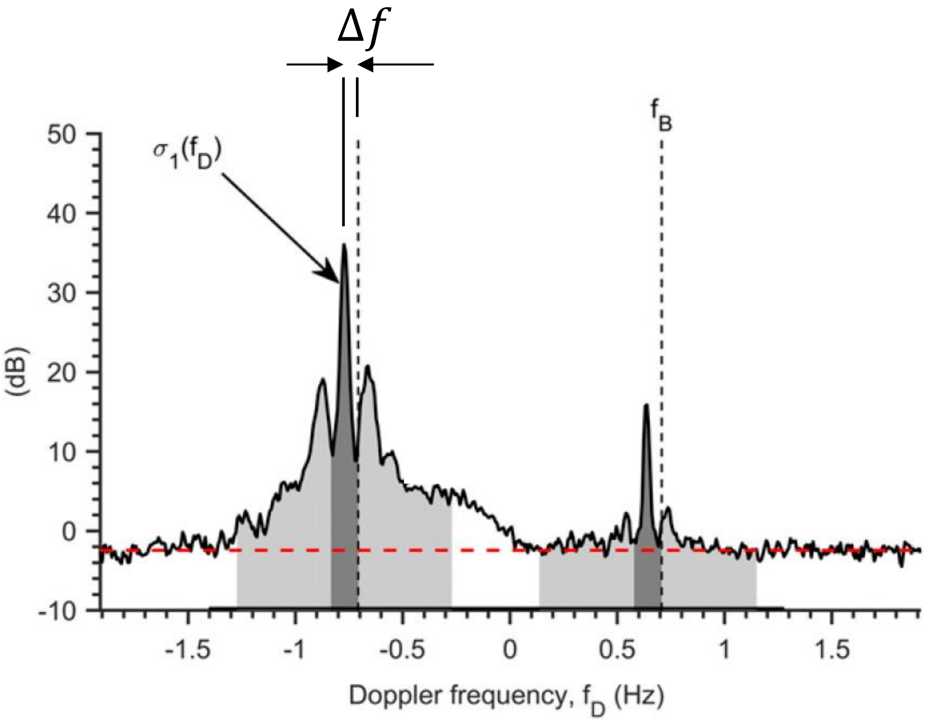

Figure 1.2: Power spectrum of the received HF radar signal.
Modified from Alattabi et al., (2019).

HF radars are deployed on land and can measure surface currents up to 200km offshore depending on operating frequency (e.g., Roarty et al., 2019), which range from 3-50 MHz (covering the HF and low end of the VHF radio spectrum). The low frequency (e.g., 5 MHz) long range radar systems typically have range resolutions of 3-6 km, while higher frequency systems (e.g., 50 MHz) have less range (~20 km) but can have much higher resolutions (e.g., 150 m, Voulgaris et al., 2011). HF radars typically measure ocean currents every 15 – 60 minutes (Roarty et al., 2019), but methods have been developed for much shorter measurement periods which can be implemented for tsunami detection (Lipa et al., 2006, Dzvonkovskaya et al., 2018). HF radar systems cover a significant portion of the continental US coastline with additional sites providing coverage in areas of Hawaii, Alaska and Puerto Rico, with over 100 operational HF radar sites in the US. Additionally, the global footprint is large, with over 100 sites in Europe and 50+ in Oceania and Asian that together with the US sites form the global high frequency radar network (Roarty et al., 2019).

The use of HF radars for measuring surface currents offers advantages over traditional methods. They offer large coverage areas that other in situ measurement methods cannot (e.g., current meters and drifters are point measurements); they offer fast measurements (hourly or shorter increments) that satellites do not, and they provide measurements 24/7 through most weather conditions and sea states (e.g., satellites prefer no clouds). Although hurricanes and other high impact storms can damage these land based HF radar systems, there are now suggested installation and maintenance practices that account for this (Mantovani et al., 2020). Mitigation methods such as backup generators and flood mitigation have been implemented for radar systems in the mid-Atlantic bight so that the radar systems can operate throughout hurricane conditions (Roarty 2017, personal communication) as to provide data critical for hurricane research.

The data provided by operational radar systems is used for a myriad of research uses (Paduan and Washburn, 2013) including model validation and model assimilation over large areas (e.g., Mujiasih et al., 2021). Search and rescue operations may benefit from using HF radar measurements (Harlan et al., 2011; Breivik et., 2013) as well as assistance to oil spill response as they can be used to predict the trajectory of the oil spill (Bellomo et al., 2015). The surface currents are also used to aid maritime shipping (Rubio et al., 2017) and the radars are capable of detecting and tracking large ships (e.g., Cai et al., 2021). Their multiple uses have made HF radars and the data they can provide invaluable for both operational and research oceanography.

Although the usefulness of HF radar data is undeniable and the accuracy of HF radar currents well studied (Chapman and Graber, 1997; Essen et al., 2000), the underlying principle that the HF radar exploits to estimate surface currents, the phase speed of the ocean waves, likely is effected by Stokes drift from other waves (Chavanne, 2018). The exact phase speed is neither solved theoretically without using approximations (e.g., Barrick and Weber, 1977) nor has been conclusively determined experimentally in the ocean (Dussol et al., 2022) and studies on Stokes drift influences in wave tanks are limited (e.g., van den Bremer et al., 2018). Additionally, the algorithm for calculating the surface current estimates for the most commonly used HF radar systems (compact cross loop systems) has seen little use on the second most commonly used systems (beamforming linear arrays). Lastly, although different large scale HF radar networks have publicly available data (HFRnet in the US hosts measurements from over 100 operational HF radar sites), there is a lack of openly available toolsets (such as eddy identification routines) to exploit these data sets for ocean research.

1.2 Scope of dissertation

This dissertation is divided into three separate chapters addressing different but interrelated issues affecting the operation and performance of HF radars. These relate to (i) analysis of the signal recorded by linear array HF radar systems. (ii) Better identifying the phase speed of an ocean wave accounting for wave-wave interactions (i.e., how does Stokes drift affect the ocean wave?) and (iii) developing and optimizing an eddy identification routine for use with HF radar surface current data sets.

The dissertation is organized in the same order that HF radar data in processed in, first an algorithm calculates the locations of the HF radar phase speed measurements, relating to (i), then these phase speed measurements are used to estimate the ocean currents, relating to (ii), followed by an application of the HF radar measurements, such as eddy identification described in (iii). This order is necessary as well, due to the difficulty in measuring the small effect Stokes drift might have on the phase speed of ocean waves, the HF radar algorithm used should be as optimized as possible to produce accurate measurements of the phase speed of the Bragg waves.

The research carried out in the three areas listed above use HF radar measurements from two systems located at the northern and southern limits of Long Bay, SC (see figure 1.3), one located near Georgetown, SC (marked as GTN) and the other at

Fort Caswell, NC (marked as CSW). The radar systems are identical, both operated at 8.3 MHz from their installation in 2012 until mid-2020 when they were switched to 5.25 MHz in order to comply with FCC regulations. Each radar site consists of a four element transmit array, which directs ~99% of the transmitted signal towards the ocean, and 12 monopole receiving antennas positioned in a line along the coastline. As described previously, each HF radar system measures the phase speed of ocean waves traveling directly towards or away from the radar site, which is then used to estimate the surface ocean current. The radar system determines where the measurements are located (the location where waves scattered back the radar signal) by calculating the distance the scattered signal came from and direction it came from.

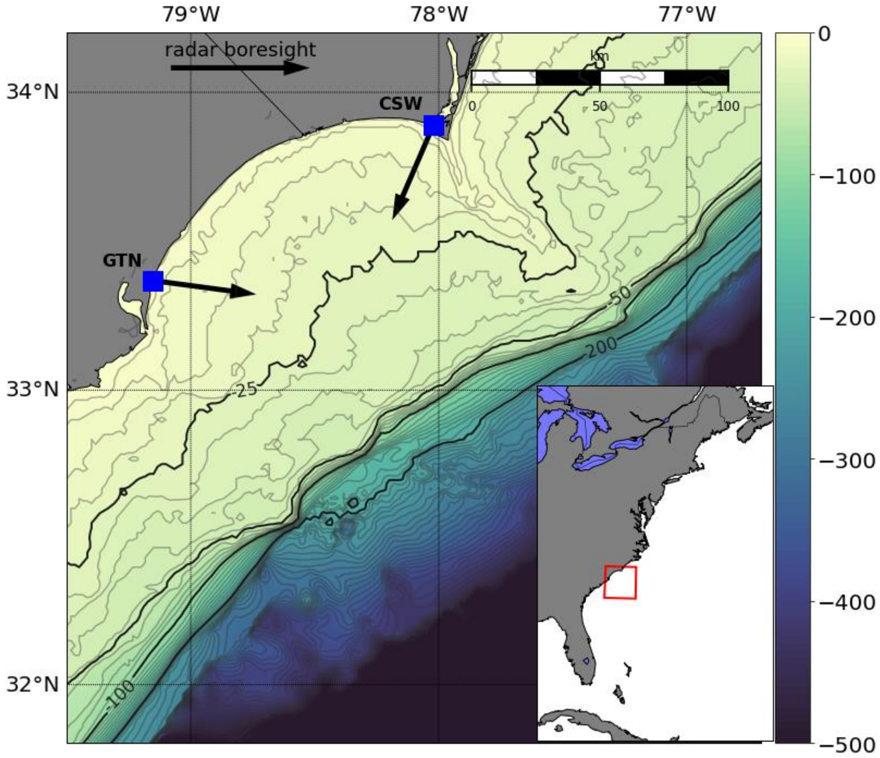

Figure 1.3: Study site overview with HF radar sites CSW and GTN, locations shown as blue squares. The direction the boresight of the radars are pointed in are shown as the black arrows.

The distant measurement is essentially a time-delay measurement which is then converted to distance by multiplying the time it took by the speed of light in air, $r = c\Delta t/2$; the factor of two is due to the round trip of the radar signal. While the distance measurement is straightforward, the accuracy of the calculated direction the scattered signal came from is dependent on both the antenna array geometry (in this case we have a linear array of monopole antennas) and what algorithm is used to calculate the direction.

In chapter 2, we use the measurements from these two HF radar sites and two current meters in the HF radar coverage area (one nearshore and one offshore) to compare different direction algorithms. The accuracy of the result is compared against in situ data.

In Chapter 3, after assessing the accuracy of the different HF radar algorithms, we use a 7-month data set HF radar measurements and in situ measurements at an offshore location to assess possible wave-wave contributions to the phase speed of the Bragg wave the HF radars measure. The different contributions of Stokes drift are estimated using the output of a wave propagation model. Neural network methods are explored as a method to identify the effect of Stokes drift on radar measurements without the need for a wave model.

Chapter 4 focuses on identifying eddies in HF radar surface current data. Eddies are important factors in fluxes across shelf breaks (e.g., Savidge et al., 2010), may play key roles in providing nutrients to the ocean surface layer in this area (Lee et al., 1991) and can be key breeding and feeding areas for fisheries (Govoni et al., 2013). The eddy identification routine is optimized for HF radar data sets, and momentum flux due to shelf break eddies is discussed in this chapter.

Finally, Chapter 5 presents concluding remarks about the research completed in Chapters 2-4, the successes and challenges that were overcome and that are yet to be resolved. Additionally, the potential for utilization of the findings of this work to other HF radar sites is presented along with some suggestions for future research.

CHAPTER 2

A COMPARISON OF BEAMFORMING AND DIRECTION FINDING ALGORITHMS (BEAMSCAN AND MUSIC) ON A LINEAR ARRAY HF RADAR IN A MEDIUM TO LOW WAVE ENERGY ENVIRONMENT[1]

---

[1] This Chapter has been published as Cahl D, Voulgaris G, Leonard L (2023) A Comparison of Beamforming and Direction Finding Algorithms (Beamscan and MUSIC) on a Linear Array HF Radar in a Medium to Low Wave Energy Environment. Journal of Atmospheric and Oceanic Technology, 40:191–218. © **American Meteorological Society. Used with permission.**

Abstract

We assess the performance of three different algorithms for estimating surface ocean currents from two linear array HF radar systems. The delay-and-sum beamforming algorithm, commonly used with beamforming systems, is compared with two direction finding algorithms, MUltiple Signal Classification (MUSIC) and direction finding using beamforming (Beamscan). A 7-month data set from two HF radar sites (CSW and GTN) on Long Bay, SC (USA) is used to compare the different methods. The comparison is carried out on three locations (mid-point along the baseline and two locations with in situ Eulerian current data available) representing different steering angles. Beamforming produces surface current data that show high correlation near the radar boresight ($R^2 \geq 0.79$). At partially sheltered locations far from the radar boresight directions ($59°$ and $48°$ for radar sites CSW and GTN, respectively) there is no correlation for CSW ($R^2 = 0$) and the correlation is reduced significantly for GTN ($R^2 = 0.29$). Beamscan performs similarly near the radar boresight ($R^2 = 0.8$ and 0.85 for CSW and GTN, respectively) but better than beamforming far from the radar boresight ($R^2 = 0.52$ and 0.32 for CSW and GTN, respectively). MUSIC's performance, after significant tuning, is similar near the boresight ($R^2 = 0.78$ and 0.84 for CSW and GTN) while worse than Beamscan but better than beamforming far from the boresight ($R^2 = 0.42$ and 0.27 for CSW and GTN, respectively). Comparisons at the mid-point (baseline comparison) show the largest performance difference between methods. Beamforming ($R^2 = 0.01$) is the worst performer, followed by MUSIC ($R^2 = 0.37$) while Beamscan ($R^2 = 0.76$) performs best.

2.1 Introduction

Modern, land-based high frequency (HF) radar systems are widely used to measure coastal surface ocean currents for both ocean research (e.g., Paduan and Shulman, 2004) and operations (e.g., Harlan et al., 2010; Roarty et al., 2019). Their accuracy in measuring ocean currents has increased over the last few decades, mostly due to improvements in signal analysis and calibration methods (e.g., Barrick and Lipa, 1999; Gurgel et al., 1999a; Kohut and Glenn, 2003; Guérin et al., 2021). HF radar derived surface current measurements are utilized for improving numerical circulation model predictions (Paduan and Shulman, 2004; Couvelard et al., 2021) through data assimilation. This has been shown to improve predictions relevant to oil spill response (Abascal et al., 2009) and search and rescue (Harlan et al., 2011; Bellomo et al., 2015) operations.

Surface current estimations are derived from the backscattered radar signal from ocean waves with a wavelength half that of the transmitted electromagnetic wavelength (Bragg scattering), first discovered by Crombie (1955). The difference between the HF radar measured speed of the Bragg wave and the theoretical one for still-water is used to estimate the surface ocean current, toward or away from the radar site (Barrick, 1977). The theoretical range resolution $\Delta r \approx \frac{c}{2B}$ of the HF radar system is determined by the bandwidth (B) of the radar (e.g., Gurgel et al., 1999b) and the speed of light, c. Angular resolution is based on both the radar system (i.e., number of antennas and antenna array characteristics) as well as the signal processing method used. Most modern HF radar systems are mainly beamforming linear arrays (BLA, e.g., Gurgel et al., 1999a) or direction finding (DF) compact cross loop (CCL) systems (Barrick and Lipa, 1997), called DF-CCL systems herein, although other configurations have been also used (e.g., Fernandez and Paduan, 1996; Kirincich et al., 2019).

In modern monostatic BLA systems, the radar signal is transmitted towards the ocean which is then backscattered from Bragg waves in the ocean that are traveling directly toward or away from the radar. The radar signal is backscattered from many locations in the ocean which is then received by the receiving antennas. The signals from all the receive antennas are first range gated, separating the signal into different range bins. After this, each range bin is processed separately. The signal from all receiving antennas from a single range bin is digitally beamformed by summing the signal of individual antennas after applying a delay (phase shift) and an amplitude weight to them (e.g., Van Trees, 2004). The phase shifts are chosen to maximize the array's sensitivity to incoming signal from a particular direction. The Bragg peaks in the resulting Doppler spectrum, for a particular direction and at a specific range, are then analyzed. The local maxima of the Bragg peaks are used to calculate their frequency (Doppler) shift from their still-water locations which is due to the presence of a surface ocean current (Gurgel et al., 1999a).

Direction finding (DF) uses the Doppler spectrum from each antenna to identify which Doppler frequencies (each corresponding to a different surface current velocity) correspond to Bragg scattering. Then, for each Doppler frequency identified, the bearing angle(s) of the signal(s) is calculated using a direction-finding algorithm. The most common and successful direction-finding algorithm used with HF radars is the **Mu**ltiple **Si**gnal Identification and **C**lassification (MUSIC) first introduced by Schmidt (1986) and applied to HF radars by Barrick and Lipa (1997). Both BLA and DF-CCL radar systems provide reliable surface ocean currents (Essen et al., 2000) and offer similar levels of accuracy (Chapman et al., 1997; Kuang et al., 2012; Liu et al., 2014; Paduan and Washburn, 2013). Although BLA systems require antenna arrays that are significantly larger than CCL systems, with 12-16 receive antennas they only offer $120°$ of coverage, $\pm 60°$ from the boresight (perpendicular to the linear array) of the radar receiving array (Gurgel et al., 1999a) as opposed to $360°$ coverage for CCL systems (Barrick and Lipa, 1997; Yeping, et al., 2017). With an 8 antenna linear array, the coverage is reduced to $90°$ or $\pm 45°$ from the boresight.

Beamforming suppresses signals from other directions significantly better near the boresight than far from it. If the oceanic wave field is directed mainly along the boresight of the radar, the resulting radar signal is strongest along this direction and weaker at higher angles, with a minimum at 90 degrees to the boresight. Under such conditions, when beamforming ('looking') far from the boresight the signal at $0°$ may not be sufficiently suppressed (Laws et al., 2000) leading to inaccuracies in current estimations. However, it has been argued theoretically, that when antenna patterns are ideal, beamforming is effective even under these conditions (Heron, 2017), while others have suggested that using MUSIC on a linear array could outperform beamforming in this situation (Laws and Fernandez, 2000). The experimental study of Wang and Gill (2016) suggested that combining beamforming and MUSIC may offer the best surface ocean current estimates with a BLA radar system.

The objective of this study is to explore the possible benefits of using direction finding algorithms on a BLA radar system. The linear receiving array in BLA systems is commonly spaced by 0.45 to 0.5 radar wavelengths, where 0.5 is the optimal spacing for linear arrays using Beamforming as well as MUSIC (Gupta and Kar, 2015). In addition to MUSIC, one can simply use beamforming as the direction finding algorithm, where instead of analyzing the Doppler spectrum at each direction, the beam is scanned over azimuth for each frequency (e.g., Krim and Viberg, 1996) corresponding to Bragg scattering. The direction where the power of this frequency is maximized is considered the direction of arrival (DOA) of that frequency. This direction finding method of beamforming has more recently been referred to as Beamscan in MATLAB®'s Phased Array System Toolbox (Mathworks, 2022). In this manuscript the term "beamforming" refers to the method of analyzing the Doppler spectrum at each direction of interest, which is the default methodology for beamforming commercial HF radar systems such as WERA (Gurgel et al., 1999a). The term "Beamscan" refers to the method whereby beamforming is used as a direction finding method to create a spatial spectrum over direction for each frequency.

Although Beamscan has been compared with other direction finding methods in signal analysis research (e.g., Sun et al., 2018), to the authors' knowledge, it has not been used for HF radar surface current measurements. Degradation of beamforming performance at high steering angles (>50°) motivates the assessment of the algorithms (i.e., beamforming, Beamscan, and MUSIC) examined in this study at such high angles. It is worth noting that application of these methods depends on antenna geometry. While MUSIC can be applied to any antenna geometry, beamforming and Beamscan require a larger array, although theoretically you could apply beamforming to any antenna geometry as well. Such arrays commonly consist of 8-16 antennas spaced roughly half a wavelength apart on a linear configuration although other array geometries such as curved and circular arrays have also been used for beamforming. However, receiving arrays consisting of collocated antenna elements or very small grid arrays (less than wavelength in size) are not capable of beamforming well enough for use in HF radar surface current measurements.

In the remainder of the paper, we first present a brief description of the three methods (Section 2.2). This is followed by a presentation (Section 2.3) of the HF radar system and the in situ data sets used in this study. In Section 2.4 the radial current estimates from each method are compared against the in situ data and against each HF radar system at a location along their baseline. Finally, the performance of the three methods is discussed in Section 2.5 and the conclusions are presented in Section 2.6.

2.2 HF radar surface current estimation methodology

2.2.1 Initial signal processing and range sorting

Gurgel et al. (1999b) and Gurgel and Schlick (2009) have provided detail description of the signal processing applied in beamforming linear array (BLA) radar systems, therefore only a brief description is presented in here.

An HF radar emits an upward (or downward) frequency modulated ‘chirp’ signal which is backscattered by the ocean waves and received by the system antennas. The individual antenna received signals are demodulated and recorded as a complex time series representing the in-phase (I) and quadrature-phase (Q) components. Then, an initial Fast Fourier Transform (FFT) is performed on the complex signal for each chirp, i, to estimate its energy distribution in the frequency domain:

$$G_i(f) = FFT[I_i(t) + iQ_i(t)] \tag{2.1}$$

where t is the time within the chirp i (i.e., $t_i < t < t_i + T$ where T is the chirp duration and t_i is the starting time of chirp i). Because the transmit signal is 'chirping' over a frequency range defined by the chirp bandwidth (B), the frequency bands from this FFT analysis correspond to different time delays,$\left(\Delta t = \frac{T}{B} f\right)$ which represent corresponding range bins ($r = \frac{c\Delta t}{2} = \frac{cTf}{2B}$, where c is the speed of light in vacuum). Using the above relationships, the signal for each chirp $[G_i(f)]$ is sorted into the different ranges it originated from $[G_i(r)]$.

Theoretically, the range resolution ($\Delta r = c/2B$) is defined by the bandwidth of the chirp but the actual (effective) resolution is lower as it is affected by the window applied to the signal prior to applying the FFT (Voulgaris et al., 2011). Each chirp creates a data point for each range bin (r); corresponding data points from the same range bin from all consecutive chirps are used to create a time-series $R_k(i = 1, M)$ where M is the number of chirps and k denotes a particular range bin (r_k). As an example, for range r_k a time-series is created

$$R_k(i) = [\, G_1(r_k), \dots, G_{i-1}(r_k), G_i(r_k), G_{i+1}(r_k), \dots, G_M(r_k)] \tag{2.2}$$

where i $(= 1, M)$ is the chirp number. The time interval between data points is the chirp duration (T).

Subsequently, each range sorted time series (i.e., a series per range bin k) is subjected to a 2nd FFT:

$$P_k(f_D) = FFT[R_k(i)] \tag{2.3}$$

which produces an amplitude $|P_k|$ and phase $\tan^{-1}\left[\frac{\mathrm{Re}(P_k)}{\mathrm{Im}(P_k)}\right]$ for each Doppler frequency (f_D). The amplitudes squared ($|P_k|^2$) constitute the familiar Doppler power spectrum for a single range bin, shown as the blue line in Fig. 1.

In the following sections, the description of the methods for surface current analysis pertains to the Doppler spectrum (amplitude and phase) from a single range bin; the same methodology is applied to each one of the range bins separately.

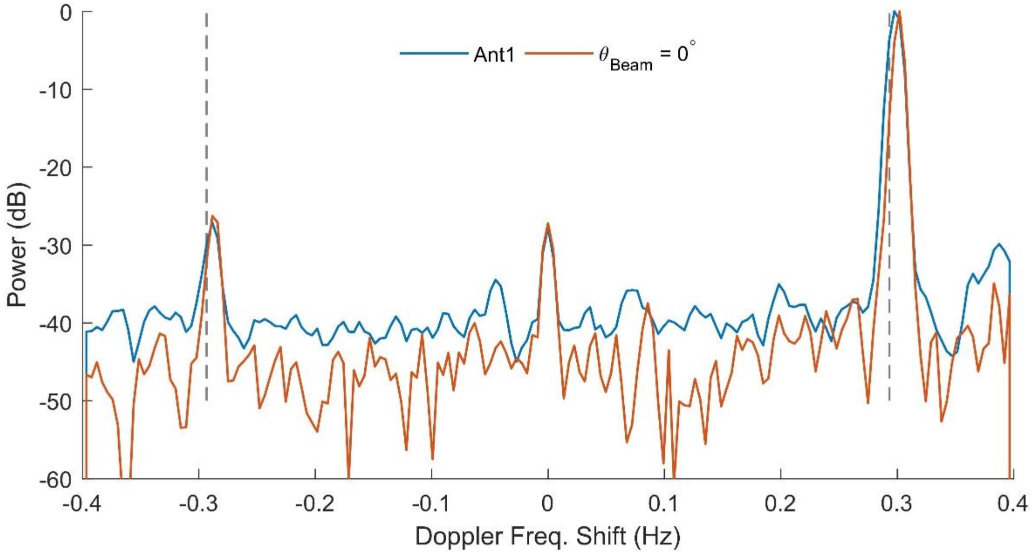

Figure 2.1: Example of Doppler spectra from an 8.3MHz radar for a single range cell ($r = 30$ km) from a single antenna (blue line) and from all 12 antennas beamformed along the boresight (red line). The location of the Bragg peaks in still-water (theoretical) are shown as vertical dashed gray lines. The radar acquisition is 2048 chirps each with a chirp length of 0.4333 seconds. The FFT analysis consists of 512 length segments with 50% overlap, resulting in 7 overlapping segments. The resulting Doppler power spectra shown in the plot are normalized by their maximum values.

2.2.2 Beamforming

Each antenna receives backscattered signals from many directions at once, therefore the energy of the single antenna Doppler spectrum (blue line in Fig. 1) contains information originating from multiple directions. Beamforming combines the amplitudes and phases from all receive antennas and effectively ‘points’ the receiving array’s sensitivity to a particular direction of interest by suppressing backscattered signals from other directions (red line in Fig. 1). For a linear array, beamforming perpendicular to the array (along the radar boresight, θ_b) to a surface patch of the ocean at range r_k, very far away ($L_N \ll r_k$, where L_N is the length of the linear array) is performed by adding the individual antenna Fourier coefficients [obtained from (3)] together,

$$B(f_D, r_k, \theta_b) \approx \sum_{j=1}^{N} P_k^j(f) \qquad (2.4)$$

where j (=1 to N) is the antenna number of the N element receiving array.

To “steer" the beam to a particular direction, a phase shift is first subtracted from the signal from each antenna to compensate for the difference in time of arrival. A backscattered signal from range bin k (measured from the center of the receiving array) at an angle θ measured counterclockwise from East (polar coordinates) will result in a phase $\phi_k^j(\theta)$ in the received signal at each antenna j. Assuming a planar approximation of the earth this phase can be estimated as:

$$\phi_k^j(\theta) = 2\pi\lambda_R^{-1}\left[\left(r_k\cos\theta - x_j\right)^2 + \left(r_k\sin\theta - y_j\right)^2\right]^{\frac{1}{2}} \qquad (2.5)$$

where x_j (Easting) and y_j (Northing) are the antenna positions measured from the center of the receiving array and λ_R is the wavelength of the radio wave transmitted by the HF radar. Beamforming to this location is performed by subtracting the theoretical phase shift $\phi_k^j(\theta)$ from each complex Fourier coefficient P_k^j, for each antenna j. Then these values from all N receiving antennas are summed so that:

$$B(f_D, r_k, \theta) = \sum_{j=1}^{N} w_j P_k^j(f_D) e^{-i\phi_k^j(\theta)} \qquad (2.6)$$

An example of the power, $|B|^2$, of the beamformed signal for a single range cell (r_{20}) and beam direction (0°), which is along the boresight ($\theta - \theta_b = 0°$), is shown in Fig. 1 (red line). Usually, a Hamming or an Ultraspherical window (w_j) is applied before beamforming (see Gurgel et al., 1999b; Helzel and Kniephoff, 2010) to increase suppression of unwanted signals coming from directions other than the beam direction (sidelobe effects), usually at the cost of a wider beam. General practice is to use Hamming for 8-12 antenna and Ultraspherical for 12-16 antenna BLA systems (see Helzel and Kniephoff, 2010).

The derived Doppler spectrum is then used to identify the Bragg peaks and measure their frequency shift (Δf) from the theoretical (still-water) value which is then used to estimate the radial current ($u = \Delta f \lambda_B$, where λ_B is the Bragg wavelength) along that direction (Gurgel et al., 1999a). This process is repeated for all Doppler spectra from all ranges and directions of interest. It should be noted that for beamformed Doppler spectra the Bragg peaks are relatively narrow, and any broadening is attributed mainly to diversity in current velocities within the patch of the ocean the Doppler spectrum corresponds to (i.e., current shear etc., Zhang et al., 2012).

2.2.3 Direction Finding

While beamforming “steers" the radar toward a particular location and then analyzes the beamformed signal to estimate the corresponding Doppler spectrum from that location [$B(f_D, r_k, \theta)$, see (6)], direction finding (DF) performs the inverse operation; it starts with the signals in each antenna and calculates the most likely direction(s) the signals originated from (e.g., Read, 1989). The received signals are due to Bragg scattering from Bragg waves and the direction(s) these signals were scattered from are defined as the directions of arrival (DOAs). DF uses the complex Doppler spectra $P_k^j(f_D)$ from all antennas (Barrick and Lipa, 1997) to calculate single or multiple DOAs for each frequency bin f (Barrick and Lipa, 1999):

$$\theta_{DOA}(r_k, f_D) = DF\left[P_k^{j=1,N}(f_D)\right] \tag{2.7}$$

where $P_k^j(f_D)$ are the Fourier coefficients corresponding to antenna j for a given range (r_k) and Doppler frequency bin (f_D).

For each range bin and each antenna, the Doppler spectrum [$P_k^j(f_D)$, see (3)], has distinctive Bragg peaks (see the two large peaks near the still-water Bragg peaks from individual antenna, blue line in Fig. 1). In contrast to beamforming (red line in Fig. 1) the Bragg peaks from individual antennas are broader and span multiple frequencies; each frequency within the broad peaks corresponds to a different offset from the still-water Bragg peak location. These different frequency offsets represent different values of ocean currents corresponding to different patches of the ocean of the same range but with different azimuthal angles. Although DF algorithms can be used on all the frequencies in the Doppler spectra $P_k^j(f_D)$, in surface ocean current estimation only the frequencies that lie within a range of the theoretical Bragg peak are considered. This frequency range (Bragg region) is often defined by the SNR level (e.g., Lipa et al., 2006) and its correspondence to within certain current velocity limits (e.g., ± 1 m/s from the still-water Bragg peak location). Other more advanced Bragg region selection techniques have been developed (e.g., Kirincich et al., 2019) that are not reviewed here as this is beyond the scope of the paper.

In comparing beamforming and direction finding, certain differences should be noted. In practice beamformed Doppler spectra are limited by beamwidth and steering angle resolution, which are functions of the antenna array geometry (i.e., a longer array with more antennas can provide a narrower beam and higher steering resolution). However, this is not the case for DF methods, as they are able to obtain a number of solutions which is proportional to the number of frequency bins that lie within the Bragg region and also the number of RX antennas (Sentchev et al., 2013). Usually, this results in numerous gaps in the radar coverage area (Liu et al., 2014) which in practice can be filled in using interpolation techniques.

Although several DF algorithms have been developed (see Tuncer and Friedlander, 2009) MUSIC is the most popular, primarily because of its computational efficiency. MUSIC is routinely used to analyze the signal from the commercially available Compact Cross Loop (CCL) radar systems (i.e., CODARs Ocean Sensors) that use a single monopole antenna and two orthogonal loop antennas (Barrick et al., 1994). More recently, the Maximum Likelihood method has shown some promise in improving surface currents estimates with CCL systems (Emery et al., 2018), however to our knowledge this method is not used operationally yet. Beamscan is a DF algorithm based on beamforming and therefore is applicable to beamforming systems. Due to the ease of implementation only Beamscan and MUSIC (the most common and popular DF method in HF radars) are considered in this study and briefly described below.

2.2.3.1 Beamscan DF method

The Beamscan algorithm can only be utilized by beamforming systems (Tuncer and Friedlander, 2009) and it is not a subspace method. Although, it can use an array covariance matrix created from several samples (e.g., Krim and Viberg, 1996), in this application we use [6] which requires the estimation of a single complex Fourier coefficient P_{k,f_D}^{j} for each antenna. The latter corresponds to a single frequency of the complex Doppler spectra [$P_k^j(f_D)$, see (3)]. The DOAs of this frequency (f_D) are determined by beamforming P_{k,f_D}^{j} [using (6)]. This creates a Beamscan spatial spectrum $B_{r_k,f_D}(\theta)$ for the particular Doppler frequency (i.e., f_D is fixed) as a function of θ (see Fig. 2). The DOA(s) corresponding to f_D are determined by the peak(s) found in the Beamscan spatial spectrum. Although Beamscan can detect DOAs from multiple directions, noise and sidelobe interference can overwhelm weaker signals resulting in false or inaccurate DOA solutions. This is shown in Fig. 2 where synthetic spectra corresponding to one (Fig. 2a) and four (Fig. 2b) DOAs are shown. Additionally, accurate identification of the DOAs requires they are separated by more than the beamwidth of the radar array. This is shown in Fig. 2b where the signals from $0°$ and $10°$ are spaced apart by an angle that is smaller than the system's beamwidth ($15°$); this results in incorrect Beamscan DOA estimates of $-5°$ and $13°$. To reduce the number of

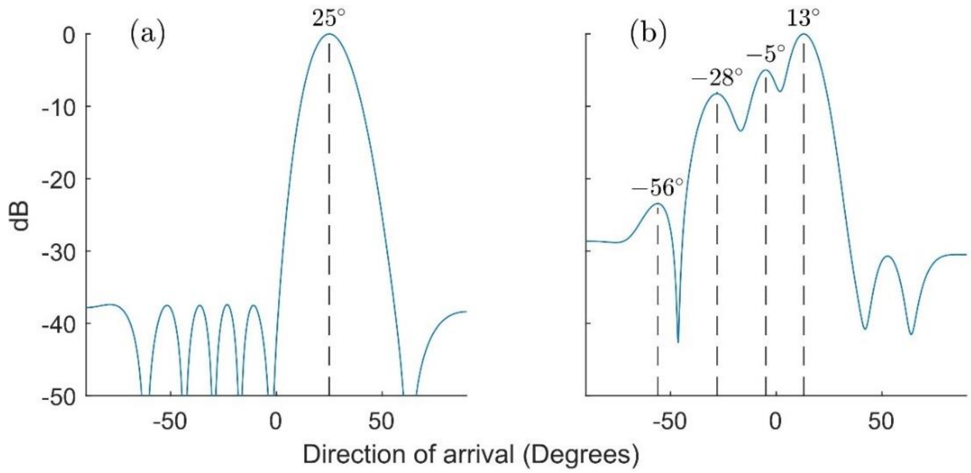

Figure 2.2: Examples of idealized (no noise) synthetic Beamscan spectra: (a) single DOA with the signal arriving from 25 degrees off the boresight and with 0 dB amplitude. (b) four DOAs arriving from -45, -30, 0 and 10 degrees with amplitudes of -20, -10, -3 and 0 dB, respectively. The numbers on the plots correspond to the DOA angles as identified by the peaks in the Beamscan spectrum.

inaccurate solutions, in this study only the DOA solution corresponding to the largest peak is used with the Beamscan method.

Beamforming and Beamscan derived Doppler spectra are shown in Fig. 3 where a simplistic model of the Doppler spectrum over azimuth [see (6) where θ is on the x-axis and f_D is on the y-axis) for a single Bragg peak, that has been Doppler shifted by a current parallel to shore (and where the frequency of the Bragg wave has been shifted to 0 Hz) is shown.

Analyzing each direction separately (giving plots of power vs. frequency) is the beamforming method commercial HF radars use (see Fig. 3b which corresponds to the frequency slice of the white arrow marked Beamforming in Fig. 3a). The current is determined from the frequency shift of the SNR weighted location of the Bragg peak, marked as a black circle in Fig. 3b. The direction finding version of beamforming (Beamscan), analyzes each frequency separately (giving plots of power vs. direction of arrival) as shown in Fig. 3c (which corresponds to the direction of boresight slice of the white arrow marked Beamscan in Fig. 3a) where a single Beamscan spatial spectrum at -0.05 Hz is presented. The current is determined by -0.05 Hz and the location of this current is defined by the location of the peak of the Beamscan spatial spectrum in Fig. 3c., marked as the red square.

The estimated currents from beamforming and Beamscan are plotted in Fig. 3a (as black circles and red squares, respectively), where the direction of the current is on the x-axis and the frequency shift of the current is on the y-axis. These current estimates show that these two methods produce different results.

2.2.3.2 MUSIC DF method

The application of MUSIC involves processing each frequency separately, similarly to the application of Beamscan as explained earlier. However, MUSIC, being a subspace method, requires multiple samples of the signal in each frequency bin (Schmidt, 1986), while Beamscan can be implemented using a single sample in each frequency bin, although multiple samples can also be used (e.g., Krim and Viberg, 1996). Therefore, for each antenna multiple complex Fourier coefficients P_{k,f_D}^{j} are required; these are created by splitting a single long radar acquisition into multiple subsamples so that multiple complex Doppler spectra [$P_k^j(f_D)$, see (3)] are created for each antenna (see Barrick, 1997). This requires longer transmission times and in practice results in radial velocity estimates at intervals of 30 minutes or longer, depending on environmental conditions and noise (Barrick, 2008). Detailed description of the use of MUSIC for HF radar compact antenna systems is given in Barrick and Lipa (1997).

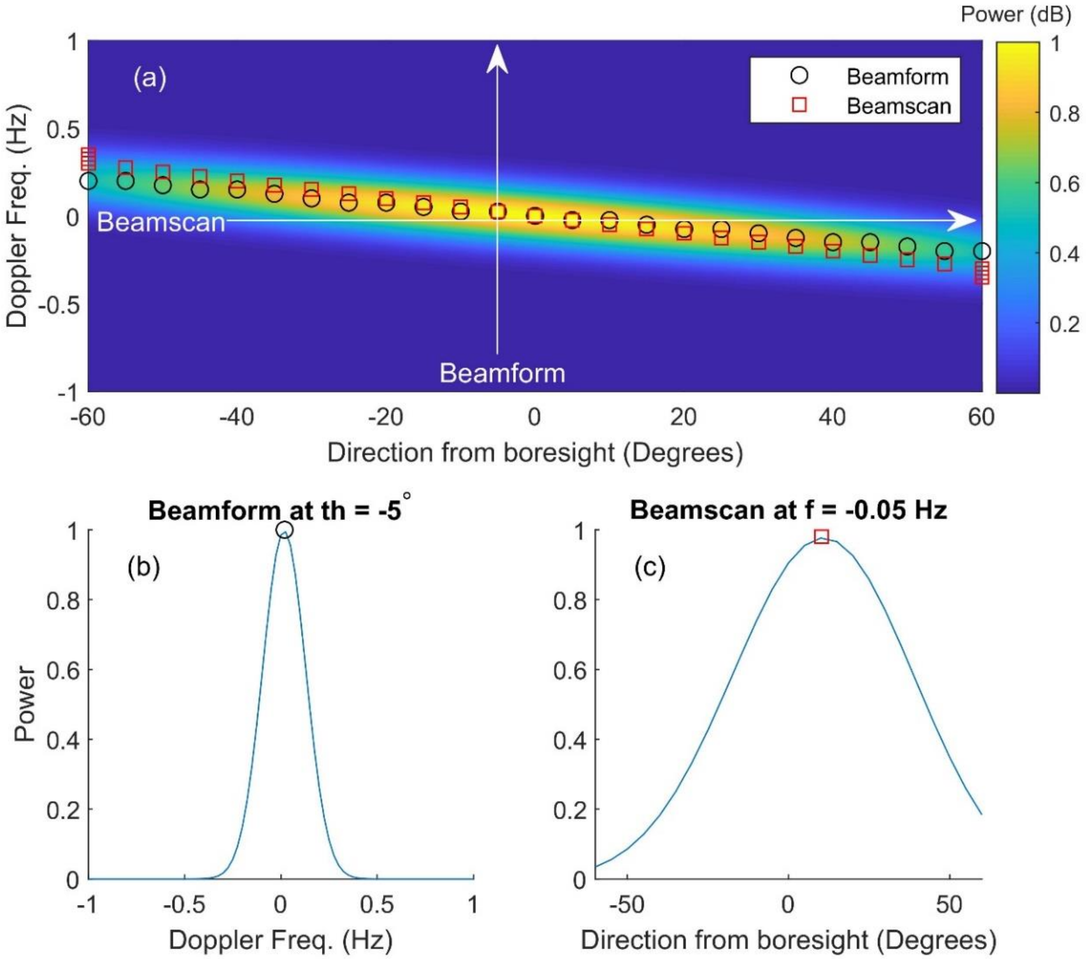

Figure 2.3: (a) Beamformed Doppler-Spatial spectrum; Doppler frequency spectra as function of direction from boresight created by modelling a current parallel to shore for the incoming Bragg peak (see section 4f), where its still-water location has been shifted to 0 Hz. White arrows correspond to the frequency (-0.05 Hz) and direction from boresight ($-5°$) slices for beamforming and Beamscan which are shown in (b) and (c), respectively.

Following Barrick and Lipa (1997), each radar acquisition or subsample (called a 'sample' from now on) provides a Doppler spectrum $P_k^j(f_D)$ estimate for each antenna j. For a single frequency and each antenna j, a vector of the complex Fourier coefficients

P_{k,f_D}^{j} is created, $\mathbf{X} = \left[P_{k,f_D}^{j}\right]$. Subsequently, an N by N signal matrix $\mathbf{S}$ is formed by multiplying this vector by its conjugate transpose, $\mathbf{S} = \mathbf{X}\mathbf{X}^{H}$. Several signal matrices $\mathbf{S}$ are created from a number (M) of consecutive radar acquisitions with each acquisition providing a P_{k,f_D}^{j} value. The receive matrices $\mathbf{S}$ are averaged to produce a covariance matrix, $\mathbf{C}$, so that

$$\mathbf{C} = \frac{1}{M}\sum_{i=1}^{M}\mathbf{X}(i)\mathbf{X}^{H}(i). \tag{2.8}$$

The maximum number of DOAs (D) that can be calculated using the MUSIC algorithm is constrained by the number of acquisitions used for averaging (M) and the number of antennas (N), so that D must satisfy both conditions $D \leq M$ and $D \leq N - 1$. The eigenvalues and eigenvectors of the covariance matrix $\mathbf{C}$ represent the signal(s) and noise for the particular frequency (see Fig. 4a). The largest eigenvalues and corresponding eigenvectors represent the DOAs while the remaining eigenvalues represent noise. A noise matrix is created, where the $N - D$ noise eigenvectors form the columns of the noise matrix $\mathbf{E_n} = [\mathbf{E_n}]$, an N by $N - D$ matrix. The MUSIC pseudospectrum, $P_{MU}(\theta)$, is defined as

$$P_{MU}(\theta) = \frac{1}{\mathbf{A}^{H}(\theta)\mathbf{E_n}\mathbf{E_n}^{H}\mathbf{A}(\theta)}, \tag{2.9}$$

where $\mathbf{A}(\boldsymbol{\theta}) = \left[a_j(\theta)\right]$ is a column vector of the complex antenna patterns $a_j(\theta)$. The D largest maxima in $P_{MU}(\theta)$ correspond to the D direction of arrival(s) of the signal(s) within this frequency bin. More details can be found in Barrick et al. (1999) who provided a thorough description of the application of MUSIC to CCL HF radar systems. The process in choosing how many sources $(D = 1$ to $N - 1)$ are present in a particular frequency bin is key to acquiring accurate DOAs and several different methods have been employed (e.g., Barrick and Lipa, 1997; Laws and Fernandez, 2000). The approach used here is called MUSIC-highest and it has been described in detail in Kirincich et al. (2019). The method assesses the DOA function $P_{MU}(\theta)$ for each different number of signals (1 to $N-1$) and then the highest number of DOAs (D) where the MUSIC pseudospectrum $P_{MU}(\theta)$ has the same number of peaks as the number of DOAs (D) is chosen.

An example of this analysis is presented in Fig. 4 using synthetic data. Two uncorrelated signals were created with DOAs of $15°$ and $25°$ and corresponding signal amplitudes of -10 dB and 0 dB, respectively. Then a -10 dB of Gaussian noise was added to them. Using this synthetic signal, a covariance matrix was created with 20 samples assuming a 12 antenna linear array with 0.45λ antenna spacing. The sorted eigenvalues from the eigen decomposition of the covariance matrix are shown in Fig. 4a. The corresponding MUSIC DOA pseudospectrum $P_{MU}(\theta)$ for $D=2$ (2 DOAs) is shown in Fig. 4b. Pseudospectra for $D=1-11$ DOAs are shown in Fig. 4c. It is worth noting that some of the pseudospectra in Fig. 4c show an incorrect number of DOAs i.e., $D\neq 2$ with additional peaks at locations other than the prescribed $15°$ and $25°$. For example, the top magenta line in Fig. 4c shows the MUSIC pseudospectrum for $D=11$ and contains 5 prominent peaks, although there are only two actual DOAs. Only the $D=2$ pseudo spectrum contains the same number of peaks as D, and therefore $D=2$ corresponds to MUSIC-highest, which gives the correct solution.

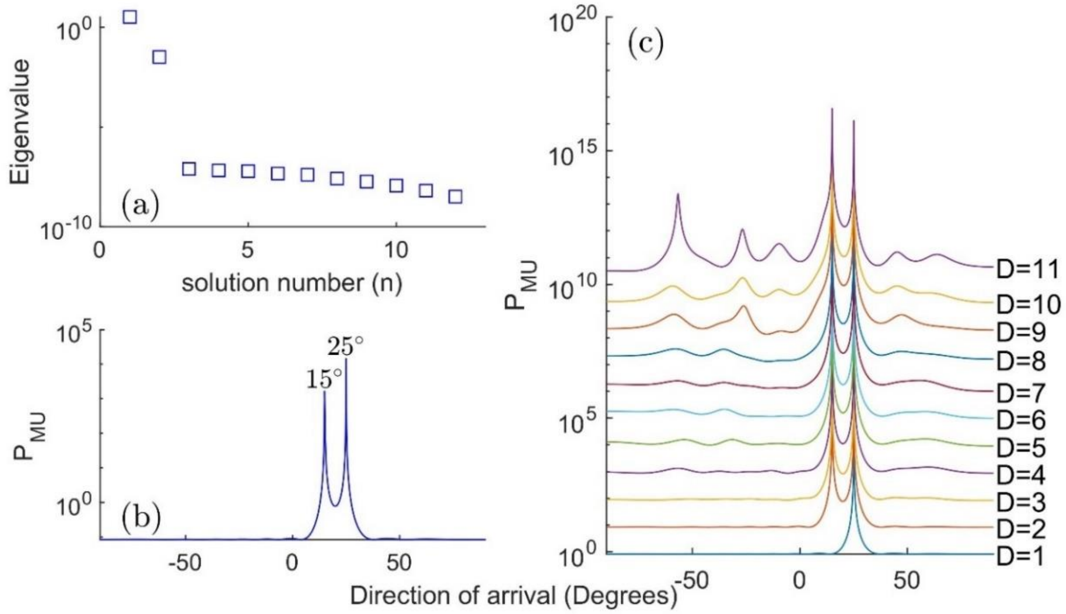

Figure 2.4: Example of MUSIC analysis using a synthetic covariance matrix created with 20 samples assuming a 12-antenna linear array with 0.45λ antenna spacing. The input consists of two uncorrelated signals with DOAs at $15°$ and $25°$, signal amplitudes of -10 and 0 dB, respectively, and -10 dB Gaussian noise. (a) Eigenvalue decomposition of the covariance matrix; (b) corresponding MUSIC pseudospectrum for the 2 DOA solution; (c) the 11 MUSIC pseudospectra (artificially vertically offset for clarity) corresponding to the 1-11 DOA solutions.

2.3 Data availability and processing

For this study, two HF radars are used to estimate surface ocean currents at three sites in Long Bay, off the South Carolina (USA) coastline (see Fig. 5). Long Bay extends some 100 km along the coast and shelf circulation is predominantly influenced by local winds and the passage of low-pressure synoptic fronts (Wu et al., 2017). Despite the local extent of the synoptic fronts, their predominant directions (from NE or SW) result in highly energetic wave events with high oblique angles of approach near the coastline

(Voulgaris et al., 2008). On average, wind speed is stronger offshore and reduced inshore (Wu et al., 2018), therefore, offshore wave heights are expected to be larger than inshore wave heights. In situ measurements (Gutierrez, 2006) have shown that tidal oscillations account for 30 to 45% percent of the total current variability. In the inner-self M2 alongshore-current amplitudes increase with proximity to the coastline where they dominate over cross-shore tidal flows. Further offshore, the cross-shore current tidal amplitudes decrease seaward in agreement with Poincaré wave theory.

2.3.1 Comparison sites and in situ data

The location of the sites with in situ current data available are shown in Fig. 5. They are denoted as ADCP1 and SSBN7 and are located at (78.347° W, 33.379° N) and (78.482° W, 33.841° N) corresponding to water depths of 25 and 10 m, respectively. Data from site ADCP1 were collected using a bottom mounted 600 kHz ADCP configured to collect data with a vertical resolution of 1 m; the topmost usable bin was located 3.1 m below the surface. Currents were recorded every 20 min and each record was the average of a 14 min ensemble. Data for site SSBN7 were obtained from NOAA/NDBC (https://www.ndbc.noaa.gov/station_page.php?station=ssbn7) that stores current data collected by a bottom mounted 600 kHz ADCP deployed at 10m water depth and operated by the Coastal Ocean Research and Monitoring Program (CORMP, Bushnell et al, 2018).The system was configured to collect data representing ensemble averages of 10 minutes, with a bin size of 1 m and the uppermost bin is centered 1 m below the surface.

ADCP1 is located close to the radar boresights (see Fig. 5), corresponding to

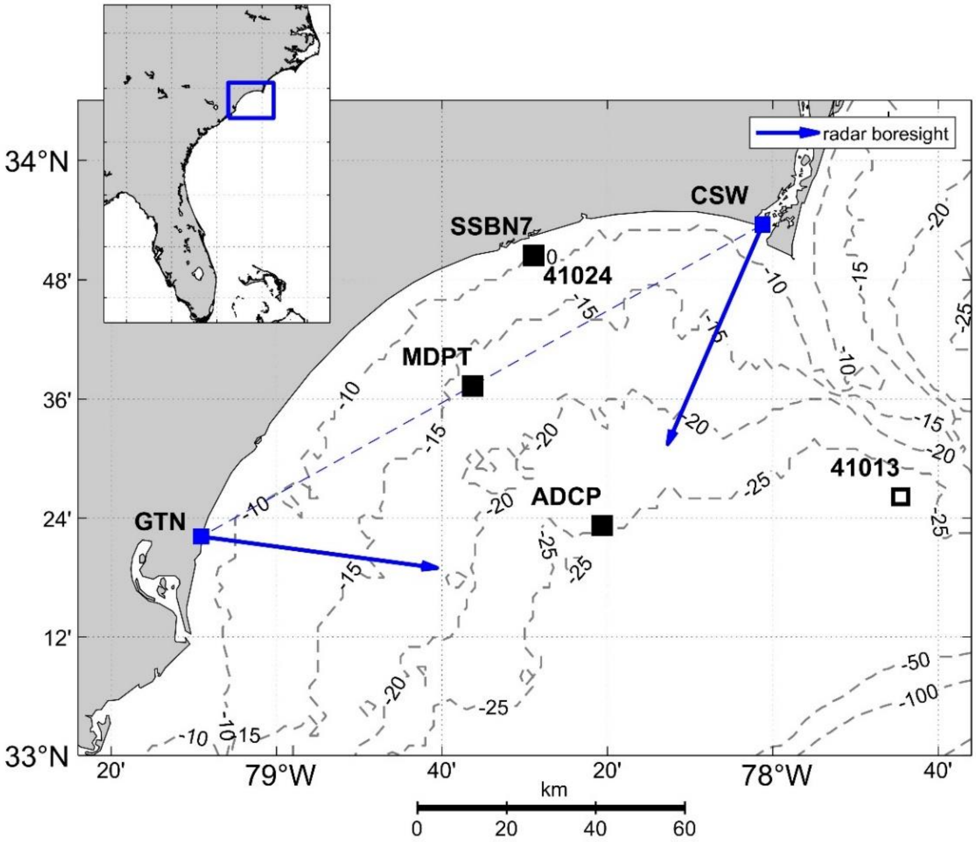

Figure 2.5: Study site location showing HF radar sites (GTN and CSW, blue squares) and their boresight (or radar look) directions (blue arrows; for angle values see Table 2). In situ current meter deployment locations (ADCP1 and SSBN7) and the baseline midpoint (MDPT) between the two radar sites are shown (black squares). Wind data were obtained from NDBC buoys 41013 and 41024 (open squares). Bathymetry contours shown in meters.

radar beam directions of 4.9° and 9.4° and ranges of 63.5 and 75.2 km for radar sites CSW and GTN, respectively. On the other hand, SSBN7 is near the limits of beamforming (±60°) corresponding to beam directions of −59.1° and 47.9° from the radar boresight and ranges of 43.1 and 81.3 km for CSW and GTN, respectively. The third site selected is the midpoint (MDPT) location (78.6047° W, 33.622° N) along the baseline between the two radars (see Fig. 5); it corresponds to beam angles of −37.1°

and 38.1° for CSW and GTN, respectively and a range of 60 km (see Table 1). At this location it is expected that the two systems would provide the same radial velocity but with opposite sign.

Table 2.1: HF radar beam characteristics at the comparison sites and % of successful radial current estimates (S) for each of the methods used. Radial directions are in mathematical convention, counterclockwise from East, whilst beam directions are with reference to the radar boresight (−113.4° and −7.6° for CSW and GTN, respectively).

HF Radar	Site	Radial Dir (°)	Beam Dir (°)	Range (km)	Successful Estimates (S)		
					beamform	Beamscan	MUSIC
CSW	ADCP1	−118.3°	−4.9°	63.5	91%	99%	97%
	SSBN7	−172.5°	−59.1°	43.1	89%	54%	34%
	MDPT	−150.5°	−37.1°	60.0	84%	90%	74%
GTN	ADCP1	1.8°	9.4°	75.2	78%	94%	93%
	SSBN7	40.3°	47.9°	81.3	59%	45%	42%
	MDPT	30.5°	38.1°	60.0	86%	81%	88%

2.3.2 HF Radar data

The two HF radar systems used are located at Fort Caswell, NC (CSW), and Georgetown, SC (GTN), as shown in Fig. 5. The systems are part of the NOAA Integrated Ocean Observing Systems (IOOS). Both systems are operated by the University of South Carolina, Columbia since February 2012, and consist of a 12 antenna linear receiving array spaced 0.45 λ apart (where λ is transmit wavelength, $\approx$ 36 m). The HF systems are WEllen RAdars (WERA) manufactured by Helzel Messtechnik Gmbh (see Gurgel et al., 1999a). The transmit array consists of four monopole antennas arranged in a rectangular configuration (0.5λ by 0.15λ spacing) with the rear antennas having a phase delay of 0.35λ so that radiation toward land is suppressed. Both receive and transmit arrays are constructed using resonant monopole antennas with three elevated radials; their boresights are $-113.4°$ and $-7.6°$ (mathematical convection, counterclockwise from East) for CSW and GTN, respectively (see Fig. 5 and Table 1). The systems operate in “listen before talk" mode, and the transmit frequency is set between 8.2 and 8.4 MHz depending on ambient noise and/or radio interference detected prior to transmitting. They transmit a frequency modulated continuous waveform (FMCW) with a 50 kHz bandwidth that results in 3km range resolution. The Bragg waves that reflect the transmitted signal have wavelengths between 17.9 and 18.3 m depending on the exact frequency of transmission. For a nominal frequency of 8.3 MHz the Bragg peaks appears at ±0.294 Hz, assuming no mean flow and deep water conditions. Each radar acquisition consists of 2048 chirps of 0.43333s length each, resulting in an acquisition time of approximately 14.8 minutes. Acquisition is repeated every 30 min in order to reduce power consumption and allow the A/C to keep the electronics trailer cool in the subtropical climate. The details of the HF radar systems used are listed in Table 2.

In the radar systems used in this study, processing up to and including (2) is completed in the radio system itself before data is sent to the control PC. All further processing is carried out using MATLAB software developed by the authors utilizing the full wave dispersion solution to estimate Bragg frequency even at shallow waters. The Beamscan direction finding along with the beamforming and MUSIC MATLAB codes used here are available in Cahl et al., (2022), while codes for reading WERA raw data are available in Voulgaris and Cahl (2020).

Application of both beamforming and DF methods require a-priori knowledge of the antenna pattern (i.e., phase and amplitude as a function of boresight direction) for each element of the array. In this study, theoretical antenna patterns [$e^{i\phi_j}$, see (5) for ϕ_j] are used, assuming a constant amplitude (i.e., a radially symmetric monopole antenna pattern). It should be noted here that in addition to extensive tuning, MUSIC also is known to often require antenna pattern measurements for accurate ocean current measurements (Kohut and Glenn, 2003) which were not available in this study.

Table 2.2: HF radar specifications used in this study. Bragg wavelength and other quantities dependent on the operating frequency are calculated using 8.3 MHz. Note: λ_R is the radar transmit wavelength.

Operating frequency (f_R)	8.2-8.4 MHz
Bandwidth (B)	50 kHz
Range resolution (Δr)	3 km
Number of RX antennas (N)	12
Antenna type	monopole (3 elevated radials)
Antenna spacing ($0.45\lambda_R$)	16.25 m
Chirp length (T)	0.4333 s
Chirps per acquisition (M)	2048
Bragg wavelength (λ_B)	18.1 m
Effective depth (m)	1.4 m
Bragg wave frequency (f_B)	0.294 Hz
Transmit array	4 antennas, directed
Transmit waveform	FMCW

The effective depth of the current the HF radar measures (Stewart and Joy, 1974) is approximately 1.4 m (Bragg wavelength divided by 4π). This depth is close to the in situ measurements at SSBN7 (1 m) but only half the depth of the in situ measurements at ADCP1 (3.1 m). However, we still expect high correlation for a 1.7 meter difference in depth at ADCP1. We do not attempt to apply any shear profile to compensate for this difference in depth as the focus of this paper is mainly a comparison between the HF radar algorithms.

2.3.2.1 Beamforming

In order to reduce noise levels, Doppler spectra for beamforming HF radars are typically averages of several individual spectra from overlapping series. In this study, three different FFT analysis lengths were tested for beamforming and Beamscan: a single 2048 point FFT (0.0011 Hz Doppler resolution), three 1024 point windows (0.022 Hz) with 50% overlap, and seven 512 point (0.044 Hz) windows with 50% overlap. The results from each of these FFT analysis lengths were compared against in situ measurements corresponding to a period of a week ("test data", not shown here). It was found that for beamforming, the 512 point windows provide surface currents that agree best (R^2 and RMSD) with the in situ measurements. This window is similar to that used in the manufacturer's software and reduces the frequency resolution by a factor of 4. Beamforming is limited to $\pm 60°$ from the boresight for a 12-antenna linear array. For computational efficiency, the beamform spectrum $B_{r_k,\theta}(f_D)$ is calculated in increments of 1°, resulting in 121 beamformed spectra over the above-mentioned range. However, the beamwidth of $15°$ in our experimental setup suggests that the 121 spectra are not truly independent for each.

For each beamformed Doppler spectrum $B_{r_k,\theta}(f_D)$, the Bragg peaks are identified. The largest peak within the Doppler frequency range± 0.055 Hz around the theoretical Bragg frequency (f_B) which corresponds to a radial velocity range of ± 1 m/s is identified. The required SNR that this peak have was set to 15 dB. This value was selected after trying a range of values (5-25 dB) and comparing the resulting surface currents to those from the “test data” (see above). If it is not above this limit, beamforming does not return a result.

Then the frequency location of this Bragg peak is determined. The accuracy of this estimate is defined by the Doppler frequency resolution (0.0044 Hz) and corresponds to a radial velocity of approximately 8 cm/s. To increase the accuracy above, defined by the resolution of the Doppler spectra, the surrounding 2 points on either side of the peak identified are used to calculate a 5-point SNR weighted peak frequency (e.g., Wang et al., 2014),

$$f_p = \frac{\sum_{i=n-2}^{n+2} f_i\left[B_{r_k,\theta}(f_i)-\sigma_{no}\right]}{\sum_{i=n-2}^{n+2}\left[B_{r_k,\theta}(f_i)-\sigma_{no}\right]}, \tag{2.10}$$

where $B_{r_k,\theta}$ is the spectral energy at frequency f_i, n is the index of the frequency bin that the maximum energy is identified, and σ_{no} is the noise level of the Doppler spectrum. The latter is estimated using the method described in Hildebrand and Sekhon (1974). The radial surface current is estimated from this peak frequency, $u = \left(f_p - f_B\right)\lambda_B$, where f_B and λ_B are the theoretical Bragg frequency and wavelength, respectively.

2.3.2.2 Direction finding

Application of the DF algorithm (7) requires that the Doppler frequencies within the Bragg regions are identified. This identification occurs for each range cell k using the corresponding, averaged Doppler power spectrum, $\overline{P_k}(f_D)$ which is defined as

$$\overline{P_k}(f_D) = \frac{1}{N}\sum_{j=1}^{N} |P_k^j(f_D)|^2, \tag{2.11}$$

where j is the antenna number.

The frequency bins within $\overline{P_k}(f_D)$ where the energy is at least 5 dB above the noise level and within ± 1 m/s of the still-water Bragg peak frequency (i.e., $f_B \pm 0.055$

Hz) are identified. Higher SNR limits (10-15 dB) were assessed but this led to significant reduction to data availability, therefore the 5 dB limit was chosen. In this study, for each frequency f_D within the Bragg region, the Beamscan algorithm calculates a single DOA, while MUSIC is limited to a maximum of 5 DOAs as using a higher or lower DOA limit resulted in decreased accuracy.

For Beamscan, the same three FFT options as for beamforming (i.e., a single 2048 points, three 1024 points with 50% overlap, and seven 512 point with 50% overlap segments) were considered and were compared against the "test data" (not shown here). It was found that the 2048 point FFT, using the entire 14.8-minute acquisition to create Doppler spectra, $P_k^{j=1,N}(f_D)$ with a resolution of 0.0011 Hz (equivalent to surface current resolution of ≈ 2 cm/s) performed best.

MUSIC requires averaging several sub-samples of the received signal to produce the covariance matrix **C**. The minimum number of sub-samples required (M) for creating covariance matrix is the same as the number of antennas available (Tuncer and Friedlander, 2009). In our analysis the 14.8 min data acquisition was split into 1024 point (7.5-minute-long) sub-spectra ($\Delta f = 0.022$ Hz) with 92% overlap creating a total of 13 sub-spectra for the covariance matrix. This results in a surface current resolution (≈ 4 cm/s) only twice that of Beamscan which uses the whole sample. Additionally, 512 point sub-spectra with 75% overlap (13 sub-spectra) were considered for using MUSIC, but this did not perform as well, the results of which are not shown here.

In addition, MUSIC also required tuning for the peak threshold used in MUSIC-highest (Kirincich et al., 2019). Due to the fact that the BLA with 0.45λ element spacing provides much sharper peaks in the MUSIC pseudospectrum than with more compact arrays different DOA peak threshold values were considered in the range of 0.5 to 8.0; the threshold value of 2.0 performed best and it was adopted for use in the analysis presented here.

2.3.3 Surface velocity estimation

For each method, spurious values in the HF radar surface current estimates were identified using a wild point editing method that uses a 5-point median sort filter (Justusson, 1981) and then removed from further analysis. Subsequently each radar derived current time series was linearly interpolated onto the in situ time series. The availability of the post-processed radar current estimates from each method (i.e., beamforming, Beamscan and MUSIC) after wild point removal is listed in Table 1 for both radar sites and all three locations of interest.

Prior to intercomparison the in situ current measurements at locations ADCP1 and SSBN7 (see Fig. 5) are projected into the radial components corresponding to the GTN and CSW radar sites using the radial directions listed in Table 1. The radial current from CSW is multiplied by -1 so that positive values of radial currents from both radar sites denote flow towards 30.5° N (NNE).

2.4 Results

2.4.1 Wave and wind conditions

Nearshore wave and wind conditions were obtained from SSBN7 and buoy 41024 (see Fig. 5), respectively. These stations are located just a few hundred meters from each other, so the data are assumed to be co-located. Wave direction measurements at this location are only available from Nov 1 – Dec 15, 2016. Offshore, wind speed and direction were provided from buoy 41013 (see Fig. 5), which because of its location and range from the coastline it is assumed to provide wind conditions similar to those experienced at ADCP1, the station where directional wave spectra were recorded. These measurements are shown in Fig. 6 and summarized as wind roses in Fig. 7.

The wind direction is predominantly alongshore both nearshore (buoy 41024, Fig. 7b) and offshore (buoy 41013, Fig. 7a), like the climatological averages found by Wu et al., 2017. Nearshore winds are variable 0-10 m/s, often fluctuating near the 5.3 m/s minimum wind speed required for the generation of 18.1 m (0.294 Hz) Bragg waves (see Fig. 6a) corresponding to the 8.3 MHz radar operating frequency (Shen et al. 2012). Offshore winds are stronger, in the range of 5 to 15 m/s, mostly above the 5.3 m/s Bragg minimum.

Wave directions offshore (ADCP1, Fig. 7c) are variable, where waves come from between east and south, with a slight preference to the southeast. Most of the time, offshore wave height is < 1 m, however there are periods where higher wave heights are observed (Fig. 6c). The wave frequency spectrum (Fig. 6e) at this location shows wind driven seas with a smooth high frequency tail measurable above the Bragg frequency (0.294 Hz), indicated by a white line.

In the nearshore (SSBN7, Fig. 7d), when wave direction measurements were available (red line in Fig. 6d), waves are mainly from the south-southeast, perpendicular to the local coastline at this location. During July, nearshore wave heights are slightly larger than those recorded at ADCP1, while in October and thereafter nearshore wave heights are $<$ 1 m and smaller than those recorded offshore (ADCP1). Measurements of the high frequency Bragg waves were not available at SSBN7.

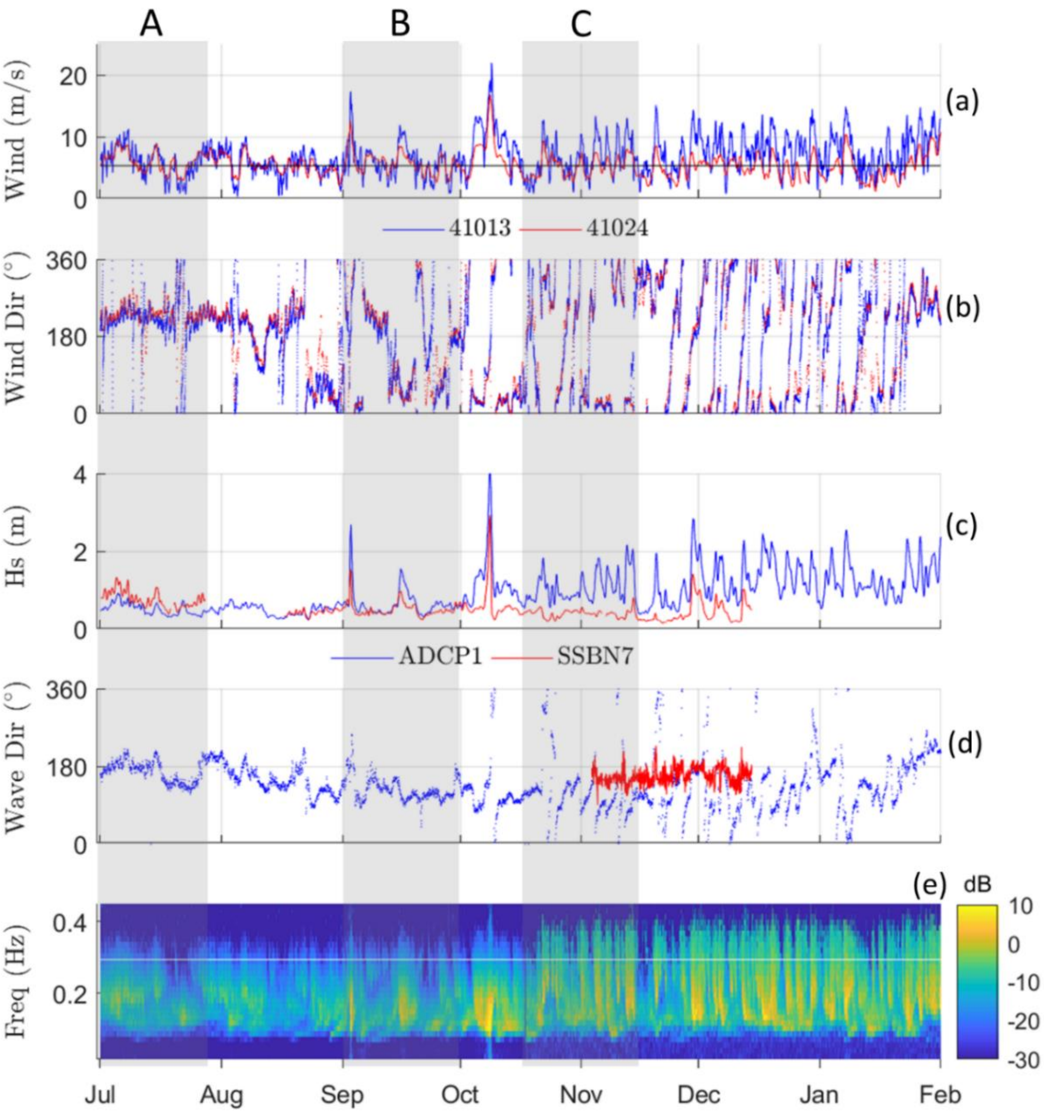

Figure 2.6: Time-series of: (a) wind speed measured offshore (NDBC buoy 41013, blue line) and nearshore (NDBC buoy 41024, red line). The theoretical minimum wind speed required to locally generate Bragg waves for the 8.3 MHz radar sites is shown as black line. (b) Offshore (blue) and nearshore (red) wind direction. (c) Significant wave height measured at sites ADCP1 (blue) and SSBN7 (red). (d) Wave direction for ADCP1 and SSBN7 as in (c). (e) Time-stack of wave energy frequency spectra for site ADCP1 (white line indicates frequency of Bragg ocean waves for an 8.3MHz HF radar).

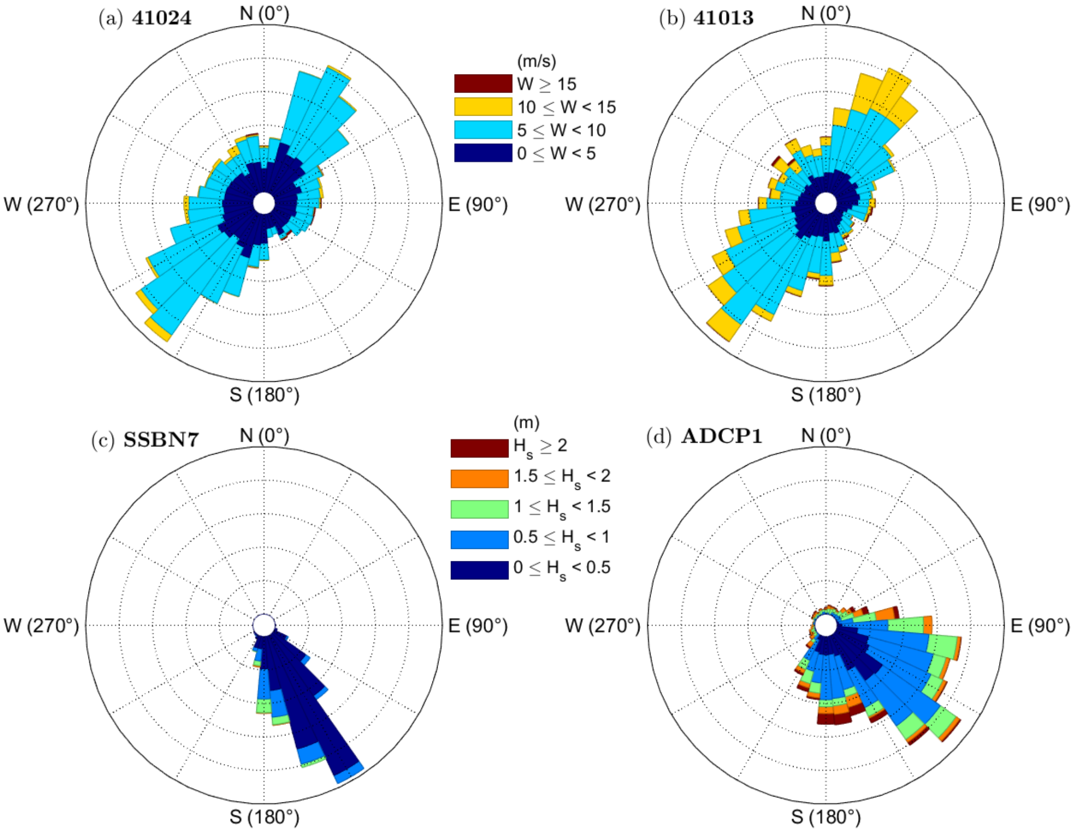

Figure 2.7: Synoptic wind and wave conditions for the period of study shown as rose diagrams. Wind conditions at (a) NDBC buoy 41013 (offshore) and (b) buoy 41024 (nearshore, near site SSBN7). Wave height and peak wave energy direction for sites ADCP1 and SSBN7 are shown in (c) and (d), respectively.

2.4.2 Doppler spectra estimates

Doppler spectra for each antenna for the range cell and beam direction corresponding to the ADCP1 location, are shown in Fig. 8 and 9 for GTN and CSW, respectively. Only a limited range of Doppler spectrum frequencies around the still water Bragg frequency is shown for clarity. The Bragg peaks are clearly visible in the spectra for both positive (waves coming towards the radar site) and negative (waves going away from the radar site) Doppler frequencies. It is noticeable that for GTN antennas 5 and 7 had low SNR in October and November. For CSW, antennas 3 and 8 had almost no signal and were effectively not operational during the periods, Jul 1 – Oct 15, and Oct 15 – Jan 31, respectively.

The antenna malfunctions noted above suggest that beamforming for CSW may be less effective than theoretically predicted for a 12-antenna linear array. For GTN, the lower SNR in antennas 5 and 7 during October and November may result in lower beamforming performance during those times. However, the same signal is used in all methods (beamforming, Beamscan and MUSIC) utilized in this analysis and this should not affect the intercomparison of the methods, although MUSIC is known to be sensitive to these antenna issues unless antenna grouping is used (Dumas and Guérin, 2020). Furthermore, these are realistic situations representing common issues in operational oceanography, especially for HF radar sites subjected to storm, coastal erosion and/or cable damage that results in performance deterioration.

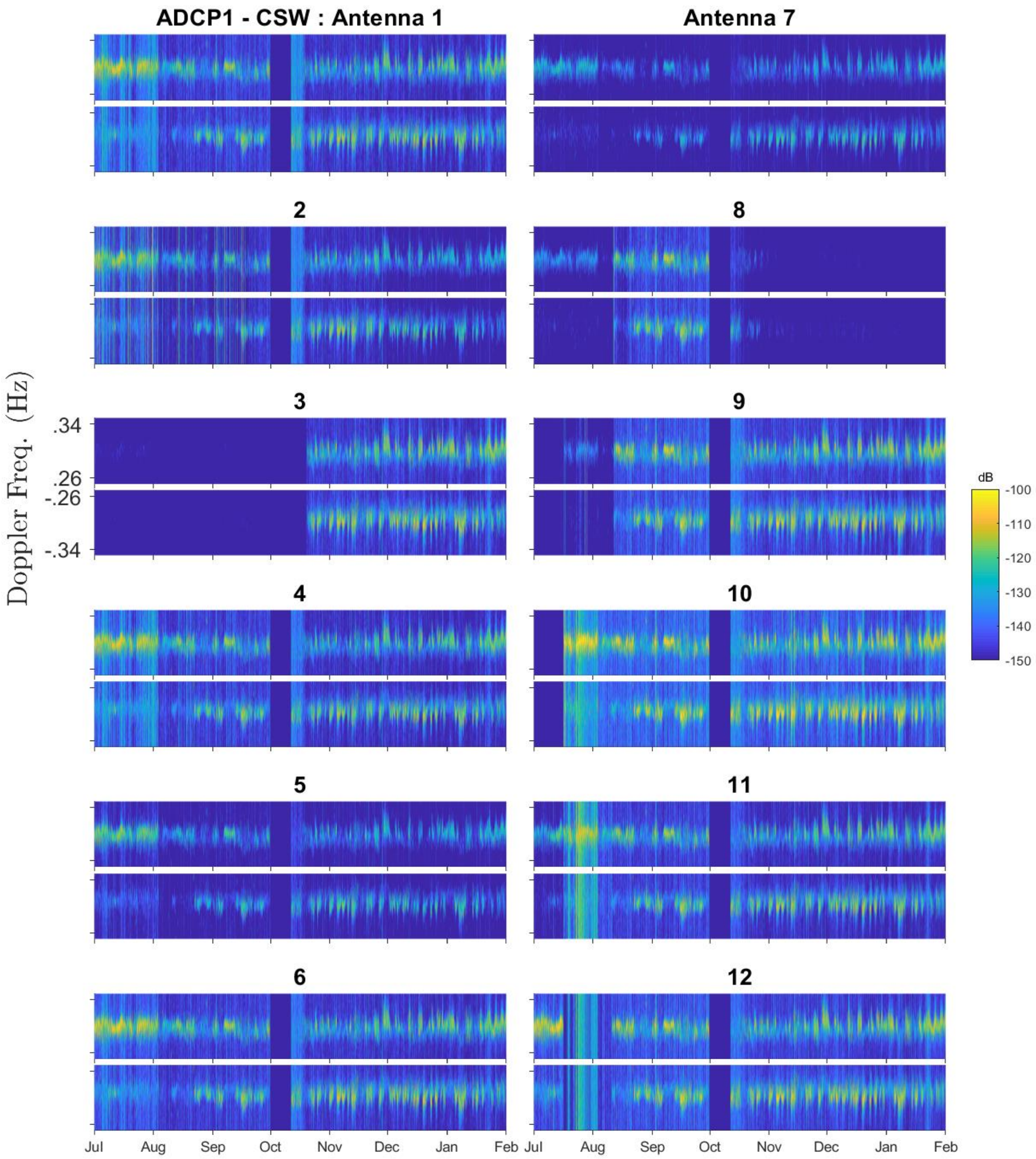

Figure 2.8: Doppler spectra for GTN antennas 1-12 for the range cell

Figure 2.9: Doppler spectra for CSW antennas 1-12 for the range cell corresponding to the location of ADCP1.

2.4.3 Radial current estimates

There is a significant amount of literature on optimizing MUSIC, specifically for HF radar current estimates with compact antenna systems (e.g., Barrick and Lipa, 1999;

Kirincich et al., 2019). Recent research has shown grouping antenna elements together into groups and averaging across these groups can be combined with self-calibration (as opposed to antenna pattern measurements) to increase the accuracy of MUSIC further (Dumas and Guérin, 2020; Guérin et al., 2021). However, specific grouping and tuning parameters are site specific (Lorente et al., 2022). This is not considered within this paper, as the main focus is to compare easily implemented direction finding algorithms for a BLA radar system.

Radial current estimates from CSW and GTN using the three methods (beamforming, Beamscan and MUSIC) were made for all three locations (ADCP1, SSBN7, and MDPT) and these are compared against the in situ data for ADCP1 and SSBN7 and between the two radar sites at MDPT. The results are shown as scatter plots in Fig. 10, and as a Taylor diagram in Fig. 11. Statistical analysis of the comparisons included estimations of correlation (R^2), regression (slope, s), bias, root-mean-square difference (RMSD) and RMSD normalized by the standard deviation of the in situ velocities (NRMSD) and the results are listed in Table 3. We note here that the p-values for the R^2 and slopes are all very close to zero except for radar CSW at SSBN7 using beamforming, where the R^2 is zero and the p-value is 0.04. The Taylor Diagram (Fig. 11) allows the comparative assessment of the different methods using the correlation coefficient, NRMSD, and the standard deviation, the closer the results lie to the in situ measurements the better they agree (Taylor, 2001). Fig. 11 suggests that all methods perform similarly at ADCP1. However, at SSBN7 and MDPT, beamforming (circles) performs worse than MUSIC (squares) and Beamscan (triangles). This is described in more detail below.

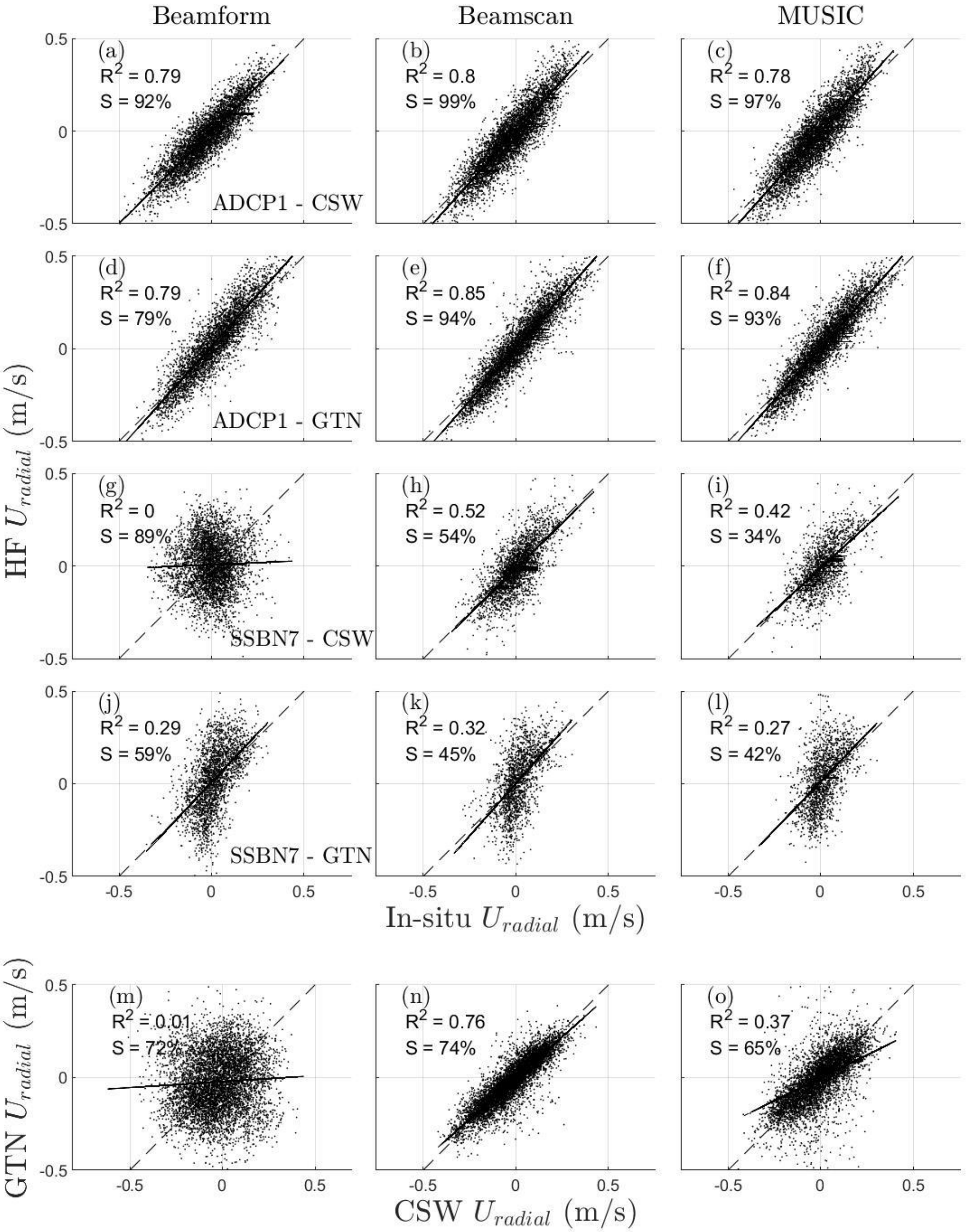

Figure 2.10: Scatter diagrams of HF radar radial velocity estimates derived using the beamforming (left column), Beamscan (middle column) and MUSIC (right column) methods against in situ measurements (a-l) and MDPT (m-o). The linear regression and the 1:1 lines are shown as solid and dashed lines, respectively. The S values represent the percentage of time each particular method provided a solution.

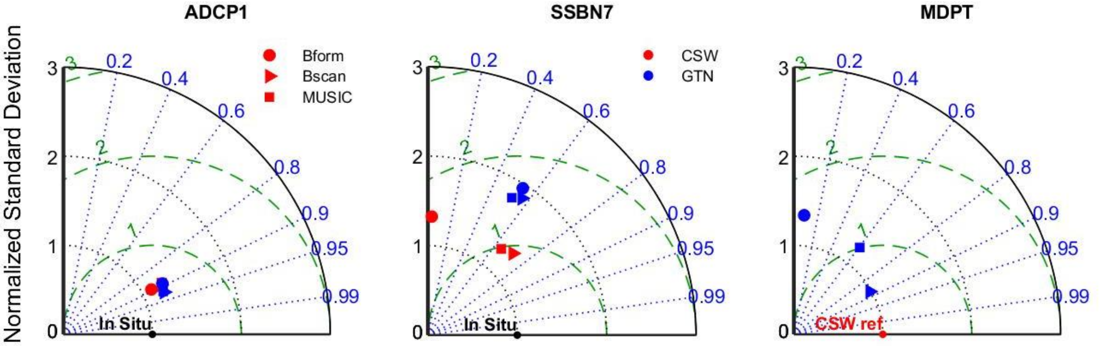

Figure 2.11: Taylor diagrams for radial current comparisons from Jul 1, 2016 – Jan 31, 2017 at sites ADCP1 (left), SSBN7 (middle) and MDPT (right). Normalized RMSD is shown as the dashed green lines.

2.4.3.1 Beamforming

At location ADCP1, beamforming derived HF radar surface currents (Fig. 10a, d) correlate well with the in situ currents with $R^2 = 0.79$ for both CSW and GTN. The scatter is low with RMSD of 7.0 and 8.5 cm/s and NRMSD of 0.5 and 0.57 for CSW and GTN, respectively (see more statistics in Table 3).

For SSBN7 and MDPT locations, corresponding to higher steering angles from the radar boresight than ADCP1 (Table 1), beamforming radial current estimates do not compare as favorably with the in situ currents (see Fig. 10g, j, m). The disagreement is more pronounced for the estimates from CSW at SSBN7 where no correlation is found ($R^2 = 0$) while for GTN the correlation is still low ($R^2 = 0.29$). Similarly, no correlation ($R^2 = 0.01$) is found at MDPT. The RMSD value at location SSBN7 is almost double than that at location ADCP1 with values of 16 and 14 cm/s, and NRMSD is almost triple with values of 1.32 and 1.64 for CSW and GTN, respectively (see Table 3). At MDPT, the RMSD between the radar sites is similar (14 cm/s) to the RMSD between the radars and in situ measurements at SSBN7.

Table 2.3: HF radar comparison statistics: slope (s), bias (in cm/s), correlation coefficient (R^2), RMSD (in cm/s) and NMRSD for the different methods of radar signal analysis.

Site	Radar	Beamforming				Beamscan				MUSIC			
		s	bias	R^2	RMSD	s	bias	R^2	RMSD	s	bias	R^2	RMSD
ADCP1	CSW	0.99	-0.2	0.79	7.0	1.1	-1.6	0.8	7.7	1.1	-.15	0.78	8.1
	GTN	1.1	1.4	0.79	8.5	1.1	0.3	0.85	7.1	1.1	0.5	0.84	7.2
SSBN7	CSW	0.04	0.8	0	16	0.99	-1.2	0.52	9.3	0.92	-0.8	0.42	9.9
	GTN	1.06	0.9	0.29	14	1.1	0.1	0.32	13	1.04	1.1	0.27	13
MDPT		0.06	-2.2	0.01	14	0.89	-0.3	0.76	6.4	0.49	-0.2	0.37	10

2.4.3.2 Beamscan

Radial estimates using the Beamscan method show a reasonable correlation with the in situ radials at ADCP1 ($R^2 = 0.8$ and 0.85 for CSW and GTN, respectively; see Fig. 10b, e). It is worth noting that at this location the steering angles ($-4.9°$ and $9.4°$ for CSW and GTN, respectively) are small. The regression lines have slopes slightly above 1, (1.1 for both CSW and GTN) and the bias is 0.1 cm/s for GTN and -1.2 cm/s for CSW (see Table 3). The percentage of time the method provided a solution (S) is 99% and 94% while the RMSD is 7.7 and 7.1 cm/s and NRMSD is 0.55 and 0.48 for CSW and GTN, respectively.

At SSBN7 Beamscan radial current estimates show more scatter than at MDPT (see Fig. 10h, k, n). At SSBN7, the correlation for CSW ($R^2 = 0.52$) is higher than for GTN ($R^2 = 0.32$) while at MDPT, the radars correlate well with each other ($R^2 = 0.76$).

S is higher for CSW (54%) than GTN (45%) at SSBN7 while at MDPT solutions were obtained for 90% and 81% of the time for CSW and GTN, respectively (see Table 1). At SSBN7, the RMSD is up to 50% higher than at location ADCP1 with values of 9.3 and 13 cm/s and NRMSD of 0.94 and 1.64 for CSW and GTN, respectively (see Table 3), while at MDPT location the RMSD (6.4 cm/s) is similar to that found for location ADCP1.

2.4.3.3 MUSIC

MUSIC HF radar surface current estimates at location ADCP1 show similar correlation ($R^2 = 0.78$ and 0.84 for radar sites CSW and GTN, respectively) than beamforming and Beamscan (Fig. 10c, f). The slope is close to 1 for both radar systems (0.92 and 1.04 for CSW and GTN, respectively) and no significant bias in the estimates is found (Table 3). The method provided solutions for 97% and 93% of the time for CSW and GTN, respectively; the RMSD is 8.1 and 7.2 cm/s and NRMSD of 0.58 and 0.48 for CSW and GTN, respectively.

At the nearshore location SSBN7 (Fig. 10i, l), higher correlation is found for CSW ($R^2 = 0.42$), than GTN ($R^2 = 0.27$). At MDPT, the radar current estimates have low correlation with each other as indicated by $R^2 = 0.37$ (Fig. 10o). At SSBN7, MUSIC provided solutions for 34% and 42% of the time, for CSW and GTN, respectively; these percentages are much lower than those found at location ADCP1. For MUSIC, there is better solution recovery at MDPT location (74% and 88%, for CSW and GTN, respectively - see Table 1). At SSBN7, the RMSD is 9.9 and 13 cm/s with NRMSD values of 1.1 and 1.7 for CSW and GTN, respectively (Table 3); a RMSD value of 10 cm/s is found at MDPT.

2.4.4 Effect of wind and wave conditions

To assess the accuracy of the different methods under different wind and wave conditions, representative events denoted as A, B and C (see Fig. 6) are selected for further examination. During event A (Jul 1 - 27, 2016), nearshore wave height at SSBN7 is higher than that at ADCP1 (Fig. 6c) although the wind speeds (Fig. 6a) are variable (0-10 m/s) their magnitude is similar at both nearshore and offshore locations. Wave heights are similar at both locations for event B (Sep 1 - 30, 2016), although the winds near ADCP1 are slightly higher than those at SSBN7. During event C (Oct 15 - Nov 15, 2016), ADCP1 is experiencing significantly larger wave heights and winds than SSBN7. For site GTN, all antennas perform well (high SNR) during events A and B but have low SNR in both antennas 5 and 7 during event C. At site CSW, antenna 3 has low SNR during events A and B while antenna 8 has low SNR during event C.

For each event, as before, radial current estimates from CSW and GTN are compared to the in situ data and the estimates between the two radar sites at MDPT. Taylor Diagrams in Fig. 12 summarize the accuracy of the different HF radar methods during each event at each location (ADCP1, SSBN7 and MDPT). For all events, the HF radar velocities correlate well with the in situ measurements at ADCP1 independently of the method used. At MDPT and SSBN7 beamforming has the lowest correlation for all events. On average, at SSBN7, Beamscan and MUSIC perform similarly while at MDPT Beamscan performs better than MUSIC.

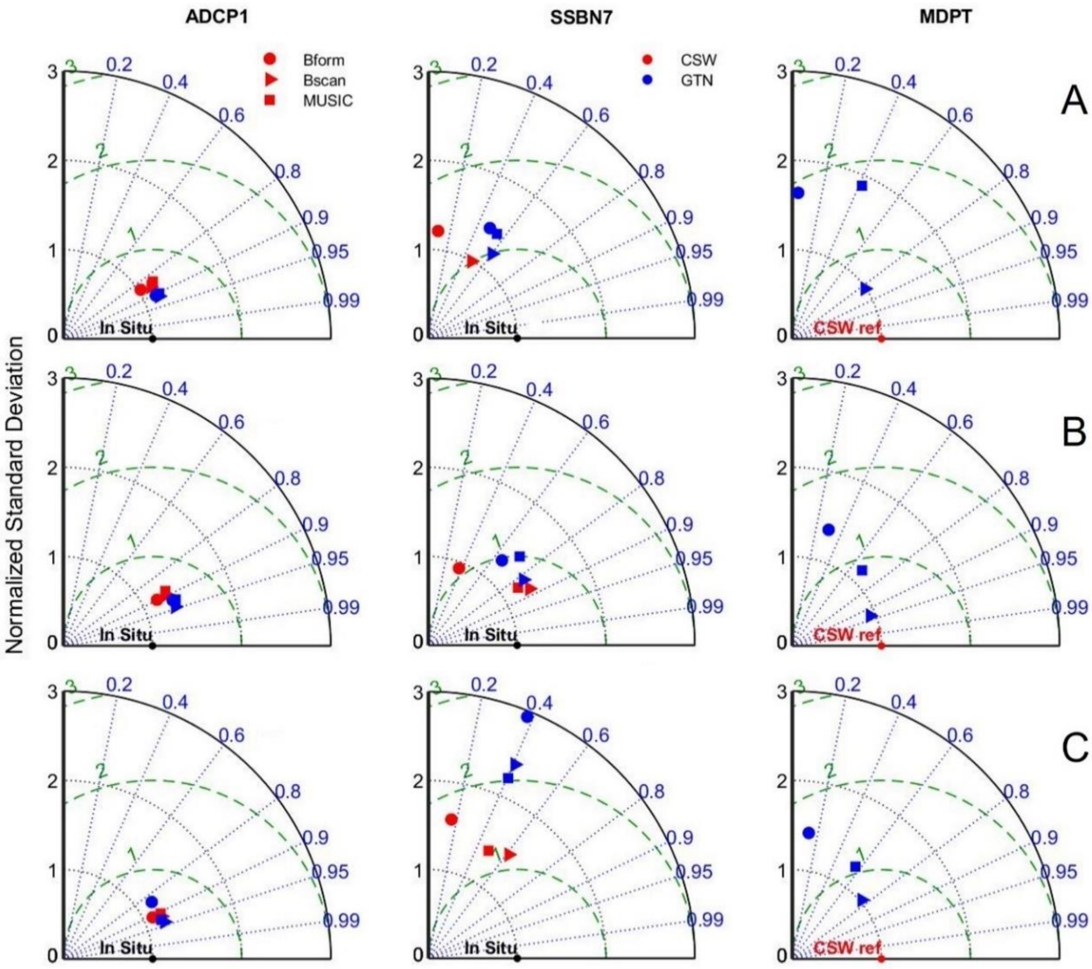

Figure 2.12: Taylor Diagrams for radial current comparisons during events A-C that correspond to the different time periods shown in Fig. 6.

Event C is most representative of the climatological average with winds stronger offshore and wave heights larger offshore (Wu et al., 2018) and it is selected for a more detailed examination. Time-series of the radial current estimates during event C, from each method and location, are shown in Fig. 13. At ADCP1, all three HF radar methods agree well with the in situ measurements (see Fig. 13a, b) as indicated by the good correlations found (Fig. 12, left column). The tidally modulated current is clearly seen in the HF radar surface current estimates in agreement with the in situ records. At SSBN7 and MDPT, MUSIC and Beamscan are noisy (Fig. 13c-g) while the beamforming estimates at SSBN7 clearly capture a tidal modulation (red line in Fig. 13c) as it was the case at ADCP1.

The performance of the three methods at MDPT are shown in Fig. 13e, f, g. Beamforming (Fig. 13e) estimates from the two radar sites are not consistent. At this location both systems should be reporting identical currents but instead the estimates, although they capture a tidal signal, appear to be out of phase for a good part of the record. However, Beamscan (Fig. 13f), and MUSIC (Fig. 13g) show better agreement with each other. For both Beamscan and MUSIC the errors in velocities seem random.

2.4.5 Effect of beamforming's beam pattern

Beamforming creates a 'beam' in the direction of the intended measurement direction [see (2.6)]. Theoretically, the beam pattern is narrow (15° beamwidth along the radar boresight) for a 12 antenna linear array with half wavelength spacing and the side lobe suppression is ~40 dB. Fig. 14 shows theoretical beam patterns for the 12 antenna receiving arrays (CSW and GTN), pointed towards the three measurement locations. Although the beamwidth is significantly larger at the direction toward SSBN7 (Fig. 14c, d: steering angle = -59.1° and 47.9° for GTN and CSW, respectively) than at ADCP1 (Fig. 14a, b: steering angle = 9.4° and -4.9° for GTN and CSW, respectively), the sidelobes are suppressed by almost 40 dB in both cases.

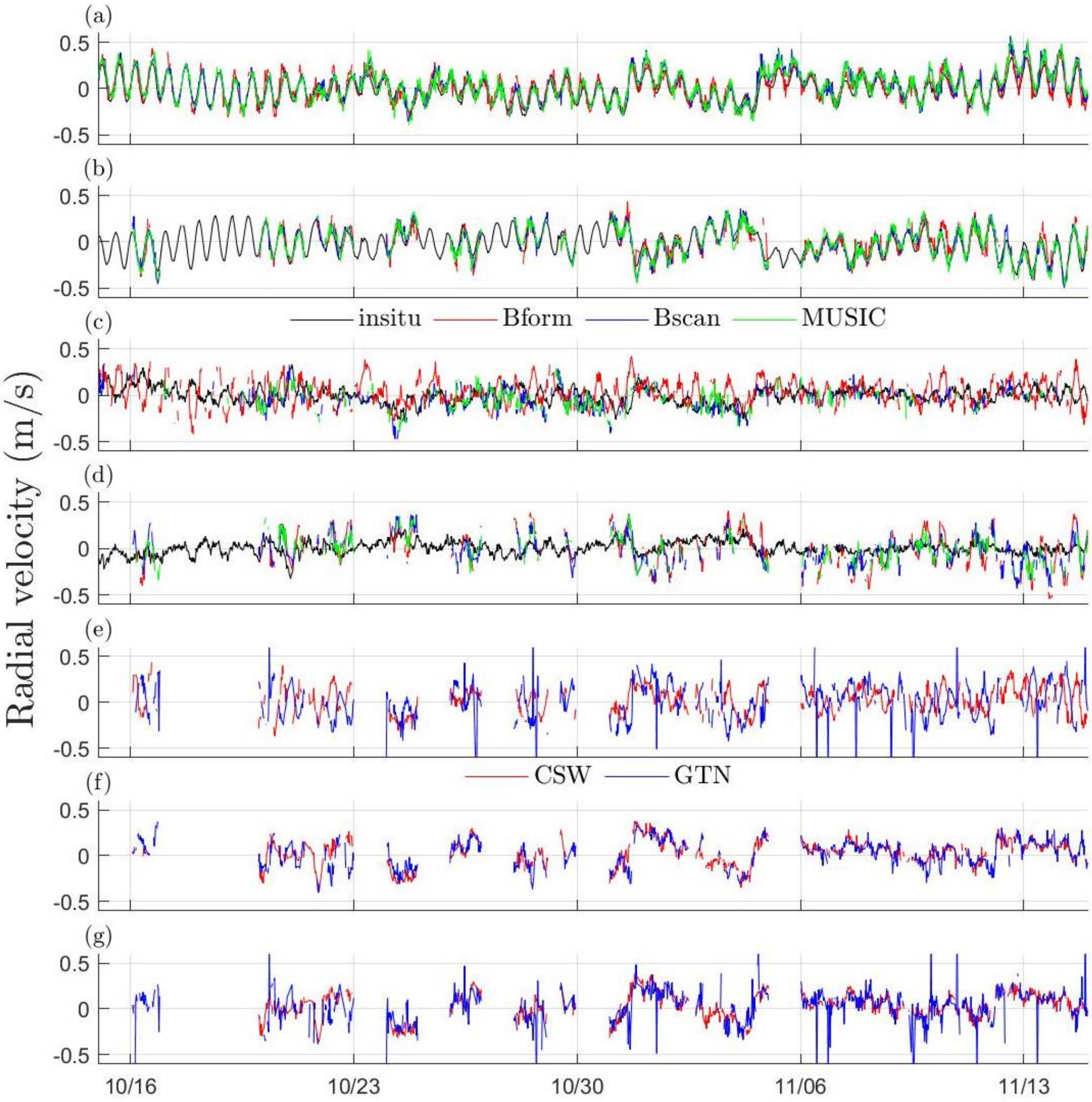

Figure 2.13: Event C time-series of in situ and HF radar surface currents obtained with the three different methods of analysis (beamforming, Beamscan and MUSIC shown in red, blue, and green lines, respectively). (a) GTN and (b) CSW for offshore site ADCP1; (c) GTN and (d) CSW for nearshore site SSBN7. The radial currents from CSW (red line) and GTN (blue line) for MDPT for (e) beamforming, (f) Beamscan, and (g) MUSIC.

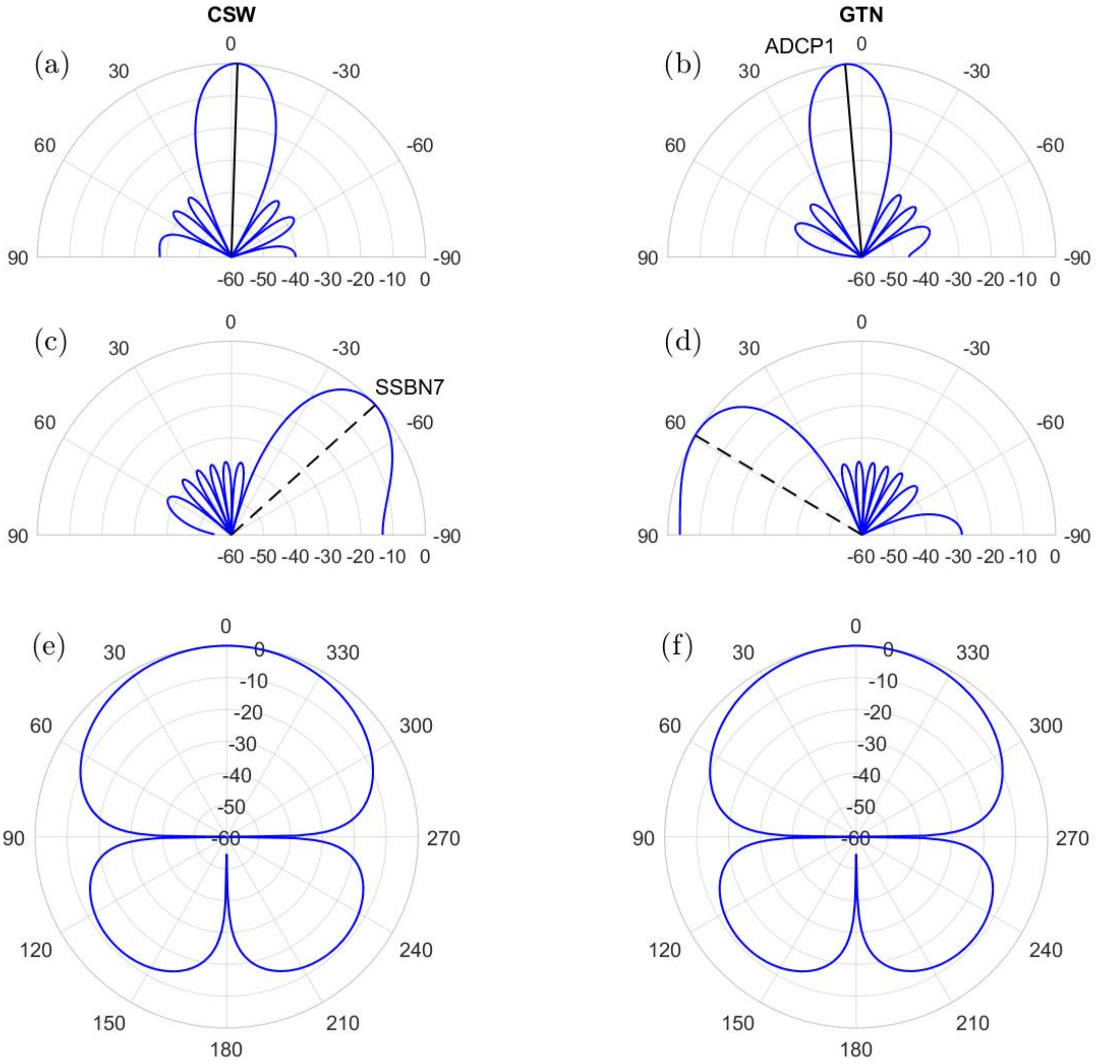

Figure 2.14: Theoretical RX beam patterns (a-d) for a 12-antenna linear array with 0.45λ antenna spacing using a Hamming window and for steering angles corresponding to those toward the comparison sites. (a) CSW-ADCP1 (steering angle $\theta_{st} = -4.9°$); (b) GTN-ADCP1 $\theta_{st} = 9.4°$); (c) CSW-SSBN7 ($\theta_{st} = 47.9°$); (d) GTN-SSBN7 ($\theta_{st} = -59.1°$); Theoretical transmit patterns for (e) CSW and (f) GTN using idealized antenna positions for the TX arrays (0.5λ by 0.15λ spacing with a phase delay of 0.35λ for the rear antennas).

According to radar theory, the signal scattered from Bragg waves is proportional to the Bragg wave height along the radar site radial direction (Barrick, 1972). The beamformed Doppler spectrum at a certain range (r), and steering angle (θ_{st}) is a convolution of the RX beam pattern $\left[B_{r,\theta_{st}}(\theta)\right]$ where θ is measured from the radar boresight, and the Bragg wave height $H_B(r,\theta)$ along the semicircle with a radius r. If we consider the theoretical beam patterns shown in Fig. 14a-d, the Bragg wave height would have to be 20 dB higher (giving a 40 dB difference in the radar cross section) somewhere along the semicircle of range r to overpower the sidelobe suppression. This would result in the beamformed Doppler spectrum containing information from this unintended direction. In most environments this is not expected to impact a beam forming radar system with 12 antennas if they perform as theory suggests (Laws et al., 2000). However, real antenna patterns often deviate from the theoretically estimated ones. Gurgel et al., 1999 has shown that for a linear array a variation in distance from the waterline along the RX array can reduce sidelobe suppression by 15 dB. Preliminary antenna pattern measurements in CSW using a small quadcopter (Cahl and Voulgaris, 2016) suggested significantly higher sidelobes than the theoretically predicted.

In addition, the 4-element transmit array used in WERA systems is a rectangular array that directs most of the radar signal towards the ocean with an approximately 80° beamwidth (see Fig. 14e, f). Multiplying the TX and RX pattern results in an effective beam pattern, shown as the solid lines in Fig. 15. For location ADCP1 the effective beam patterns have smaller sidelobes by a few dB while at location SSBN7 the sidelobes are increased by 5 and 10 dB for CSW and GTN, respectively.

Furthermore, the performance the RX array as a whole depends on the quality of the individual antenna elements. At CSW, antenna 3 had little to no signal for the first half of the study period. After antenna 3 was fixed, antenna 8 was damaged and had little to no signal for the second half of the study period (see Fig. 9). At GTN, antennas 5 and 7 were damaged and exhibited low SNR during event C (see Fig. 8). The effects of reduced antenna element performance are assessed by calculating effective beam patterns (including the effect of the TX pattern) with the malfunctioning antennas removed. With antennas 3 and 8 removed (see Fig. 15) the change in the effective beam patterns is similar for CSW and GTN. This modification results in reduced sidelobe suppression of 30 and 20 dB, respectively for site ADCP1 and 20 and 10 dB for SSBN7.

This reduced sidelobe suppression suggests that beamforming measurements at SSBN7, with antenna 8 performing poorly at CSW, would be inaccurate if the Bragg wave height varies by more than a factor of $\sqrt{10} \cong 3.3$ (since the radar cross section is proportional to spectral energy, or wave height squared) along the semicircle corresponding to the range of SSBN7 from site CSW. This sidelobe suppression of only 10dB could allow the Bragg scattered HF radar signal from other directions to overwhelm the beam pattern steered towards to SSBN7.

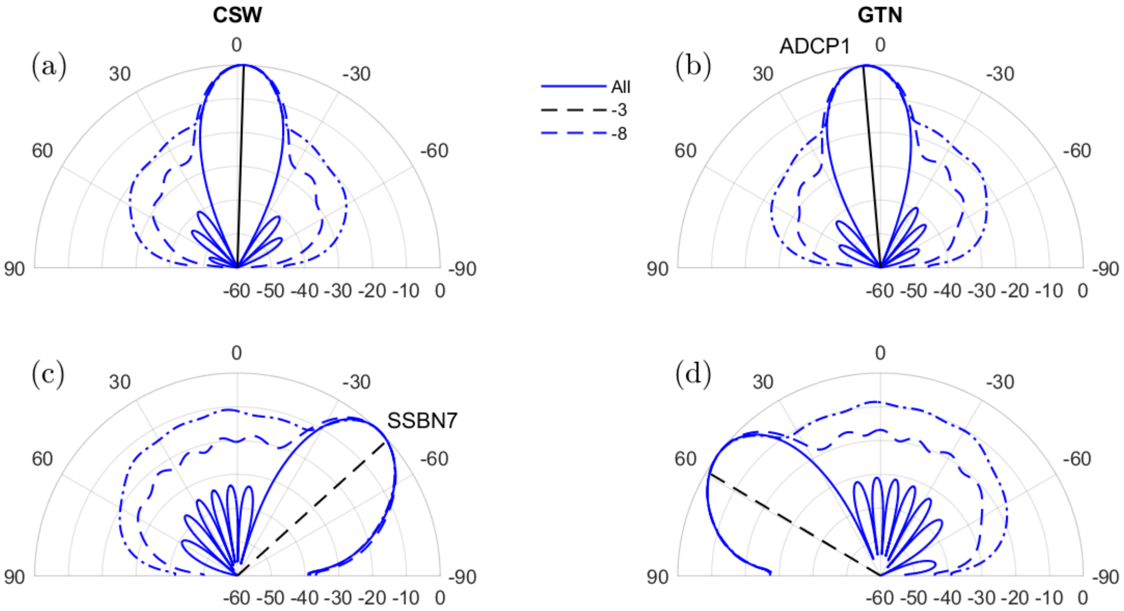

Figure 2.15: Theoretical beam patterns for a 12-antenna array after accounting for the TX antenna pattern (see Fig. 14e, f). (a) CSW-ADCP1 ($\theta_{st} = -4.9°$); (b) GTN-ADCP1 $\theta_{st} = 9.4°$); (c) CSW-SSBN7 ($\theta_{st} = 47.9°$); (d) GTN-SSBN7 (θ_{st}=$-59.1°$). Solid lines show the effective beam pattern when all antennas are functioning. Dashed and dash-dot lines show the pattern with antenna 3 and antenna 8 removed, respectively. Solid black lines denote the direction towards ADCP1 while the dashed black lines denote the direction toward SSBN7.

2.4.6 Theoretical evaluation of beamforming and Beamscan

In this section beamforming and Beamscan are evaluated using the method of Wang and Gill (2016). Modelled Doppler spectra for each HF radar antenna are created and then surface current analysis is carried out on these theoretical spectra. Wang and Gill (2016) evaluated MUSIC vs beamforming, but they did not use the directional characteristics of the TX array, something that is included in here.

For a single range bin, prediction of the Doppler spectrum for each antenna requires knowledge of the wave and current fields at every point along the range ring. Since wave and current information exist only for two locations in this study (ADCP1 and SSBN7), full Doppler spectrum estimation for each antenna is not possible using in situ data. Therefore, an idealized EM backscattering model is used to estimate Doppler spectra in each antenna (for a single range bin) using two different surface current scenarios. Subsequently, Beamscan and beamforming is performed to estimate surface currents which are compared to the surface current inputs of the model.

The Wang and Gill (2016) model used here simulates the first order spectrum (Bragg peak) and does not consider second order effects. The model estimates the signal in each antenna j by summing the signal received from each radial direction θ from the boresight:

$$s(t)_j = \sum_\theta \left[A_p(\theta)e^{2\pi i(f_B+f_c)t} + A_n(\theta)e^{-2\pi i(f_B-f_c)t} + \phi_j(\theta)\right] + noise \qquad (2.12)$$

where f_B is the Bragg frequency and f_c is the Doppler shift due to the radial current $u_r(\theta)$. The phase shift ϕ_j for each antenna j is given by (5). The spectral amplitudes of Bragg waves traveling towards and away from the radar are represented by A_p and A_n, respectively. This idealized model assumes a fully developed sea where the Bragg wave spectral energy $[S_w(f_B,\theta)]$ is determined by the directional characteristics of the wave field which is assumed to be $\cos^4$ (e.g., Longuet-Higgins et al., 1963)

$$S_w(f_B,\theta) = S_w(f_B)\cos^4\left(\frac{\theta-\theta_w}{2}\right) + 0.01 \qquad (2.13)$$

where the wind direction is given by θ_w and θ is the angle measured from the boresight. The synthetic signal (12) generated consists of 2048 samples with a chirp length of 0.43333 seconds (the same as the radar system used in this study). Random Gaussian noise is added to the signal so that the SNR of the larger Bragg peak to the noise in the Doppler spectrum [the Fourier Transform of $s(t)_j$] is either 20 dB (high SNR case) or 10 dB (low SNR case). For the model runs discussed here, the wind direction is directed towards the radar site, along the radar boresight and the beam patterns are those shown in Fig. 14, 15.

Two synthetic current flows were considered, similar to Wang and Gill (2016): (i) a constant speed current flowing parallel to the coast, depicted in Fig. 16 (top panel) and (ii) a parallel current to the coast as in (i) with large cross-shore flow (i.e., river outflow) depicted in Fig. 17 (top panel). In the latter case, this ‘burst’ or cross-shore flow resembles a Gaussian distribution of radial velocity with the peak speed located at $\theta = -20^\circ$ (Fig. 17a). After the modelled signals (12) and corresponding Doppler spectra are created, Beamscan and beamforming (as described in section 3) are used to estimate radial currents. As in Wang and Gill (2016), this is repeated 100 times for each method and then the estimated radial currents are bin averaged (1° bin size) radials current estimates are shown in Fig. 16a-d and 17a-d.

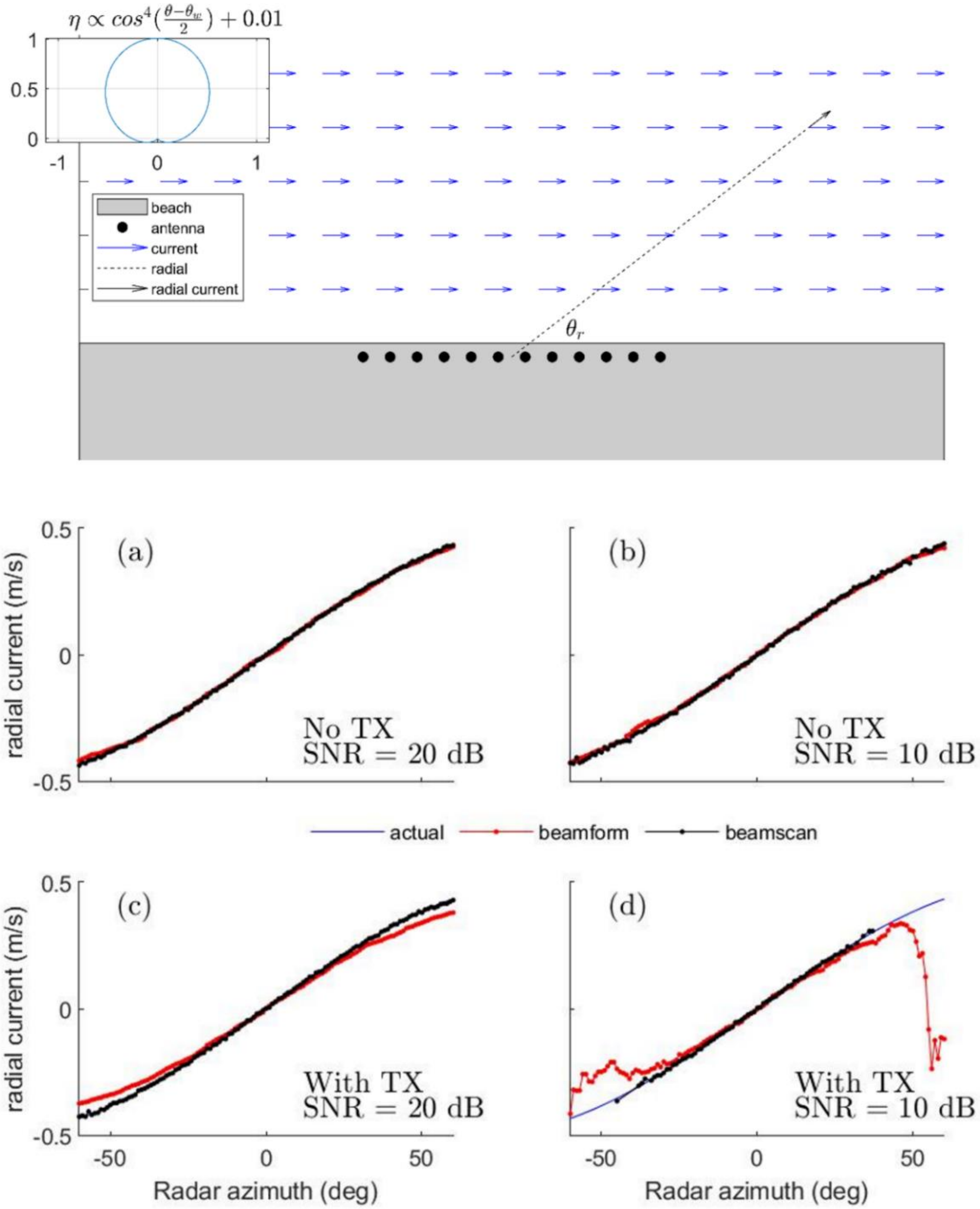

Figure 2.16: Top panel: Schematic of flow conditions for the constant current profile case used to drive the HF radar forward model. Bottom panel: Comparison of Beamscan and beamforming current estimates without (a, b) and with (c, d) TX pattern included and for high (20dB) and low (10 dB) SNR.

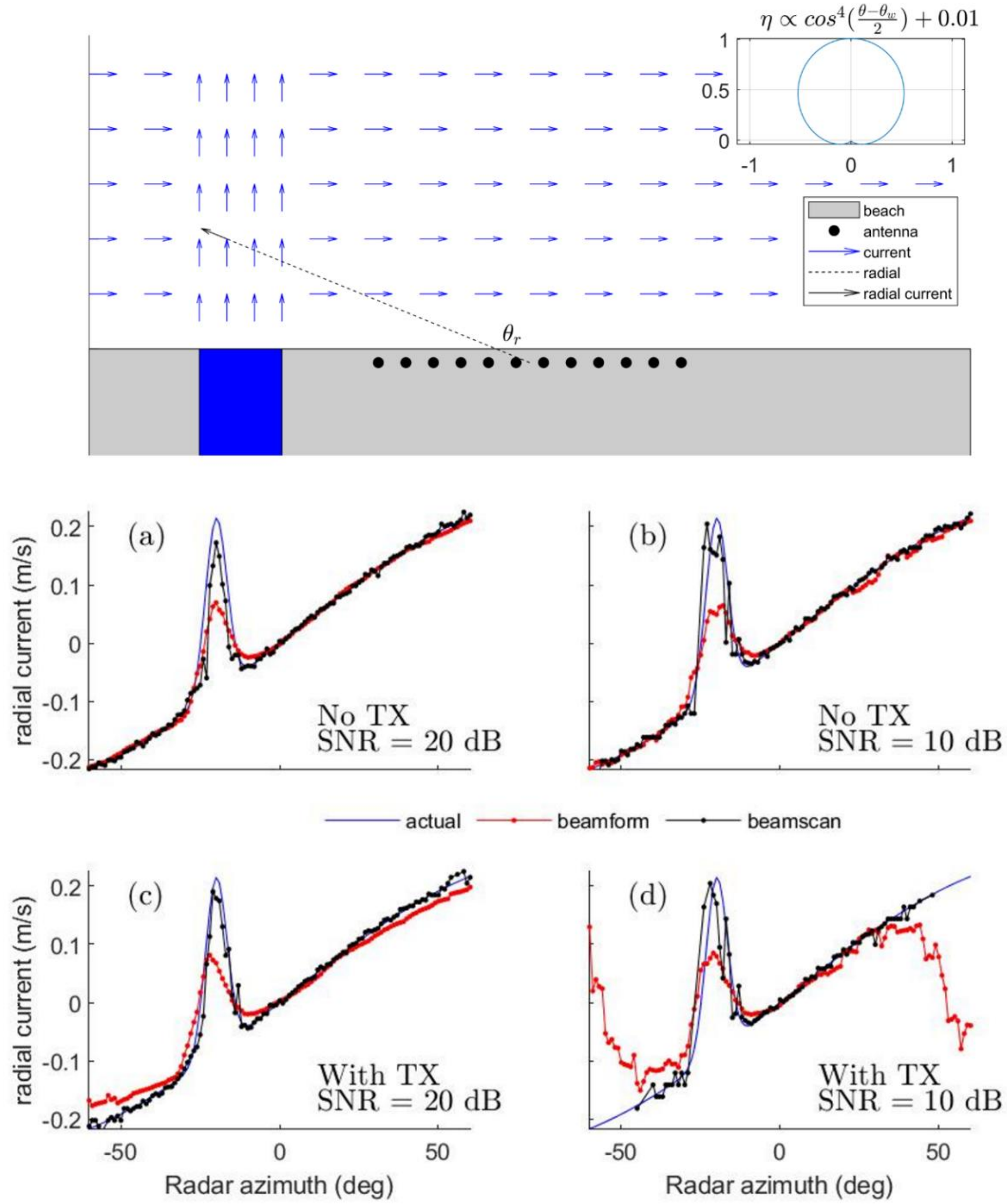

Figure 2.17: Top panel: Schematic of flow conditions for the Gaussian radial current profile case used to drive the HF radar forward model. Bottom panel: Comparison of Beamscan and beamforming current estimates without (a, b) and with (c, d) TX pattern included and for high (20dB) and low (10 dB) SNR.

For a uniform current profile both Beamscan and beamforming estimates agree well with the synthetic flow when not accounting for the transmit pattern (Fig. 16a, b). When accounting for the transmit pattern, Beamscan performs well in both the low and higher SNR cases (Fig. 16c, d) but fails to produce results for beam angles greater than 50° in the low SNR case. For beamforming, the low SNR case (Fig. 16d) has large inaccuracies at beam angles > 40° while the deviations at these high angles are smaller for the high SNR case (Fig. 16c).

For the Gaussian ‘burst’ profile (Fig. 17), Beamscan performs well in all cases and captures the Gaussian profile almost completely. However, it does not return current estimates at beam angles > 50° in the low SNR case when accounting for TX (Fig. 17d). Beamforming does identify the Gaussian current profile for all cases but only at roughly half the amplitude of the model input Gaussian. As described earlier when accounting for TX, beamforming estimates deviate from the synthetic ones at higher radial angles and the deviation is bigger for lower SNR (Fig. 17c, d).

The results here show Beamscan to be better than beamforming in capturing the Gaussian burst current profile, which is similar to the results of Wang and Gill (2016) that found MUSIC to outperform beamforming in these cases. Additionally, when accounting for the transmit pattern, we find that at high beam angles beamforming produces less accurate results while Beamscan is less likely to produce results especially at low SNR cases. It should be noted that in all cases the wind was directed towards the radar boresight.

2.5 Discussion

2.5.1 Source of radial estimates errors

Intrinsic angular biases are known to exist in both DF- CCL systems and BLA radar systems (Emery et al., 2014; Cosoli and Stewart de Vos, 2019). A similar analysis is done here for location ADCP1 using beamforming, Beamscan, and MUSIC (see Fig. 18). The radial HF radar currents are compared to the in situ radial currents at ADCP1 for different bearing angles of the radar. The true direction of ADCP1 is shown as the gray dashed line in Fig. 18. For CSW, both R^2 and RMSD values show the best correlations and minimum difference with the in situ data at angles within 2° of the true direction (Fig. 18a,b) for all methods. At GTN, the best correlation (R^2) with the in situ data is within 2° in bearing direction from the true direction of ADCP1 using any method (Fig. 18c) while the best RMSD values are within 4° (see Fig. 18d). It should be noted here that the direction finding methods decorrelate faster than beamforming, especially for CSW (Fig. 18a,b).

Overall, our HF radar measurements corresponding to SSBN7 and MDPT, the two locations with high steering angles, show that although MUSIC performs better than beamforming, Beamscan outperforms both methods (see Fig. 9-11).

The beamforming radial current estimates at both MDPT and SSBN7 exhibit tidal variability that is similar to that found at ADCP1 during event C (Fig. 13) something unexpected given the relative position of the two stations in relation to the coastline. This is not the case for the MUSIC and Beamscan radial current estimates. As discussed in section 3.2.2, in contrast to beamforming, both Beamscan and MUSIC first separate the Doppler spectrum into separate frequency bins and subsequently try to identify the direction of arrival of each frequency. Separating the signal first by frequency, may suppress stronger signals at other frequencies more than beamforming as the latter relies solely on the beam pattern for suppression. The effective beam patterns at SSBN7 (Fig. 15c, d) have sidelobes which are not well suppressed when one of the antennas is not operational. Under such circumstances, a strong signal from a different location would not be sufficiently suppressed and could overwhelm the signal from SSBN7.

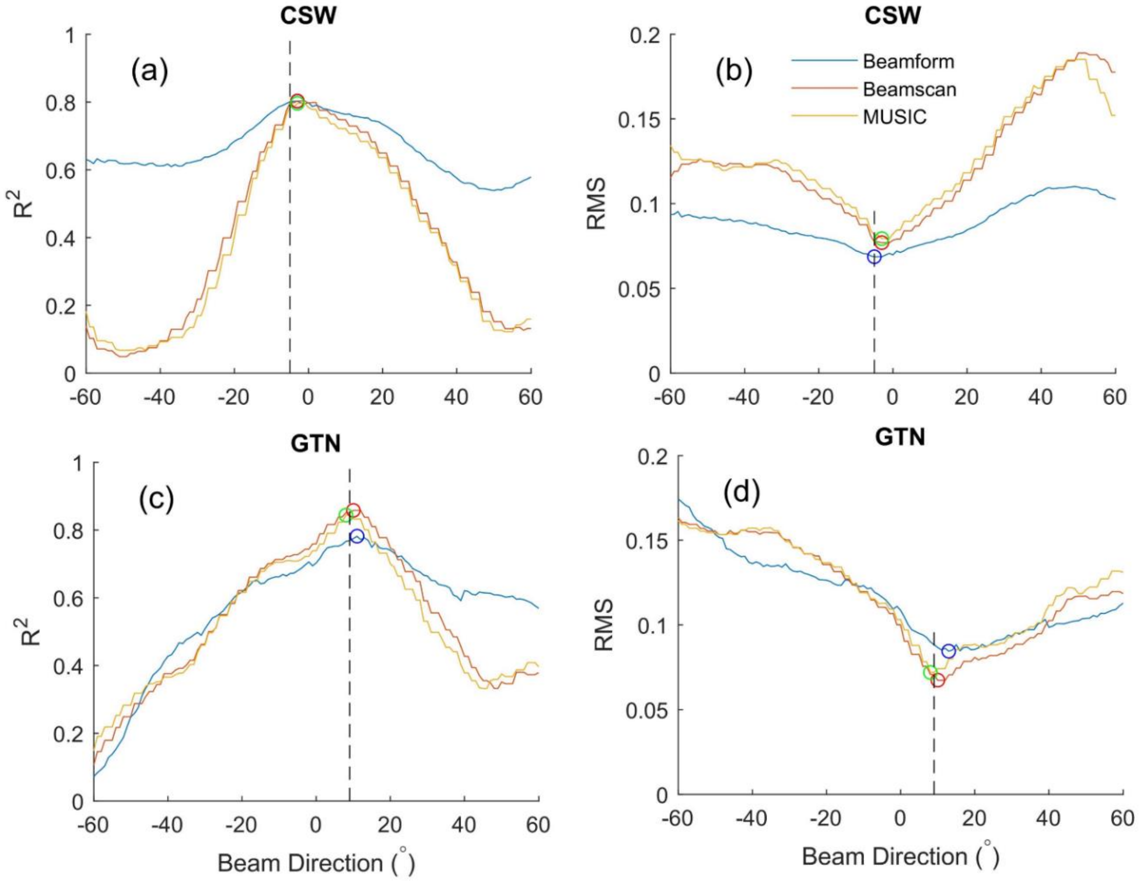

Figure 2.18: The correlation (R^2) and RMSD between HF radar radial current estimates and in situ radial currents at ADCP1 for different radial directions. The vertical dashed line indicated the true direction of the in situ location. Beamforming's (blue), Beamscan's (red) and MUSIC's (yellow) best correlations and minimum in RMSD is shown as circles.

Although the theoretical beam patterns presented in here are smooth, real antenna patterns are known to be noisier due to antenna geometry imperfections and local environmental conditions potentially reducing the effectiveness of sidelobe suppression. This would lead to the HF radar beamformed current estimates at SSBN7 to reflect ocean current values corresponding to a different patch of the ocean but of the same range. If this is the case, the tidal characteristics of the beamformed radial estimates at SSBN7 should match those at a different location of the ocean. This is further explored below. Additionally, it should be noted that MUSIC is known to be sensitive to imperfections in antenna patterns (Dumas and Guérin, 2020).

2.5.1.1 Tidal analysis

As noted earlier tidal flows in Long Bay, SC are dominated by semi-diurnal tides (Blanton et al, 2004; Gutierrez, 2006). Therefore, we use this tidal signal to identify the discrepancies observed in the current estimates. Harmonic analysis (Pawlowicz et al, 2002) was carried out on the in situ and radar derived radial velocities estimated using the different methods at the various stations using the full time-series available. The results for the dominant constituent (M2) are listed in Table 4 and suggest that at the offshore site (ADCP1, low steering angle) the in situ and radar methods are within 3 cm/s in amplitude and 12° in phase values (see Table 4). The tidal analysis for SSBN7 shows that the M2 characteristics derived from Beamscan and MUSIC are much closer to the in situ results than beamforming.

Table 2.4: Amplitude and phase of the M2 constituent estimated using the different radar radial velocity components at the different locations (ADCP1, SSBN7, and MDPT). $\Delta\theta$ is the result of the optimization method used to identify the source of the signal (see text for details).

Location	Radial Velocity	Radial Direction	Amp. (cm/s)	Phase (∘)	Δθ (∘)
ADCP1	in situ	CSW	12.7 ± 0.2	125.9 ± 1.1	5.4
		GTN	13.1 ± 0.3	55.4 ± 1.2	-3.6
	beamform	CSW	12.5 ± 0.2	121.9 ± 1.1	5.4
		GTN	16.1 ± 0.3	67.2 ± 1.2	-18
	Beamscan	CSW	12.2 ± 0.3	137.9 ± 1.2	-1.8
		GTN	15.2 ± 0.2	61.3 ± 1.1	-12.6
	MUSIC	CSW	12.4 ± 0.3	139.0 ± 1.3	-1.8
		GTN	14.8 ± 0.3	61.3 ± 1.1	-12.6
SSBN7	in situ	CSW	5.1 ± 0.3	280.5 ± 3.5	-1.8
		GTN	2.3 ± 0.3	101.5 ± 7.5	-1.8
	beamform	CSW	12.1 ± 0.6	112.9 ± 2.7	64.8
		GTN	11.9 ± 0.5	70.3 ± 2.4	-41.4
	Beamscan	CSW	3.8 ± 0.4	274.9 ± 5.5	0.0
		GTN	6.8 ± 0.4	86.7 ± 3.4	-1.8
	MUSIC	CSW	1.7 ± 0.4	273.3 ± 13.4	-1.8
		GTN	7.6 ± 0.4	84.6 ± 2.5	1.8
MDPT	beamform	CSW	10.4 ± 0.4	112.9 ± 1.9	37.8
		GTN	10.4 ± 0.7	250.1 ± 3.9	14.4
	Beamscan	CSW	4.7 ± 0.3	233.4 ± 3.1	-3.6
		GTN	4.8 ± 0.4	233.6 ± 4.8	-16.2
	MUSIC	CSW	4.8 ± 0.4	240.0 ± 3.6	-5.4
		GTN	4.3 ± 0.5	245.5 ± 6.8	14.4

2.5.1.2 Source (azimuth) of the backscattered signal

To estimate the origin (azimuth) of the backscattered signal that leads to the radar derived radial currents (and therefore the radar derived M2) at each station, an optimization method is utilized. The assumption is that the source of the signal is located at the same range as the intended station, but at a different azimuth. The optimization method identifies an azimuth on this range ring where the HF radar derived M2 amplitude and phase (Table 4) match modelled barotropic tides at this location [available at https://adcirc.org/products/adcirc-tidal-databases/, see Blanton et al. (2007) and Szpilka et al. (2016) for details]. The minimization process includes both normalized velocity and phase errors $E(\theta)$ and it is defined as the difference (RMSD) between the radar estimated tidal harmonic and the modelled tidal harmonic projected onto the radar radial over one tidal cycle:

$$E(\theta) = \frac{1}{2\pi}\int_0^{2\pi}\{v_{HF}\sin(t+\phi_{HF}) - v_{DB}(\theta)\sin[t+\phi_{DB}(\theta)]\}^2\,dt, \qquad (2.14)$$

where $v_{HF}(0)$, $\phi_{HF}(0)$ and $v_{DB}(\theta), \phi_{DBm}(\theta)$ are the M2 amplitude and phase, from the HF radar and tidal database, respectively; θ is the radial angle with $\theta = 0$ defined as the direction of the HF radar towards the location the optimization method is applied (e.g., ADCP1). t in (14) denotes tidal phase within the M2 tidal cycle. The value $\Delta\theta$ where the function $E(\theta)$ in minimized is assumed to represent the azimuth that the signal comes from, and it represents the difference in direction between the intended beam direction and the location the tidal analysis from the HF radar measurement that most closely matches the model.

Application of the optimization method to the offshore site ADCP1 is shown in Fig. 19a where the range rings for that site corresponding to CSW and GTN radar systems are shown as dotted black lines. The $\Delta\theta$ values for the HF radar derived M2 radial amplitudes/phases are listed in Table 4 and shown on the ADCP1 range rings in Fig. 19. At ADCP1, $\Delta\theta$ for CSW, when compared to the modelled tides are low ($\Delta\theta \leq 5.4°$ for all three methods), which agrees with the comparison of the in situ measurements and the modelled tides ($\Delta\theta = 5.4°$). For GTN, in situ azimuth error ($\Delta\theta = -3.6°$) differ by less than $15°$ to the radar results, beamforming ($\Delta\theta = -18°$), Beamscan ($\Delta\theta = -12.6°$) and MUSIC ($\Delta\theta = -12.6°$). In Fig. 19a, the differences to the model ($\Delta\theta$) are plotted and the in situ measurements and all three radar methods closely agree for CSW. At GTN, the differences between the radar and in situ data are equal to roughly half the beamwidth ($15°$) and therefore within expected accuracy. Therefore, HF radar measurements at ADCP1 fall within the expected azimuth accuracy.

Similar analysis was carried for the nearshore station SSBN7 and the location MDPT along the baseline. The error in azimuth ($\Delta\theta$) at these two locations are shown in Table 4 and are plotted along the range rings in Fig. 19b, c. At SSBN7 (Fig. 19c) the in situ, Beamscan and MUSIC errors in azimuth are within $2°$ of the modeled tides. However, the beamforming errors in azimuth are over $40°$ for both CSW and GTN. As seen in Fig. 19c, the actual directions the beamformed and MUSIC tidal signals come from are closer to the radar boresight than the intended beam direction.

At MDPT (Fig. 19b), the errors in azimuth are below $20°$ for Beamscan and MUSIC while beamforming has an error of $37.8°$ for CSW. Although the errors in azimuth are similar for beamforming at GTN, the difference in tidal amplitude is large; close to the in situ tidal amplitude at ADCP1.

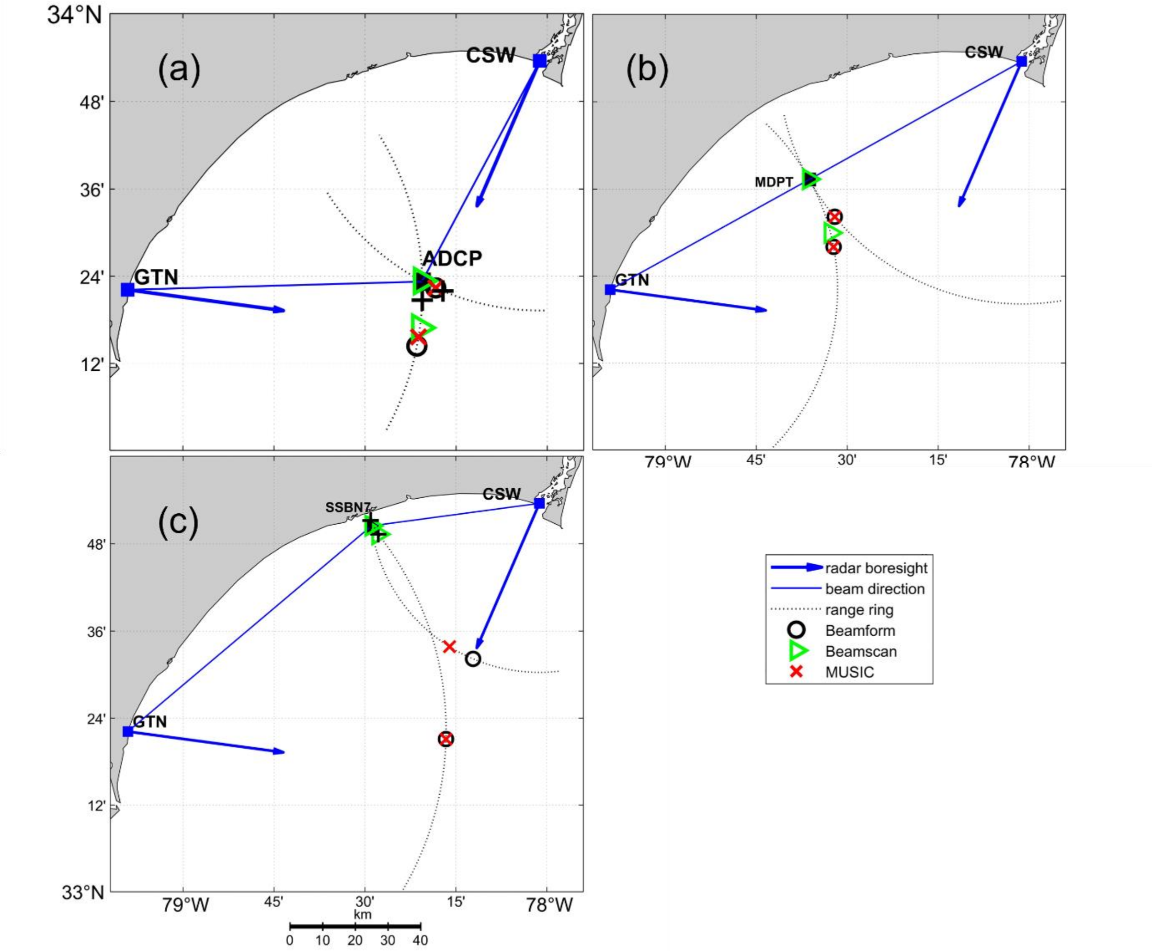

Figure 2.19: Results of the minimization analysis (see text for details) performed to the tidal M2 signal recorded on sites (a) ADCP1, (b) MDPT, and (c) SSBN7. In each panel black '+' is used to mark the location along the range circle where the in situ radial amplitude and phase match those of the model. Locations where beamforming (circles), Beamscan (green triangle) and MUSIC (red 'x' symbols) derived radial current solutions match those of the tidal model. The radar boresight and beam direction are shown with blue arrows and blue lines, respectively.

$\Delta\theta$ suggests that the beamformed error in direction ranges from $0°$ to $64.8°$ in this study. This error in direction is greater than half the beamwidth and is most likely due to sidelobe contamination as can be expected from our previous considerations of the beam pattern and HF radar forward modeling (Fig. 16-17). This large bias in direction is unwanted but does explain why we see such large tidal modulation in the beamformed currents (Fig. 13c-e).

2.6 Summary and conclusions

Whilst numerous studies have focused on evaluating the performance of HF radar systems with in situ data, most have concentrated on establishing the accuracy of the radars. In this study we examined the potential reasons a HF radar system might not perform as expected and we identified alternative methods to analyze the signal as to improve performance. We compared HF radar surface currents to in situ measured currents from two linear HF radar arrays under normal operational conditions and at large steering angles, with and without malfunctioning antennas. HF radar surface currents were estimated using beamforming (the standard method for linear arrays) and two direction finding methods: the commonly used algorithm, MUSIC, and Beamscan. Our results indicate that all three HF radar methods perform well at low azimuth angles (i.e., close to the radar boresight). This location is representative of how beamforming performs when the beampattern suppresses sidelobes well.

However, at locations far from the radar boresight (steering angle $> 35°$) beamforming was found to be a poor performer for our system (RMSD and NRMSD of roughly 14-16 cm/s and 1.5, respectively); Beamscan and MUSIC show better correlation with in situ data at location SSBN7 corresponding to a large steering angle. For Beamscan and MUSIC, RMSD values are 9-13 cm/s. At the baseline midpoint (steering angle of $38°$), the two radars correlate to each other significantly better using Beamscan ($R^2 = 0.76$, RMSD = 6.4 cm/s) than either beamforming ($R^2 = 0.01$, RMSD = 14 cm/s) or MUSIC ($R^2 = 0.49$, RMSD = 10 cm/s), although MUSIC still performs much better than beamforming.

Notably, when all antennas are functioning well (site GTN for events A and B) beamforming performed similarly to Beamscan during event A at both locations (SSBN7 and MDPT), however, wave height was higher at SSBN7 than near the GTN boresight (ADCP1) during this time. During event B, which better represents climatological averages where wave height is lower nearshore (SSBN7) than offshore (ADCP1), Beamscan performed better than beamforming even though all antennas were functioning well for site GTN. During the other events and for site CSW, not all antennas were functioning correctly, which caused a significant degradation in the beam pattern. For these situations, Beamscan performed significantly better than beamforming. Although these antennas can be fixed, an 8 antenna linear array always has lower sidelobe suppression and therefore Beamscan may offer better performance than beamforming at large steering angles on these systems.

Besides the known degradation of the beam pattern at large angles from the boresight, the additional effects of the transmit pattern significantly effect beamforming in our modelled results, especially with low SNR. The transmit pattern will vary with other TX array configurations and we suggest future research incorporates TX array characteristics (including measuring the transmit beam pattern) in HF radar modelling. As in the modelled results, the HF radar measurements near the coast (SSBN7 and MDPT), resulted in beamformed currents with low accuracy when wave height was significantly higher offshore (in the direction of the radar boresights). Under such conditions comparing the results with those obtained using a direction finding method might be beneficial as the latter method would provide data that is in disagreement to the beamforming data. This could be recorded as a flag alerting the operator that these locations may be problematic.

At SSBN7 and MDPT, where wave energy is low and the beam pattern is poor, the direction finding methods' results are noisy, while the beamformed current estimates have tidal modulation resembling the beamformed measurements closer to the radar boresight. Tidal analysis of the HF radar radials currents confirms these expectations. The beamformed HF radar measurements do not agree with in situ measurements at the high steering angles (SSBN7) but instead agree with the modeled tides from an offshore location much closer to the radar boresight. In a worst-case scenario, the pointing error in beamforming was over 60° (see Table 4). The random errors in Beamscan do not affect tidal analysis, and HF radar derived tidal M2 constituents closely matches the in situ derived results and the modeled tides at this high steering angle location.

The Beamscan direction finding method used here could be easily applied to beamforming HF radar systems operationally as it does not require extensive tuning and more easily adaptable for longer term operations where antenna characteristics tend to deteriorate over time. Disagreements between the two solutions can used identify possible issues in beamforming at particular locations in the HF radar coverage area. The Beamscan direction finding along with the beamforming and MUSIC MATLAB codes used here are available in Cahl and Voulgaris (2022), while codes for reading WERA raw data are available in Voulgaris and Cahl (2020).

CHAPTER 3

ON THE FRACTION OF STOKES DRIFT INCLUDED IN OCEAN WAVE PHASE SPEED, MEASURED BY HF RADARS[2]

---

[2] This Chapter has been submitted as Cahl D, Voulgaris G, Wu X (2023) On the Fraction of Stokes Drift Included in Ocean Wave Phase Speed, Measured by HF Radars. Ocean Dynamics ODYN-D-23-00025, submitted 3/7/2023.

Abstract

HF radars' surface current estimates are based on the ability of these systems to accurately measure the phase speed of wind driven ocean waves. The latter is thought to be modified by the Stokes drift which in turn affects the accuracy of the Eulerian current estimate provided by the HF radar systems. Efforts to quantify this have led to the development of three approaches that describe the fraction of the Stokes drift contributing to wave phase speed modification: a nonlinear weighted and depth averaged Stokes drift (effective Stokes drift), the Stokes drift mostly from longer waves than the wave in question (filtered Stokes drift), and half the surface Stokes drift. The first two quantities are dependent on the wavelength of the ocean wave, where long waves are barely affected, and short waves are affected by the majority of the surface Stokes drift.

A 7-month data set from two 12-antenna beamforming linear array HF radars are compared to in-situ Eulerian current measurements. Modelled wave spectra are used to assess the three proposed Stokes drift contributions. Filtered Stokes drift shows the best correlation to the difference between the radar and in-situ current measurements and it could be used to correct HF radar derived surface velocities. With that in mind, a neural network method is developed that uses the amplitude of the Bragg peaks from two radar systems to predict the filtered Stokes drift terms. The filtered Stokes drift prediction correlates to the difference between the radar and in situ measurements with $R^2 > 0.6$.

3.1 Introduction

Recently, remote sensing techniques that estimate ocean surface currents by measuring the phase speed of ocean waves have increased in popularity. The surface current is estimated as the difference between the theoretical still-water phase speed of an ocean wave and the measured phase speed. This method of estimating surface currents is performed using HF Doppler radars (Paduan and Washburn, 2013, and Rubio et al. 2017), marine X-band radars (Huang et al. 2017), proposed satellite radars (Ardhuin et al. 2019) and video imagery from high resolution cameras mounted on airplanes (Dugan et al. 2001), fixed platforms (Middour et al. 2023) and small quadcopters (Streßer et al. 2017).

HF radars are the most mature technology in widespread use that estimate ocean currents by measuring the phase speed of ocean waves and there has been a plethora of research on the accuracy of HF radar derived surface current measurements (see Paduan and Washburn, 2013 and references within). Although Stokes drift is often 1-2 orders of magnitude less than the phase speed of wind-driven waves, HF radar technology and data processing techniques have matured to the point where this small effect is within the accuracy of HF radar measurements.

HF radar's transmitted signal is scattered from ocean waves with a wavelength equal to half the radar wavelength (Crombie, 1955), which are known as Bragg waves. The Doppler shift of the return signal has been shown to be a measurement of the phase speed of these ocean Bragg waves (Barrick, 1972). The deviation from the theoretical phase speed in still-water is used to estimate the surface ocean current. Since the early research into using HF radars to estimate surface currents, there has been the need to assess the effects of vertical current shear (Stewart and Joy, 1974) and wave-wave interactions (Barrick, 1979) on the phase speed of these ocean Bragg waves to determine what exactly the surface current estimate is. Although Stewart and Joy's (1974) vertical current shear solution is widely accepted (e.g., Paduan and Washburn, 2013), wave-wave interactions are still debated (Chavanne 2018).

The most well-known solution comes from Stokes (Stokes, 1847), known as the Stokes wave. In addition to giving rise to Stokes drift, a Stokes wave in the finite amplitude approximation also increases its own phase speed by half the surface Stokes drift that it produces. This suggests that the phase speed of a wave on the ocean surface is modulated by half the total surface Stokes drift, which has shown to be consistent with HF radar measurements by Dussol et al. (2022).

However, it seems unlikely that the Stokes drift of very short waves can modify the phase speed of longer swell waves with larger wavelengths, where the orbital velocities extend many meters below the surface. This argument is confirmed with theoretical approximations using both non-directional (Longuet-Higgins and Phillips, 1962) and fully directional wave spectra (Weber and Barrick, 1977). These approximations suggest that only Stokes drift from waves with longer wavelengths than the wave in question contribute to its phase speed (referred to as ‘filtered Stokes drift’ in Adrhuin et al. 2009). This implies that the shorter waves would “feel” the Stokes drift from the longer waves, but not vice versa.

A different approach considers the solution to the modulation of wave speed due to Eulerian currents (Stewart and Joy, 1974). In this case the phase speed of a wave is modulated by the vertical current profile weighted by the same vertical (with depth) exponential weighting as Stokes drift. Assuming a linear vertical shear profile, the additional phase velocity of the wave is equal to the Eulerian velocity at a depth of $\lambda/4\pi$, called the ‘effective depth’ of the Bragg wave. For more sheared profiles, such as Stokes drift, the effective depth is shallower (Chavanne et al. 2018). We refer to this contribution term as ‘effective Stokes’, which has shown to correlate to the difference between in-situ and HF radar current estimates (Laws, 2001; Ullman et al. 2006).

While half surface Stokes drift is the same for all wavelengths, both filtered Stokes and effective Stokes go close to zero for long wavelengths and close to the full surface Stokes drift for short wavelengths. For more insight into these terms, synthetic JONSWAP spectra (Hasselmann et al. 1973) for wind speeds of 5, 10, 15 and 20 m s^{-1} were created (see figure 1a) and converted to directional spectra using the method in Kumar et al. (2017) assuming a spreading parameter of 20° (see example in figure 1b). These synthetic directional wave spectra were used to calculate the different Stokes contribution terms for wavelengths ranging from 1 km to 10 cm, and the results are shown in terms of velocity (in m s^{-1}) and percent of the total surface Stokes drift in figures 1c and 1d, respectively.

The absolute values of the contribution terms (figure 1c) show a difference between the effective Stokes term (dashed lines) and the filtered Stokes terms (solid lines) for all wind speeds. At 5 m/s wind speed (blue lines) the difference between the terms for a 10 meters wavelength wave is close to 1 cm/s while at 20 m/s wind speed (magenta lines) the difference is close to 5 cm/s. When comparing these two terms to the total surface Stokes drift (figure 1d), there is no overlap between the two. For all wind speeds, wavelengths longer than 100 meters have an effective Stokes term close to 0% (dashed lines in figure 1d) while filtered Stokes is 10 – 20% of the full surface Stokes drift (solid lines in figure 1d). For waves shorter than 10 meters, filtered Stokes is close to the full surface Stokes drift while effective Stokes only approaches full surface Stokes drift for very short waves. Half surface Stokes is marked by the solid black line in figure 1d, signifying the same increase in phase velocity for all wavelength waves.

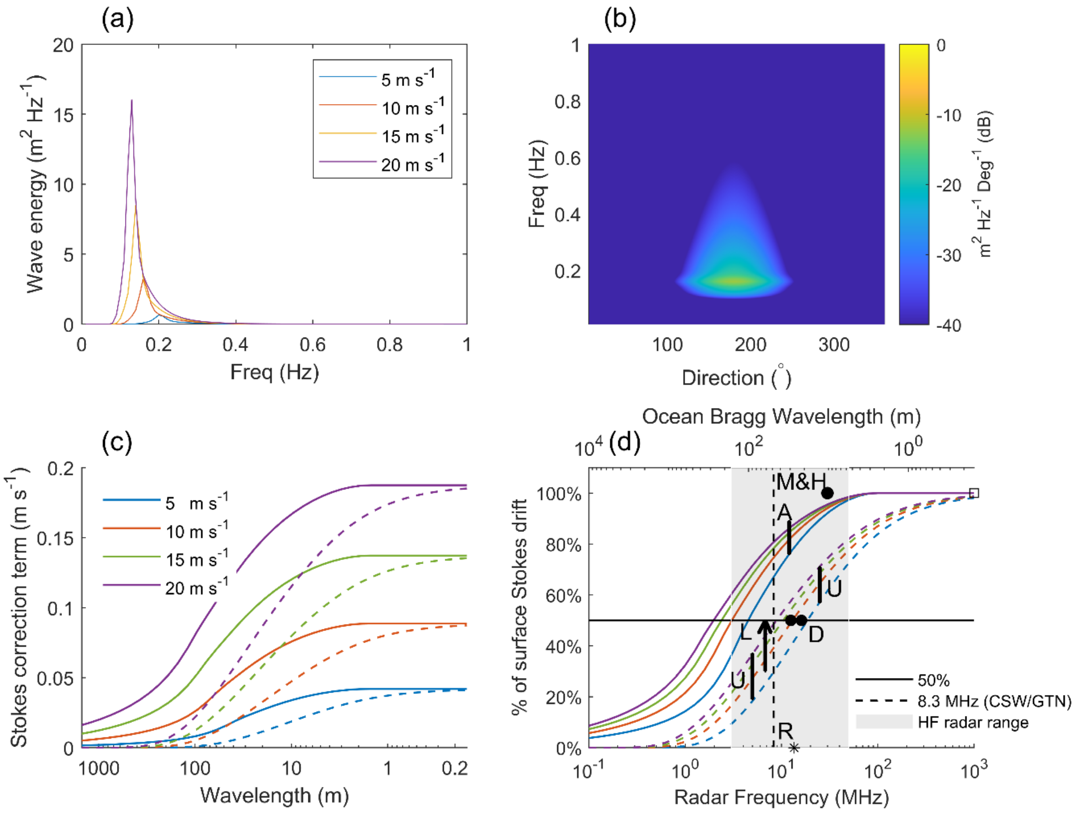

Figure 3.1: (a) JONSWAP spectrum for four wind speeds, 5, 10, 15 and 20 m/s. (b) Directional wave spectrum with a spreading parameter of 20° for a wind speed of 10 m/s in. (c) Filtered (solid lines) and effective (dashed lines) Stokes drift contribution terms (in velocity) calculated from the JONSWAP wave spectra in (a). (d) Same contribution terms as in (c) shown as percentage of the surface Stokes drift. Horizontal solid line in (d) indicates half surface Stokes drift. In (d), shaded area delineates HF radar common operating frequencies; Stokes drift contributions to HF radar measurements from previous studies are also shown: **R**: Rohrs et al (2015), **U**: Ullman et al. (2006), **M&H**: Mao and Heron (2008), **D**: Dussol et al. (2022), **L**: Laws et al. (2008), **A**: Ardhuin et al. (2009)

Additionally, in figure 1d, the range of HF/VHF radar operating frequencies (3-50 MHz) and corresponding Bragg wavelengths are shaded in gray. Although previous research has been inconsistent in identifying which Stokes drift contribution is applicable to HF radars, figure 1d suggests that effective and filtered Stokes terms provide the greatest variability. Rohrs et al. (2015) found no Stokes drift contribution (see R in figure 1d) but noted that the uncertainty in the HF radar measurements were larger than the potential contribution terms (marked with a star in figure 1d). Mao and Heron (2008) suggested the full surface Stokes drift was included but at their operating frequency (30 MHz) a large fraction of Stokes drift is included in filtered Stokes drift already, so distinction between these two terms is not possible. Laws et al. (2001) found a good correlation between effective Stokes drift and the difference between in situ and HF radar measurements (at 6.8 MHz), however the fitted slope was much greater than 1; this suggests that a larger percent of Stokes drift was present in the HF radar measurements (see upward arrow in figure 1d). Ardhuin et al. (2009), using a 12 MHz radar, argued that filtered Stokes provides the appropriate contribution while Ullman et al. (2006) found effective Stokes drift to be correct at both 5 and 25 MHz. Dussol et al. (2022), using 12.5-16 MHz radars, found half surface Stokes drift to best fit their data but at their operating frequencies half surface and effective Stokes drift contributions are very fall very close to each other (figure 1d). Despite the lack of clear agreement, the aforementioned studies seem to suggest that there is a Stokes drift contribution that is included in the HF radar measurements that merits further investigation.

Using the HF radar, the most direct path to estimate the Stokes contribution terms is to estimate the wave spectrum through wave inversion of the HF radar signal (e.g., Wyatt et al. 2006, Essen et al. 1999; Al-Attabi et al. 2019). However, this is not feasible at long ranges, where signal attenuation and increased noise levels make wave inversion inapplicable (Paduan and Washburn, 2013). On the other hand, wind inversion methods use the first order radar signal from multiple HF radar sites have been developed (i.e., Shen et al, 2012, Kirincich et al. 2016) that can provide wind speed and direction estimates at all ranges surface currents are provided. The premise is that these wind speed and direction estimates can be used to calculate the Stokes contribution terms corresponding to these wind conditions. Although this is possible, wind inversion from HF radars has limited accuracy ($R^2 \approx 0.5$, Shen et al. 2012) and the sea state is likely not well approximated by a JONSWAP spectrum since wind variation can be significant and the waves are not always in equilibrium with the prevailing winds. Therefore, motivated by the fact that neural networks have been capable of estimating wind speed from the first order radar signal (i.e., Shen et al. 2012) and wave spectra from the second order spectra (i.e., Hardman and Wyatt, 2019), in this study we investigate the ability of neural networks to directly estimate the Stokes contribution terms from the first order radar signal.

The primary goal of this paper is to evaluate the different Stokes drift contribution terms and identify the most appropriate one to be used operationally. A secondary goal is to increase the accuracy of HF radar derived surface current estimates by developing a method that uses the radar signal itself to estimate the appropriate contribution term. If successful, HF radar estimates can be corrected to represent either truly Eulerian or Lagrangian velocities. In this study we focus on providing Eulerian currents that agree with the in situ measurements from an ADCP.

In section 2 we present a description of the various Stokes drift contribution terms: effective, filtered, and half surface Stokes. The data and methods of analysis carried out are described in section 3 while the results are presented in section 4. This is followed by a discussion of the neural network inversion in section 5 and the conclusions are presented in section 6.

3.2 Phase speed of ocean waves and Stokes drift

In addition to wavelength and depth (h) dependence of the phase speed of ocean gravity waves, there are well-known wave-current interactions (Stewart and Joy, 1974) and likely wave-wave interactions (Chavanne et al. 2018) that should be considered. Wave-current interactions are dependent on the Eulerian currents $[u(z)]$ in the direction of wave propagation, while wave-wave interactions (the Stokes contribution terms introduced in section 1) are due to the directional wave spectrum $[S_{\eta\eta}(f,\theta)]$ and are also dependent on the wavelength of the wave (see figure 1). Therefore, the observed wave phase speed (c) includes contributions from both Eulerian velocity, $c_E[k,u(z)]$ and wave-wave interactions, $\Delta c_{St}[k,S_{\eta\eta}(f,\theta)]$ so that:

$$c\left[k,h,u(z),S_{\eta\eta}\right] = c_0(k,h) + c_E[k,u(z)] + \Delta c_{St}\left(k,S_{\eta\eta}\right) \qquad (3.1)$$

where c_o is the linear phase speed, $c_0 = \sqrt{\frac{g}{k}\tanh kh}$ and k is the wavenumber. The third term in equation (1) is the wave-wave interaction term $\left[\Delta c_{St}\left(S_{\eta\eta}\right)\right]$; it could be either filtered Stokes $\left[\Delta c_F\left(S_{\eta\eta}\right)\right]$, effective Stokes $\left[\Delta c_E\left(S_{\eta\eta}\right)\right]$, or half surface Stokes $\left[\Delta c_H\left(S_{\eta\eta}\right)\right]$.

Stokes drift (Stokes 1847) is the time averaged velocity water particles experience due to the orbital velocities induced by surface gravity waves. Stokes drift from each wave is proportional to its amplitude squared and exponentially weighted by twice its wavenumber (k) times depth. Given a surface gravity wave spectrum $[S_{\eta\eta}(\omega,\theta)]$ the Stokes drift $[u_s(z)]$ at a depth z is given by the sum of the Stokes drift from all gravity waves (Kenyon, 1969). Usually, we assume some high frequency cutoff (ω_c) due to wave breaking, so that:

$$u_S(z) = \int_0^{\omega_c} \int_{\theta=0}^{\theta=2\pi} \omega\, k S_{\eta\eta}(\omega, \theta) e^{2kz}\ d\theta\ d\omega, \tag{3.2}$$

where ω is the wave frequency and θ is wave direction.

In the sections below a brief background and theoretical description of the wave conditions and processes affecting the three terms on the RH side of equation (1) is presented.

3.2.1 Linear Wave Phase Speed

The surface gravity wave dispersion (Airy, 1841) relationship ($\omega^2 = gk \tanh kh$) relates the wave frequency (ω) to wavelength ($\lambda, k = 2\pi/\lambda$) and is dependent on water depth (h). This ignores surface tension and the shortest wavelength valid in the ocean is roughly 5 cm (Falcon and Mordant, 2022). The phase speed (c_0) of Airy waves is only dependent on wavelength and water depth,

$$c_0(k, h) = \sqrt{(g/k) \tanh kh}\,. \tag{3.3}$$

This assumes a small amplitude approximation and no vertical current shear, no other waves (i.e., no wave-current, wave-wave, or self-interaction). Therefore, there using the Airy wave solution, one must assume the entire water column is moving at a constant speed (u) and therefore the phase speed of an ocean wave (c) is simply the still-water phase speed (c_0) plus the speed of the water column. However, the water column has significant vertical shear near the surface (Laxague et al. 2018). Therefore, a search for analytic solutions to ocean surface gravity waves in a vertically sheared current is necessary to know what depth the HF radar measurements correspond to as this defines the wave-current interaction effects, discussed next.

3.2.2 Wave-current Interaction Effects

The vertical current shear from Eulerian flows affects the second term in equation (1), $c_E[k, u(z)]$; Stewart and Joy (1974) presented a solution based on the assumption that the surface current is much smaller than the phase speed of the wave in still water $[u(z = 0) \ll c(k, h)]$. In this case the phase speed of a particular wave, is influenced by the vertical current profile $[u(z)]$, in the direction of wave propagation, weighted by the waves' Stokes drift profile (e^{2kz}):

$$c_E = 2k \int_{-\infty}^{0} u\,(z) e^{2kz}, \tag{3.4}$$

where c_E is change in phase speed due to the current. The depth at which, the horizontal current $[u(\mathrm{z})]$ is equal to c_E is referred to as the effective depth (z_{ef}) and assuming linear vertical current shear $[u(z) = mz]$ it can easily be shown that $z_{ef} = \lambda/4\pi$. Even for an exponential vertical current shear $[u(z) = ae^{mz}]$, the effective depth is well approximated by $z_{ef} = \lambda/4\pi$ if $m \ll k$ (Stewart and Joy, 1974), i.e., the vertical current shear occurs over a larger depth than the e-folding scale of the wave (k).

This implies that the HF radar measurements of wave phase speed include the effect of the current at the effective depth of the corresponding Bragg wave. This effective depth depends on both the wavelength of the wave and vertical current shear but it is common to use the approximation $z_{ef} = \lambda/4\pi$. This wavelength dependent effect of vertical current shear on the phase speed of waves has been validated (Fernandez et al. 1996; Shrira et al. 2001; Sentchev et al. 2017) using data from both HF and x-band radars (Lund et al. 2015).

3.2.3 Wave-wave Interaction Effects

Perhaps the most well-known wave-wave interaction is the self-interaction of a finite amplitude wave (Stokes, 1847), which results in an increase in the phase speed as compared to Airy waves (2):

$$c_{st47} = \sqrt{\frac{g}{k}(1 + k^2a^2)}. \tag{3.5}$$

where a is the amplitude of the wave. In a small amplitude approximation $(k^2a^2 \ll 1)$, the departure of Stokes phase speed (c_{st47}) from Airy wave phase speed (c_0) is equal to half of the surface Stokes drift. This is quite small, as the Stokes drift is only from a single wavelength. Chavanne et al. (2018) remarks that for a HF radar operating at 13.5 MHz (11m Bragg wavelength), this increase in phase speed is typically around 3 cm/s, which is smaller than the typical HF radar accuracy (5-20 cm/s, i.e., Essen et al. 2000; Guérin et al. 2021).

3.2.3.1 Effective Stokes

Effective Stokes utilizes the Stokes drift velocity (2) in Stewart and Joy’s (1974) solution for Eulerian sheared currents (4). HF radar surface current estimates can therefore be thought of as Lagrangian current measurements at the effective depth of the Bragg wave, this solution is therefore called ‘effective’ Stokes. However, since Stokes drift has high shear near the surface, the effective depth of the Bragg wave due to Stokes drift will be shallower than the effective depth due to linear vertical shear from Eulerian currents.

Laws (2001) solution for a 1D wave spectrum of waves propagating in the direction of the Bragg wave is what is known as the ‘effective Stokes drift’:

$$\Delta c_E = 2k_B \int_0^{\infty} \omega \frac{k}{k+k_B} S(k) dk. \tag{3.6}$$

where k_B is the wavelength of the Bragg wave corresponding to the HF radar operating frequency. Although this approach may seem logical, Teague (1986) has argued that there is no validity in using the Lagrangian mean flow in Stewart and Joy’s (1974) solution.

3.2.3.2 Filtered Stokes

Instead of using a Eulerian solution for Lagrangian flows (effective Stokes), Longuet-Higgins and Phillips (1962) produce a different result for a 1D wave spectrum,

$$\Delta c_{L62} = 2 \int_0^{k_B} \omega\,(k) k S(k) dk + 2k_B \int_{k_B}^{\infty} \omega\,(k) S(k) dk. \tag{3.7}$$

Barrick and Weber (1977) extended this analysis to a fully directional wave spectrum. In their solution the filtered Stokes velocity is approximated (Broche et al. 1983) by the surface Stokes drift from waves longer than the wave in question (Bragg wave, k_B) and a smaller nonlinear term from higher frequency waves. Following Ardhuin et al. (2009), the approximation for ‘filtered Stokes drift’ is given by,

$$\Delta c_F = \vec{u}_{ss}\,(f_B) \cdot \vec{e}_{\theta_B} + \int_{f_B}^{\infty} \int_0^{2\pi} f \cos(\theta - \theta_B) S(f, \theta)\, d\theta\, df, \tag{3.8}$$

where $\vec{e}_{\theta_B}$ is a unit vector in the direction of propagation of the Bragg wave. The first term, $\left[\vec{u}_{ss}\,(f_B) \cdot \vec{e}_{\theta_B}\right]$, is equal to the surface Stokes drift from all waves longer than the Bragg wave [(2) with an upper frequency limit $w_c = f_B$], which means that waves "feel" the Stokes drift from other waves that are longer than them $(f < f_B)$. Shorter waves do play a role, but for HF radar operating frequencies the second nonlinear term that depends on the full directional wave spectrum is usually much smaller than the first term (Ardhuin et al. 2009). Therefore, the filtered Stokes term is well approximated by the surface Stokes drift up to the Bragg wave frequency of the HF radar.

3.2.3.3 Half Surface Stokes

Huang and Tung (1976) extended Longuet-Higgins and Phillips (1962) approximated solution for a continuous wave spectrum. Their analysis suggested that every wave has the same phase speed contribution, half the total surface Stokes drift (u_{ss}),

$$\Delta c_H = \int_0^\infty \omega\,(k)\; k\; S(k)\; dk = \frac{1}{2} u_s(0) = \frac{1}{2} u_{ss}. \tag{3.9}$$

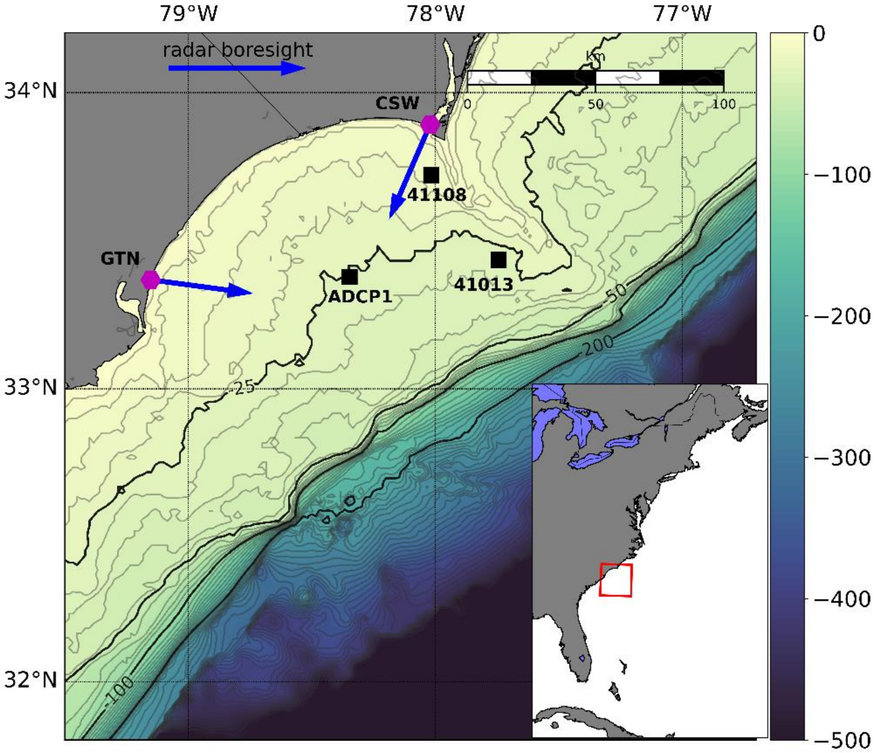

Figure 3.2: Study site location. HF radar sites GTN and CSW and their boresight direction are shown as magenta hexagons and blue arrows, respectively. The locations of in situ current data from a bottom mounted ADCP (ADCP1), wind data (NDBC Buoy 41013), and wave data (NDBC Buoy 41108) are also shown

3.3 Data Availability

3.3.1 Study Site

In this study, data from two HF radars, in-situ currents from an ADCP and wind and wave data all collected off the SE USA coastline in Long Bay SC are used.

Long Bay extends ~100 km off the coasts of South and North Carolina. The location of the ADCP deployment (ADCP1) is in the middle shelf, where the tides account for 30-45% of the total current variance (Gutierrez, 2006). The shelf circulation is also influenced by the passage of low-pressure synoptic fronts and local winds (Wu et al. 2017) which, on average, are stronger offshore than near the coastline (Wu et al. 2018). This results in average wave heights offshore being larger than wave heights nearshore (Cahl et al. 2022). The predominant directions of the winds during the passage of the fronts are from the northeast or southwest (roughly alongshore) and results in highly energetic wave events (Voulgaris et al. 2008). During the data collection period (July 1, 2016 – Feb 1, 2017) the passage of two Hurricanes brought strong winds and higher than average wave heights which created periods of significant Stokes drift.

3.3.2 Ocean Wave Phase Speed: HF Radar

HF radar surface current estimates were recorded from two beamforming HF radar systems located near Georgetown, SC (GTN) and at Fort Caswell, NC (CSW) overlooking Long Bay (SC). The HF radar systems used were 12 antenna beamforming linear array WEllen RAdars (WERA) systems manufactured by Helzel Messtechnik Gmbh (see Gurgel et al. 1999). The radars' operating frequency of 8.3 MHz corresponds to measurements of the phase speed of Bragg waves with a wavelength of ~18 m corresponding to an effective depth of ~1.4 m. Their boresights were pointed 9.4° and -4.9°away from the in situ current location (ADCP1) for GTN and CSW, respectively. The distance from GTN and CSW to the ADCP1 site is 75.2 and 63.5 km, respectively. Further details of the HF radar systems (GTN and CSW) and the beamforming surface current algorithm used can be found in Cahl et al. (2023) and the code in Cahl and Voulgaris (2022).

The HF radar velocity estimates represent 15 minute averages from quality controlled Doppler spectra with a Bragg peak with a minimum 25 dB signal-to-noise ratio. As in Cahl et al. (2023), a wild point editing method with a 5-point median sort filter (Justusson, 1981) was used to remove outliers.

3.3.3 In-situ Eulerian Currents: ADCP

A bottom mounted ADCP operating at 600 kHz was deployed in 25 m of water depth ($Site\ ADCP1, 78.347°\ \mathrm{W}, 33.379°\ \mathrm{N}$) and collected current data with a vertical resolution of 1 m. The upper usable bin was around 3.1 m below the mean sea surface and varied as function of sea state and tidal stage. Currents were recorded every hour and each record was the average of a 14 min ensemble.

A single acquisition of the ADCP measurements is shown in figure 3, the water depth is 25 meters, and the deepest measurement is 20 meters below the sea surface. The closest to the sea surface ADCP measurement is at 3.9 m (figure 3) which is below the HF radar effective depth (1.4 m) of the Bragg wave. Although the vertical current shear so close to the sea surface is not well understood (e.g., Mheen, 2020), Richman et al. (1987) and Churchill and Csanady (1983) have showed that current shear near the sea surface has a logarithmic distribution with distance (z) below the sea surface so that , $u(z) = u_* \kappa^{-1} \ln(z/r) + const$, where u_* is the wind stress, κ the von Karman constant and r is an empirical roughness parameter. However, wave breaking during high winds and/or high seas is known to increase near surface turbulence (Gemmrich and Farmer, 2004) and reduce the vertical shear predicted by the logarithmic model (Kudryavtsev et al. 2008). Furthermore, recent measurements have shown close to linear vertical shear in the top few meters (Laxague et al. 2018).

Therefore, to estimate the Eulerian current at the effective depth of the Bragg wave, a logarithmic model was fitted to the upper 5 ADCP measured velocities (green line in figure 3), additionally, a linear extrapolation was also made (black line in figure 3). The logarithmic extrapolation had worse correlation to the HF radar measurements than the uppermost ADCP measurement, while the linear extrapolation had slightly better correlation than the uppermost ADCP measurement. Therefore, we will use the linear extrapolation to the effective depth of the HF radar (1.4 m, black circles in figure 3) instead of the uppermost ADCP measurement for comparison to the HF radar measurements. We note here that rotation with depth is not included in our extrapolation as we expect little rotation between the topmost ADCP measurement and the effective depth of the HF radar (a difference of roughly 2 meters).

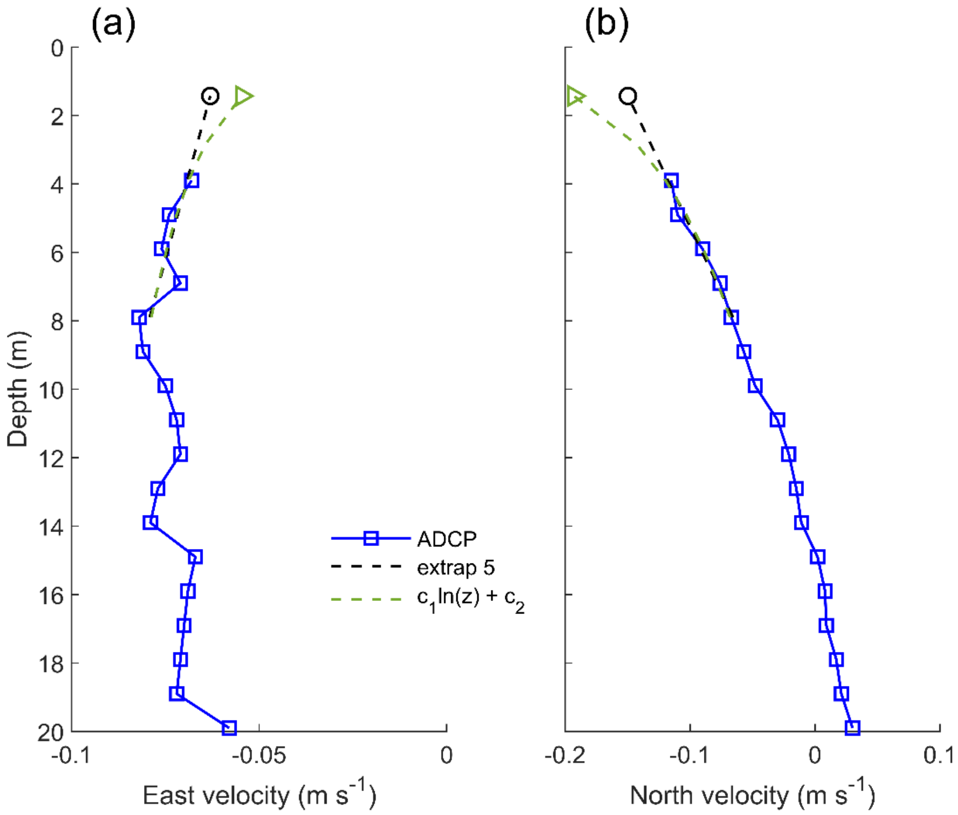

Figure 3.3: Example of current measurements at ADCP1 collected on June 29, 2016 00:50 UTC. A linear extrapolation from the 5 (dashed black line) shallowest ADCP measurements as well as the logarithmic model (dashed green line) are used to estimate velocity at the effective depth (1.4 m, circles and triangles) of the Bragg wave of the HF radars

3.3.4 Wave Spectra: Wave Model

Given a wavefield $[S_{\eta\eta}(f,\theta)]$, the different Stokes drift contributions can be estimated using the expressions shown in (6), (8) and (9). The high frequency 'tail' of the wave spectrum is responsible for a significant proportion of Stokes drift and must be resolved if accurate Stokes drift estimates are desired (Lenain and Pizzo, 2020). Although the ADCP deployed at ADCP1 can estimate a wave spectrum, the large water depth (25 m) does not allow for the estimation of the high frequency wind wave 'tail' of the wave spectrum.

Therefore, numerical results from the Simulating Waves Nearshore model (SWAN; Booij et al. 1999) were used to estimate full directional wave spectra at the ADCP location. The model was set up over an area of 180 km x 165 km with a grid resolution of 830 m. The SWAN boundary conditions were obtained from the WaveWatch III Regional US East Coast (4 arc min) Wave model, provided by the National Centers for Environmental Prediction. The wave bulk parameters recorded in the WaveWatch III database were used to recreate full wave spectra along the open boundaries following the inversion method described in Kumar et al. (2017). The model was forced by winds from the NOAA NAM surface flux fields over the 7-month simulation and wind-wave generation is included. Directional wave spectra outputs were saved at locations ADCP1 and NDBC buoy 41108 (see figure 2).

The bulk wave parameters of wave height (H_s), peak period (T_m), mean wave direction (θ_m) and mean spreading parameter (σ_m) measured from buoy 41108 and the model output at that location are shown in figure 4. The wave height (figure 4a), mean period (figure 4b) and mean direction (figure 4c) from the model and buoy agree well, while the mean spreading parameter (figure 4d) is not as accurately produced by the mode. Additionally, individual spectra are compared between the wave buoy 41108 and the model output there (left column, figure 5) and between measurements from the ADCP at the model output at that location (right column, figure 5). For buoy 41108, the model and buoy agree well up to the 0.5 Hz limit of the wave buoy. The measurements from the ADCP also agree with the model results up to ~0.2 Hz limit of the ADCP. These agreements between the model and wave measurements provide confidence to use the higher frequency wave spectra provided by the model output at the ADCP1 location.

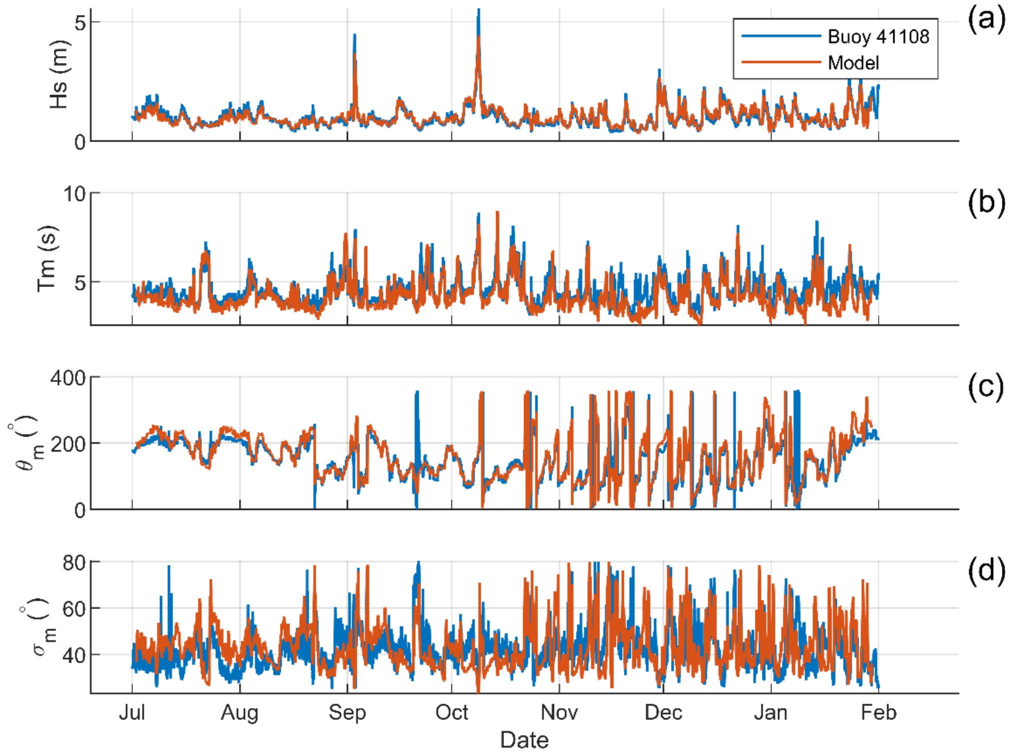

Figure 3.4: Comparison of bulk wave parameters from the wave model (red) and in-situ measurements from wave rider buoy NDBC 41108 (blue) over the data collection period (July 1, 2016 – Feb 1, 2017)

3.4 Results

The HF radar surface current estimate, c_{HF}, is the measured phase speed minus the still water-phase speed, $c_{HF} = c\left[k, h, u(z), S_{\eta\eta}\right] - c_0(k, h)$; equation (1) can be re-arranged and written as

$$c_{HF} = c_E[k, u(z)] + \Delta c_{St}\left(k, S_{\eta\eta}\right), \tag{3.10}$$

where the Eulerian current (c_E) corresponds to the extrapolated ADCP current to the effective depth of the Bragg wave {reducing $c_E[k, u(z)]$ to $u\left(z_{eff}\right)$; see figure 3}. The wave spectra, $S_{\eta\eta}$, is provided by the wave model so that the wave-wave terms, Δc_{St}, given in (6), (8) and (9) can be calculated.

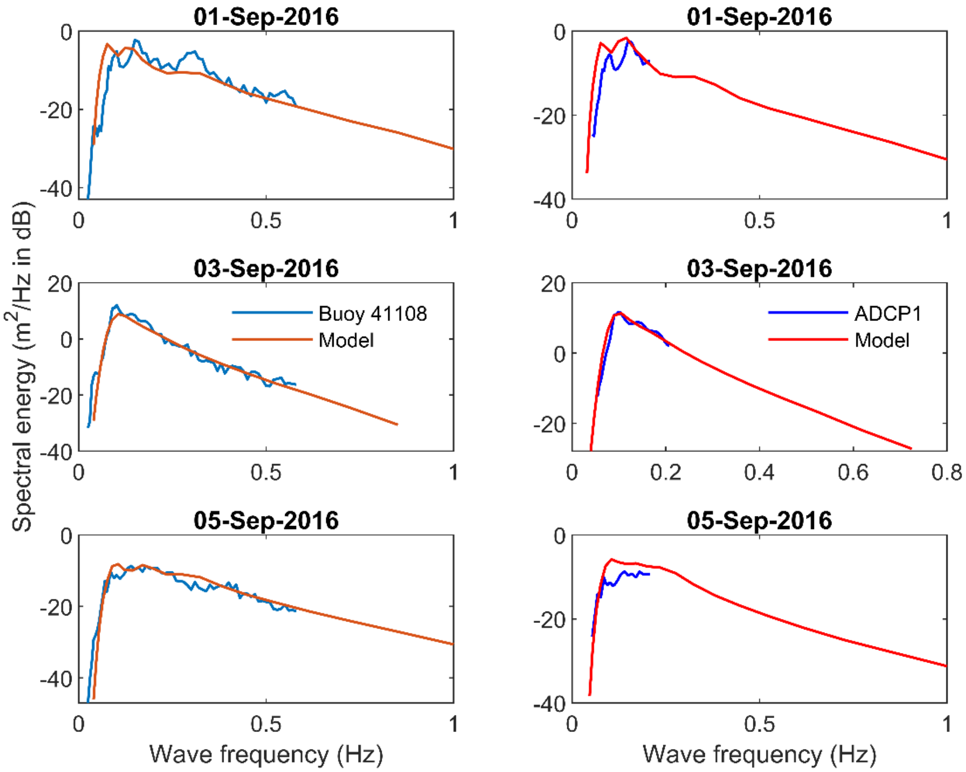

Figure 3.5: Comparison of measured and SWAN estimated wave spectra. Measured spectra are from NDBC Buoy 41108 (left column) and the bottom mounted ADCP at ADCP1 (right column)

3.4.1 Wind and Wave Conditions

Wave heights during the study period ranged from 1 to 2.5 meters (figure 6b) however during early September and October hurricane activity in the region produced wave heights in excess of 4 meters and wind speeds over 20 m/s (figure 6a). The modelled wave spectra (figure 6c) indicate significant energy at the Bragg frequency (see solid white line in figure 6c). During the winter, mid-November to February, the variability in wind and wave height is larger than during the summer months mainly due to the cold and warm front systems found in the region as described in Wu et al. (2017).

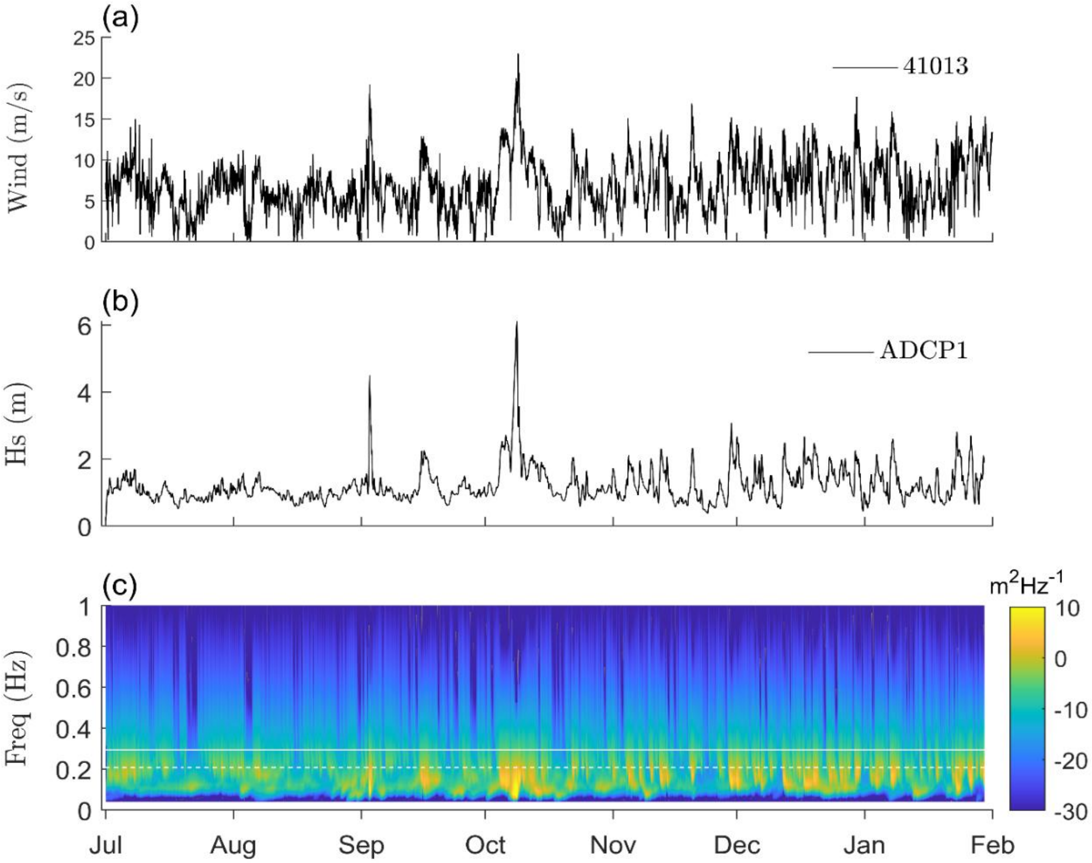

Figure 3.6: Wind and wave conditions during the study period July 1, 2016 to Feb 1, 2017. (a) Wind speed measured at buoy 41013. (b) Significant wave height estimates from the wave model at location ADCP1. (c) Wave spectra from the wave model at location ADCP1; the solid and dashed white lines mark the Bragg and harmonic wave frequencies corresponding to the HF radar used. (d) HF radar surface currents with SNR > 25 dB, from radar sites GTN in blue and CSW in red. (e) Data availability sorted by wave height for each radar site

3.4.2 HF Radar Surface Currents

Following the QA/QC process described earlier only 73 and 58% of the radar radial velocities are available for CSW and GTN, respectively (see figure 6d) . These data are compared to the ADCP data and used to evaluate the three different Stokes drift contribution terms.

Velocity measurements for the first week of September, 2016 are shown in figure 7, with currents from the ADCP, radar estimated surface currents, and winds measured from buoy 41013 with Stokes drift calculated from the wave model spectra. The surface Stokes drift (figure 7) at ADCP1, estimated using the modeled wave spectra and (3) closely follows the wind (figure 7c) measured at 41013. The difference between the HF radar vector surface currents shown in figure 7a and the in-situ currents (figure 7b) is shown in figure 7e. This difference qualitatively resembles the surface Stokes drift (figure 7d) during this time. Although vector currents are shown here, the error in the estimated HF radar current vectors depends on the intersection angle of the two radials (i.e., geometric dilution of precision, Chapman and Graber, 1997). To avoid this error in this study only HF radar radial currents estimates (single site measurements) are used for comparisons, as recommended by Savidge et al. (2011).

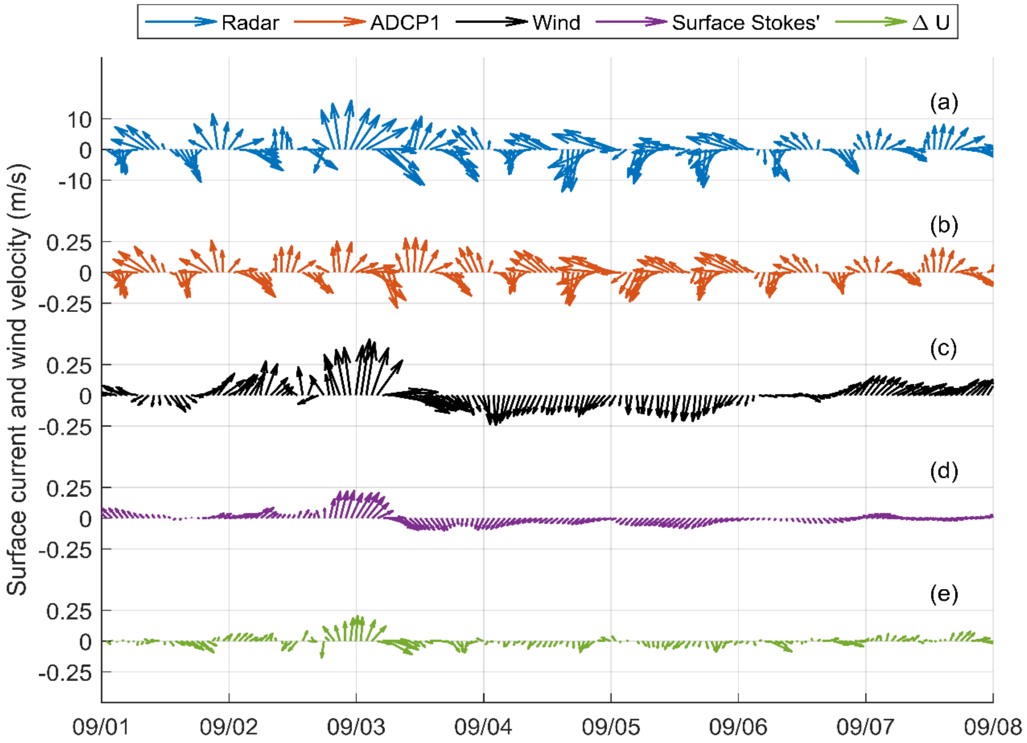

Figure 3.7: Time series of surface current and wind velocity conditions for the period September 1 – 7, 2016 at ADCP1 and buoy 41013, respectively. (a) HF radar surface velocity estimates ; (b) in situ (ADCP) measured velocities;(c) wind velocity vectors; (d) calculated surface Stokes drift at ADCP1; and (e) the difference between the HF radar and in situ velocities

A time series of radial currents from the ADCP and HF radar sites is shown in figure 8c,d (corresponding to the same time period as in figure 7) as solid blue and red lines, respectively. The wave height and wind speed (black and blue lines, respectively) are shown in figure 8a while the filtered Stokes drift estimated from the wave spectra for each radar site is shown in figure 8b. As the wave height increases above 2 meters on Sep 3rd (figure 8a), the filtered Stokes drift term increases significantly (figure 8b). At the same time, the difference between the ADCP (blue) and HF radar (red) measurements increases (figure 8c,d). To produce Eulerian currents from the HF radar, the filtered

Stokes drift (Δc_F) is subtracted from the HF radar measurement (see 10), and the result is shown as the black line in figure 8c,d. This corrected HF radar current (black line) shows significantly better agreement with the ADCP measurements (blue line) than the uncorrected radar estimates (red line) for both GTN (figure 8c) and CSW (figure 8d) data.

The differences between the different Stokes contribution terms are quite small. The HF radar currents corrected using the filtered, effective and half Stokes are shown for the 12 hours before and after Sep. 3rd for GTN (figure 8e) and CSW (figure 8f). The differences between the different Stokes contribution terms are small and it is not clear which term is most appropriate. We note that for CSW on Sep 3rd at 00:00 (figure 8f), the HF radar currents corrected using the filtered Stokes (black) show better agreement with the ADCP data than those corrected using the effective Stokes (green line) or half Stokes (magenta line) terms.

As shown in figure 8, the Stokes contribution terms are much larger when wave heights are higher; the filtered Stokes terms increase significantly on Sep. 3rd for both radar sites (figure 8c,d), but are close to zero on Sep. 1st when wave heights are lower. This wave height dependence is explored further by sorting the HF radar derived surface velocities (figure 6d) by wave weight (see figure 6e). As we might expect at low wave conditions (<1m) the small Stokes contribution terms (see figure 8b on Sep. 1st) are masked by noise.

Most of the data available correspond to wave height conditions between 1 and 2 meters (41 and 33% for CSW and GTN, respectively) while data corresponding to wave heights greater than 2 meters represent only around 5% of the data, for both radar sites. However, given the 7 month data set, there are still over 258 HF radar measurements for each radar site, with wave heights over 2 meters (figure 6e).

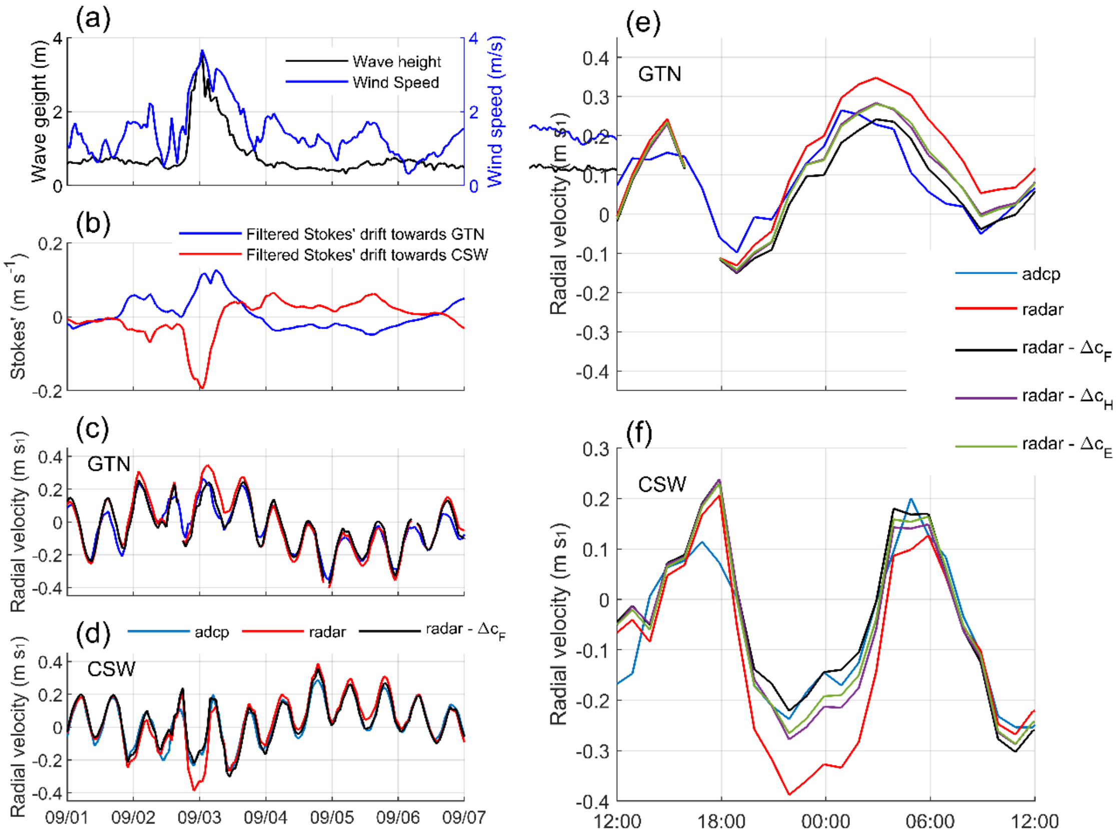

Figure 3.8: **:** (a) Time series of wind speed and wave height. (b) Time series of the filtered Stokes (Δc_F) terms for GTN and CSW. (c) Time series of in-situ (ADCP), HF radar and HF radar radial velocities without Stokes contribution terms for GTN. (d) as before for CSW. (e),(f) same as (c) and (d) but for only Sep. 3rd +/- 12 hours. Key: ADCP: blue, HF radar=Red, HF radar - Δc_F = black, HF radar- Δc_E= green, HF radar- Δc_H= magenta

The outcomes of linear regression (for all data available) analysis between the ADCP radial velocities and (i) the HF radar radial velocity estimates and (ii) the HF radar radial velocity estimates corrected for Stokes drift contributions (HF radar minus Δc_{St}, as in figure 8e-f) are presented in the form of Taylor Diagrams in figure 9a-c while the corresponding statistics are given in table 1. As expected, the HF radar currents (circles in figure 9a-c) correlate well (>0.9) to the in situ ADCP measurements. The effective Stokes (right triangle) and half surface Stokes (left triangle) are very similar for all wave heights and seem to overlap for wave heights > 2 m (figure 9c). This might be expected as the effective Stokes is very close to half Stokes for strong wind speeds at 8.3 MHz as shown by the dashed black line in figure 1d. When only wave heights greater than 2 meters are considered, the Stokes drift contributions lie significantly closer to the in situ measurements than the radar measurements (compare squares and triangles to circles in figure 9c). Although correlations are similar, the RMSE values of 6.1 and 6.2 cm/s are reduced to ~3.7 and ~4.3 cm/s for CSW and GTN, respectively (table 1) for these higher wave heights.

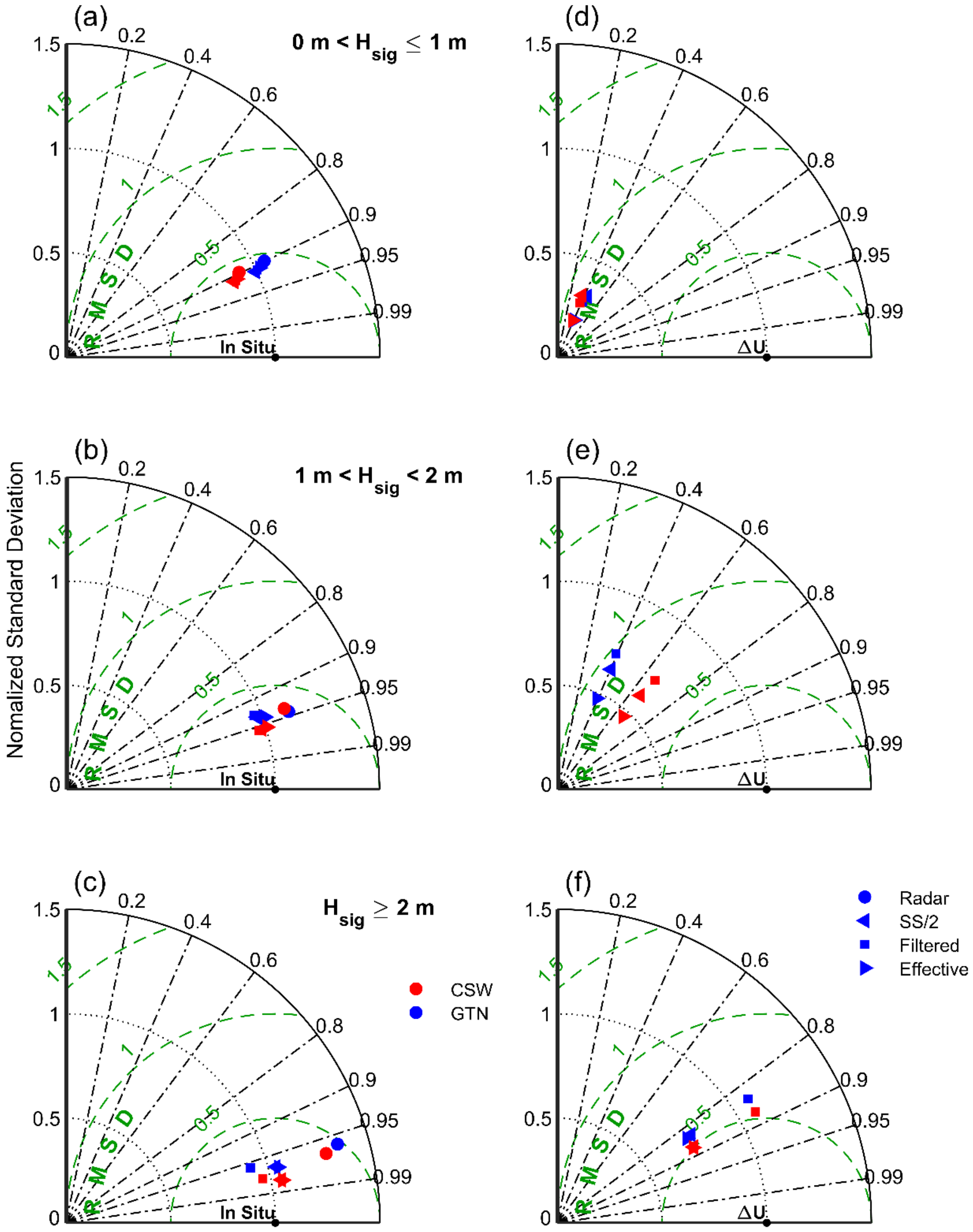

Figure 3.9: Comparisons between the HF radar radial current estimates using the Bragg wave and in situ measurements. Stokes drift contributions are subtracted from the HF radar measurements and compared to the in situ measurements in a-c. In d-f, the difference between the HF radar and in situ measurements are compared to the Stokes drift contributions. $\Delta U = c_{HF} - c_E$ which should be equal to the Stokes drift contribution following (10)

In figure 9d-f we compare the difference between the ADCP and HF radar measurements ($\Delta U = c_{HF} - c_E[k, u(z)]$) to the Stokes drift contribution terms (Δc_{St}). Other than noise, these terms should be equal to each other (see 11). For wave heights less than 1 m the Stokes drift contribution terms have a correlation to the difference, ΔU, of $R \approx 0.40$ (figure 9d) which increases to 0.85-0.90 for wave heights greater than 2 meters (figure 9f). For wave heights over 2 meters, the Stokes drift contribution terms have R^2 values of 0.79 and ~0.73 for GTN and CSW, respectively (table 1). Although all three contribution terms have almost identical R^2 and RMSE values (table 1), the filtered Stokes drift term has a larger standard deviation (figure 9d-f) than effective Stokes drift or half surface Stokes drift that more closely aligns with the standard deviation of the difference (ΔU).

Table 3.1: Statistics corresponding to figure 9. The statistics for the fitted lines between the HF radar surface currents (with and without Stokes contributions) compared to the ADCP measurements in the GTN and CSW columns, corresponding to figures 9a-c. The statistics for the difference between the HF radar and ADCP measurements compared to the Stokes drift contribution terms are in the GTN difference and CSW difference columns and correspond to figures 9d-f.

		GTN				CSW				GTN difference				CSW difference			
		m	b	R^2	RMSE	m	b	R^2	RMSE	m	b	R^2	RMSE	m	b	R^2	RMSE
Hsig < 1m	No Stokes	1.1	1.0	0.88	6.2	1.0	0.6	0.87	5.8								
	SS/2	1.0	0.8	0.89	5.2	1.0	0.1	0.91	4.3	1.0	0.7	0.35	5.3	1.2	0.2	0.46	4.3
	Filtered	1.0	0.8	0.88	5.4	0.9	0.1	0.91	4.2	0.8	0.8	0.32	5.5	1.0	0.1	0.45	4.3
	Effective	1.0	1.0	0.89	5.4	1.0	0.3	0.91	4.5	1.3	1.1	0.32	5.5	1.5	0.3	0.45	4.5
	Shear	1.1	0.8	0.87	6.3	1.0	0.5	0.86	5.9	0.6	0.9	0.06	6.4	0.5	0.5	0.04	5.8

	Filtered$_{net}$	1.0	0.4	0.86	5.7	0.9	0.7	0.88	4.9	0.7	0.6	0.31	5.7	0.7	0.7	0.34	5.0
2m> Hsig >= 1m	No Stokes	1.2	0.6	0.90	6.0	1.1	1.0	0.89	5.7								
	SS/2	1.0	0.6	0.90	5.1	1.0	0.1	0.93	3.9	1.0	0.6	0.39	5.1	1.2	0.0	0.58	3.9
	Filtered	1.0	0.5	0.89	5.2	1.0	0.2	0.93	3.8	0.8	0.5	0.38	5.3	1.0	0.1	0.57	3.9
	Effective	1.0	0.8	0.91	5.2	1.0	0.4	0.93	4.1	1.1	0.8	0.38	5.2	1.4	0.2	0.57	4.1
	Shear	1.1	0.4	0.90	6.0	1.1	0.9	0.89	5.6	0.8	0.6	0.07	6.3	0.8	0.7	0.08	5.8
	Filtered$_{net}$	0.9	0.4	0.87	5.6	1.0	0.4	0.91	4.5	0.7	0.5	0.34	5.7	0.8	0.5	0.45	4.5

Hsig > =2m	No Stokes	1.3	0.7	0.92	6.2	1.3	1.3	0.93	6.1								
	SS/2	1.0	0.7	0.94	4.3	1.0	0.5	0.96	3.7	1.1	0.8	0.72	4.3	1.2	0.4	0.79	3.8
	Filtered	0.9	0.5	0.92	4.2	1.0	0.1	0.96	3.8	0.8	0.6	0.73	4.6	0.8	0.3	0.79	3.9
	Effective	1.0	1.0	0.94	4.3	1.1	1.0	0.97	3.7	1.2	1.1	0.73	4.4	1.2	0.9	0.79	3.9
	Shear	1.3	0.9	0.92	6.4	1.2	1.3	0.93	6.2	0.6	0.4	0.02	8.0	1.3	0.7	0.16	7.2
	Filtered$_{net}$	1.0	1.1	0.93	4.5	1.1	1.0	0.94	4.8	1.0	1.0	0.69	4.6	1.0	0.9	0.61	4.9

3.5 HF radar Stokes drift self-correction

To self-correct the HF radar at all ranges that surface currents are estimated, utilization of the first order Bragg peak signal is required. HF radar estimates of wind speed and direction have been suggested using the first order Bragg peaks only (Shen et al. 2012; Kirincich et al. 2016). These methods utilize the fact that the Bragg waves are wind driven waves and therefore any variation in the wind is reflected in the Bragg waves' direction and wave height which cause a variation in the energy level of the first order Bragg peaks. We note here that this method is limited to the range of wind speeds that drive the Bragg waves. The minimum wind speed that can drive the Bragg waves is approximately equal to their phase speed (Hasselmann et al. 1980). At high wind speeds there is a limit after which the waves reach a saturation point and stop increasing in wave height (Shen et al. 2012). For an 8.3 MHz radars (18 m Bragg waves) like those used in this study, the minimum and saturation point wind speeds are 5.3 m/s and ~15 m/s, respectively.

Despite these limitations, it is suggested that HF radar estimates of wind speed and direction could be used to estimate the Stokes drift contribution terms using a theoretical wind sea spectrum such as JONSWAP (Hasselmann et al. 1973). The relationship between wind speed and the first order Bragg peaks is nonlinear and a function of the HF radar range in addition to wind speed and direction (Kirincich et al. 2016). A common practice is to train a neural network to predict the wind speed and direction given the amplitude of the first order Bragg peaks from two or more radar systems (Shen et al. 2012; Zeng et al. 2016). Unfortunately, due to the highly nonlinear nature, neural network training must be carried out for each location wind speed and direction estimates are desired. For example, the radar system used here has 3 km range resolution for HF radar surface current estimates. For any location that wind estimates are desired, the radar system must be trained with wind measurements at that location making it a laborious exercise.

When estimating wind speed using two radar sites, the input is the signal level of the four Bragg peaks (two Bragg peaks from each site) and the desired output is wind speed and direction. For each Bragg peak, the width of the peak is determined by fitting a Gaussian function to it. The full width at half maximum of the Gaussian function is used to integrate the signal of the Bragg peak, giving the total energy in the Bragg peak (as described in Alattabi et al. 2019). For most radar applications, the signal to noise ratio is used, however for wind inversion, variation in noise may mask the variation in the Bragg peak amplitudes due to wind changes. Therefore, the Bragg peak energies are used directly to train the neural network as in Shen et al. (2012).

The Bragg peak energies of the four Bragg peaks from radar sites CSW and GTN are used as input for a neural network model to predict wind speed and direction at location ADCP1. Although wind measurements are not available at this location, wind data from buoy 41013 are used to train the neural network; the wind field is not expected to have large variation between these two locations that are separated by 55 km in the open ocean. Two neural networks were assessed in their accuracy for wind inversion: single hidden layer networks consisting of 2-50 nodes and two hidden layer networks consisting of 2-25 nodes in each layer. Once more than 10 nodes were used, results were similar between the networks but it was found that the most accurate network used here consisted of 2 layers with 24 nodes in the first layer and 15 nodes in the second layer.

The training data was limited to wind speeds between 5 and 15 m s^{-1} and consisted of a random sample using 30% of the total dataset. The predicted wind speed and direction for the entire dataset for wind speeds between 5 and 15 m s^{-1} is shown in figure 10a,b. Additionally, the predicted 'radial wind speed', or the predicted wind along the radial direction at ADCP1 for CSW and GTN are shown in figure 10c,d.

The predicted wind speed from the neural network correlates to the measured wind speed at buoy 41013 with an R^2 value of 0.41 and an RMSE of 1.3 m s^{-1} (figure 10a) while the wind direction correlation has an R^2 of 0.54 (figure 10b) and an RMSE of $54.5°$ (figure 120). The accuracy presented here is similar to other studies of HF radar wind inversion (Shen et al. 2012; Kirincich et al. 2016). The large RMSE in wind direction prediction results in poor radial wind speed predictions for both CSW (figure 10c) and GTN (figure 10d) with R^2 values of 0.22 and RMSE values of 6.5 and 6.7 m/s. This is not sufficient accuracy for the creation of a wave spectrum that could then be used to calculate the Stokes drift contribution terms.

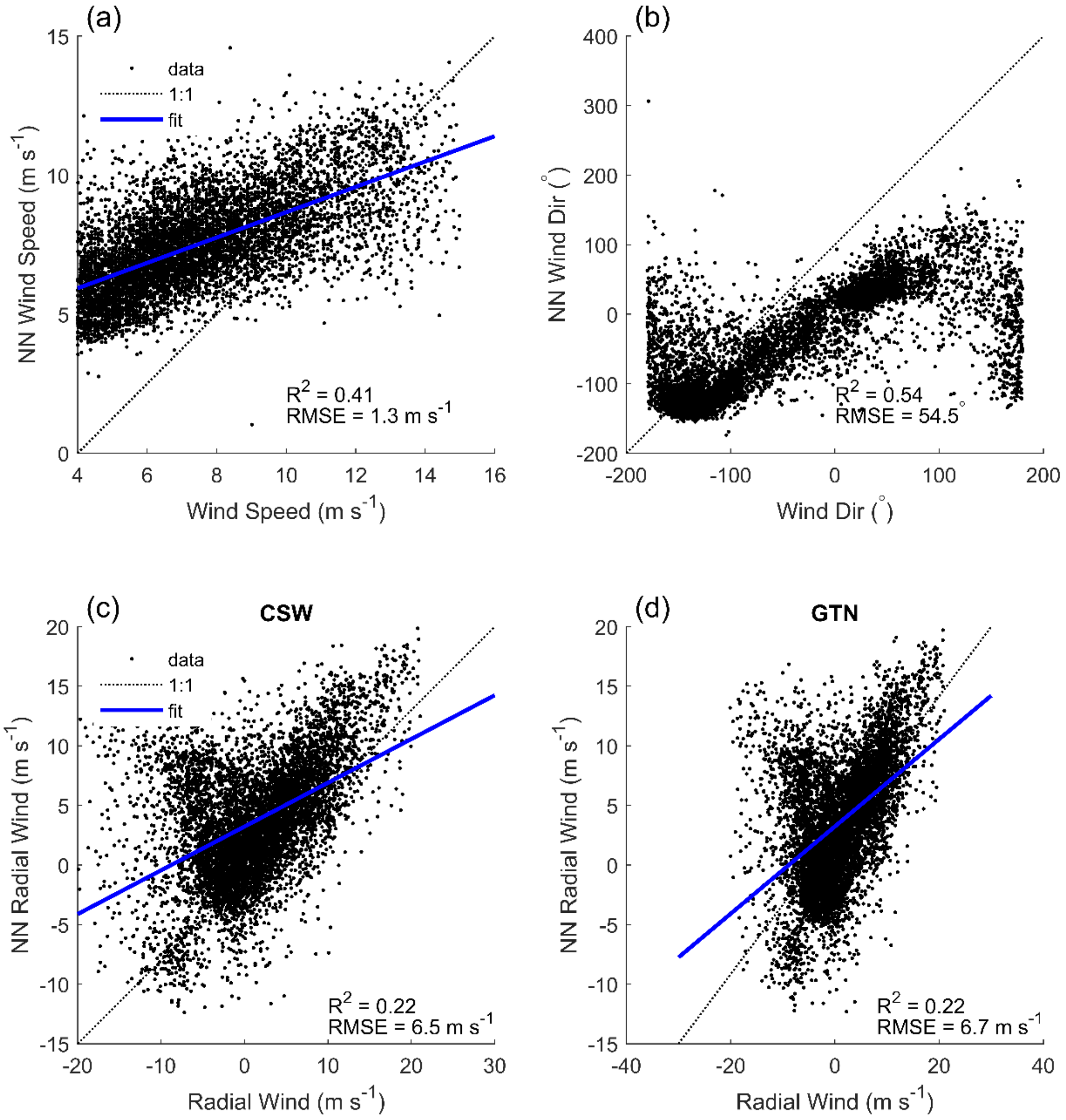

Figure 3.10: Neural network (NN) prediction of wind speed (a) wind direction (b), wind projected along the radial direction at ADCP1 for CSW (c) and GTN(d), after being trained, compared to measured winds at buoy 41013

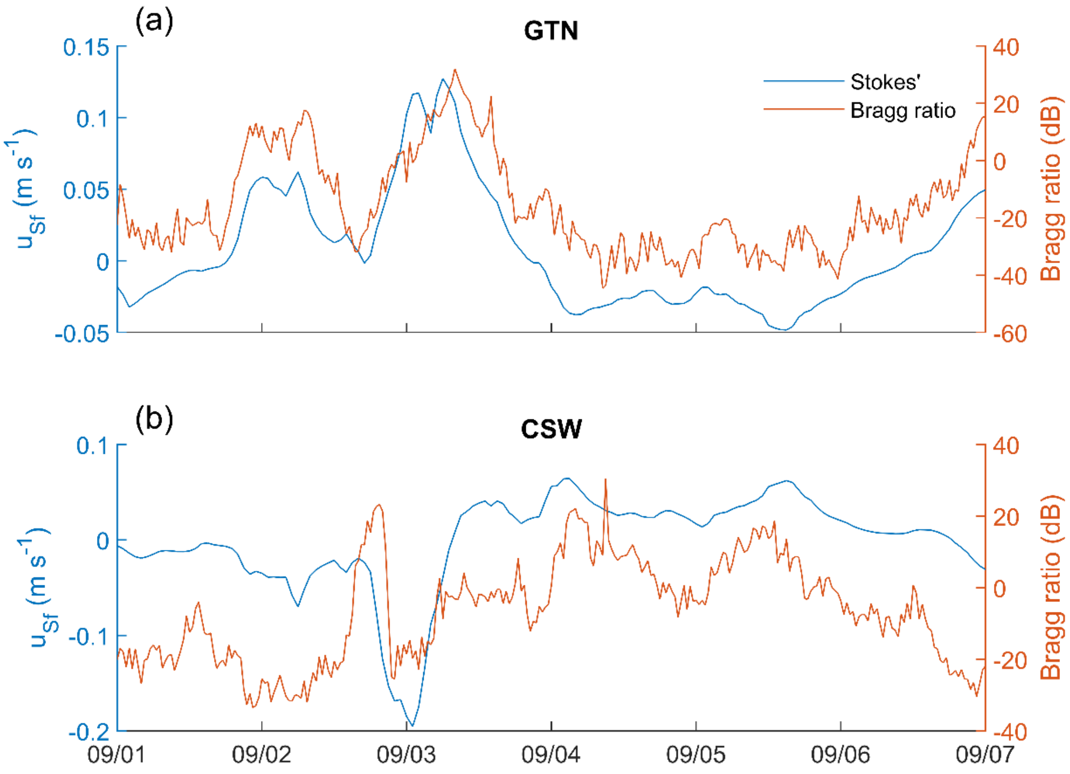

Figure 3.11: Example of current measurements at ADCP1 collected on June 29, 2016 00:50 UTC. A linear extrapolation from the 5 (dashed black line) shallowest ADCP measurements as well as the logarithmic model (dashed green line) are used to estimate velocity at the effective depth (1.4 m, circles and triangles) of the Bragg wave of the HF radars

Given the limitations of using neural network methods to estimate wind from the Bragg peaks, the possibility to directly estimate the Stokes drift contribution terms is examined. This approach is motivated by the fact that the ratio of the positive to negative Bragg peak amplitudes is directly related to directional spectrum of the Bragg waves. Additionally, a comparison between estimates of radial surface Stokes drift from the wave estimates and the ratio of the Bragg peak amplitudes (see Figure 11) shows a good correlation between them, for both radar sites GTN and CSW.

A neural network was trained as before but using the radial filtered Stokes contribution term for each radar site instead of wind speed and direction as the desired output. The same wind speed limits of 5 and 15 m s^{-1} were used and the neural network was the same size as before, 2 layers with 24 nodes in the first layer and 15 nodes in the second layer. Again, the training data was limited to a random sample of 30% of the total dataset.

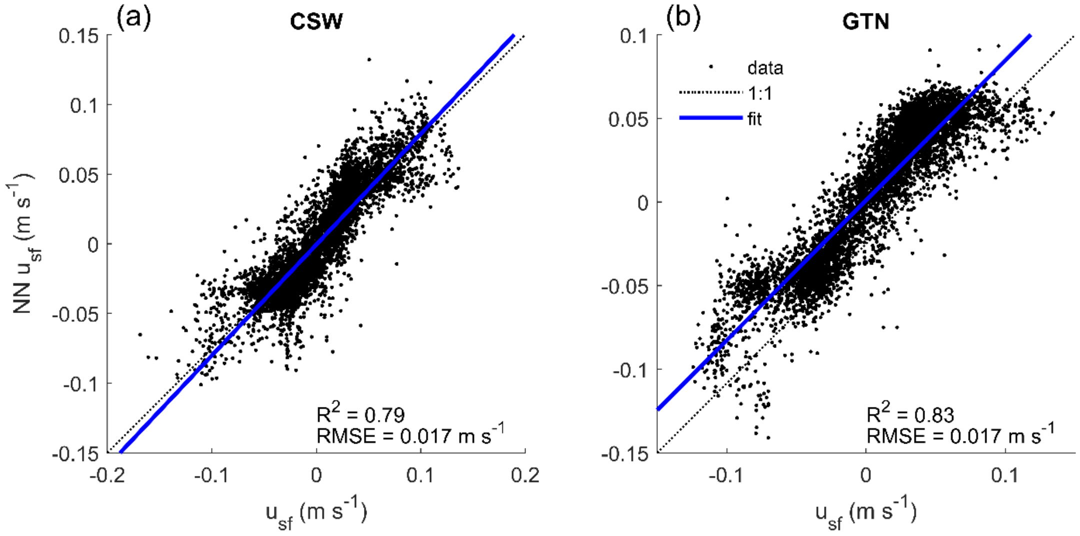

Figure 3.12: Neural network (NN) prediction of the radial filtered Stokes drift for CSW (a) and GTN (b) after being trained, compared to the filtered Stokes drift terms calculated from the wave model

The results for the predicted filtered Stokes drift for CSW and GTN from the neural network are compared to the filtered Stokes drift terms calculated from the wave model in figure 12. The correlation is much higher than wind speed prediction with R^2 values of 0.79 and 0.83 and RMSE values of 1.7 and 1.7 cm s^{-}1 for radar sites CSW and GTN, respectively. These results allow the radar to correct itself at the ADCP1 location using the trained neural network.

The results from this self-correcting method are shown in figure 13 and are similar to those derived using the wave model estimated filtered Stokes term (see figure 9). As before, higher wave height leads to the contribution term explaining a larger percentage of the difference between the HF radar measurements and the ADCP measurements. At wave heights over 2 meters (figure 13f), the neural network predictions at GTN have an R^2 of 0.69 while the filtered Stokes contribution term from the wave model has an R^2 of 0.73. For CSW, the neural network has an R^2 of 0.61 while the wave model result is 0.79 (table 1).

We may expect the neural network to perform well during wind seas but have difficulty during swell. Swell is known to be hard to predict during wave inversion of the HF radar signal and special methods were developed specifically for swell (Want et al. 2014; Al-Attabi et al. 2019). The Bragg waves are wind driven and therefore swell should not cause much, if any, variation in the Bragg peak amplitudes, while it could change the predicted Stokes drift term. We investigate the effect of swell using a short time series of the filtered Stokes term calculated using the wave model and compare it to the neural network predicted values (figure 14). On Dec 4, 2016, some swell is present along with the wind sea above 0.2 Hz (figure 14); shortly after, on Dec 5 there is only a strong wind sea (figure 1). For both GTN and CSW, the predicted values (shown in red in figure 14c) deviate from the wave model derived values (shown in blue) more during the swell sea on Dec 4 (black squares in figure 14c,d) than during the wind sea on Dec 5 (circles).

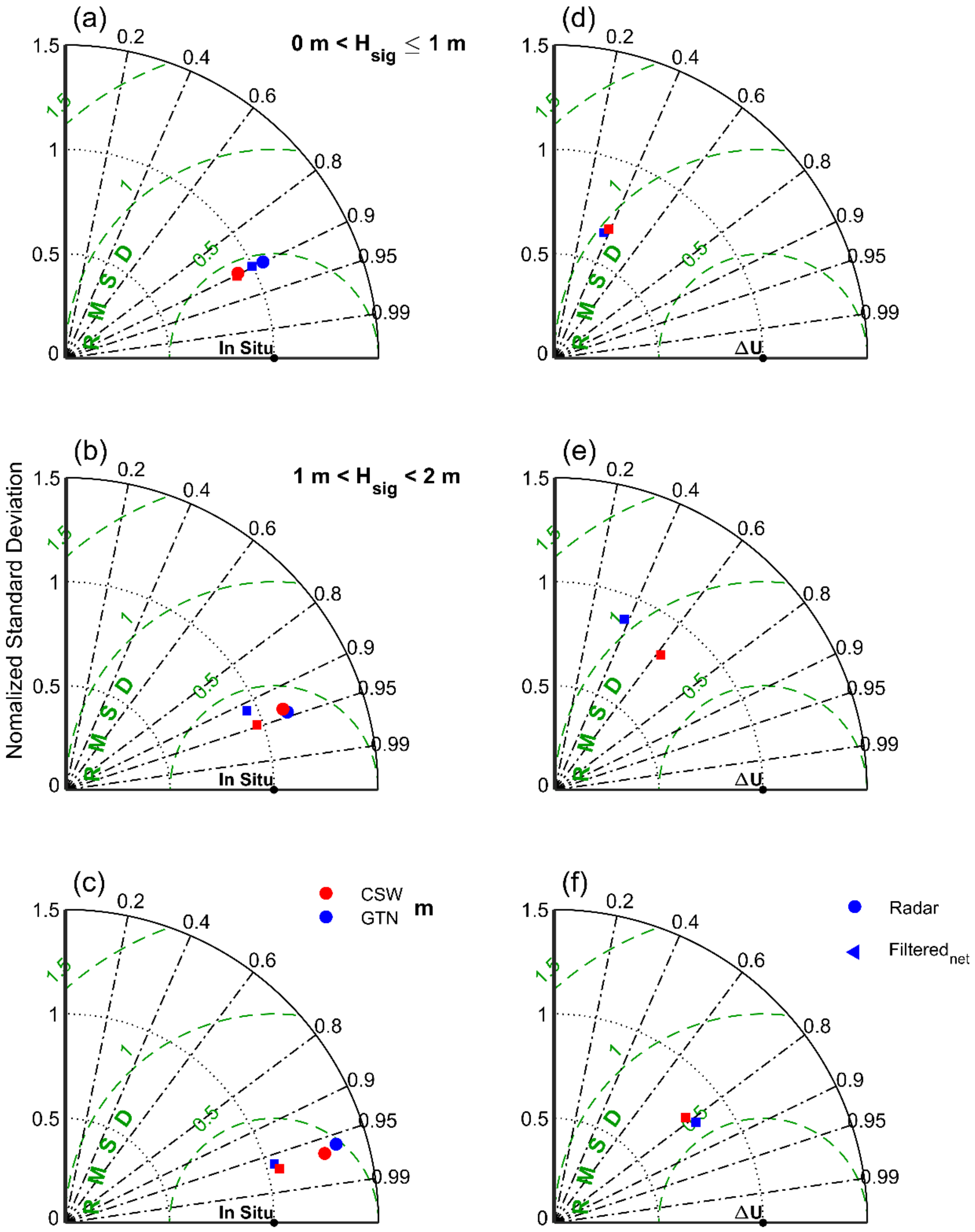

Figure 3.13: Comparisons between the HF radar surface current estimates using the Bragg wave and in situ measurements as in figure 11 but with filtered Stokes drift estimated using the trained neural network.

The deviation of the predicted filtered Stokes drift term is only a few cm s^{-1}, but these data represent an area with limited swell presence. This effect may be more significant in areas with significant swell presence.

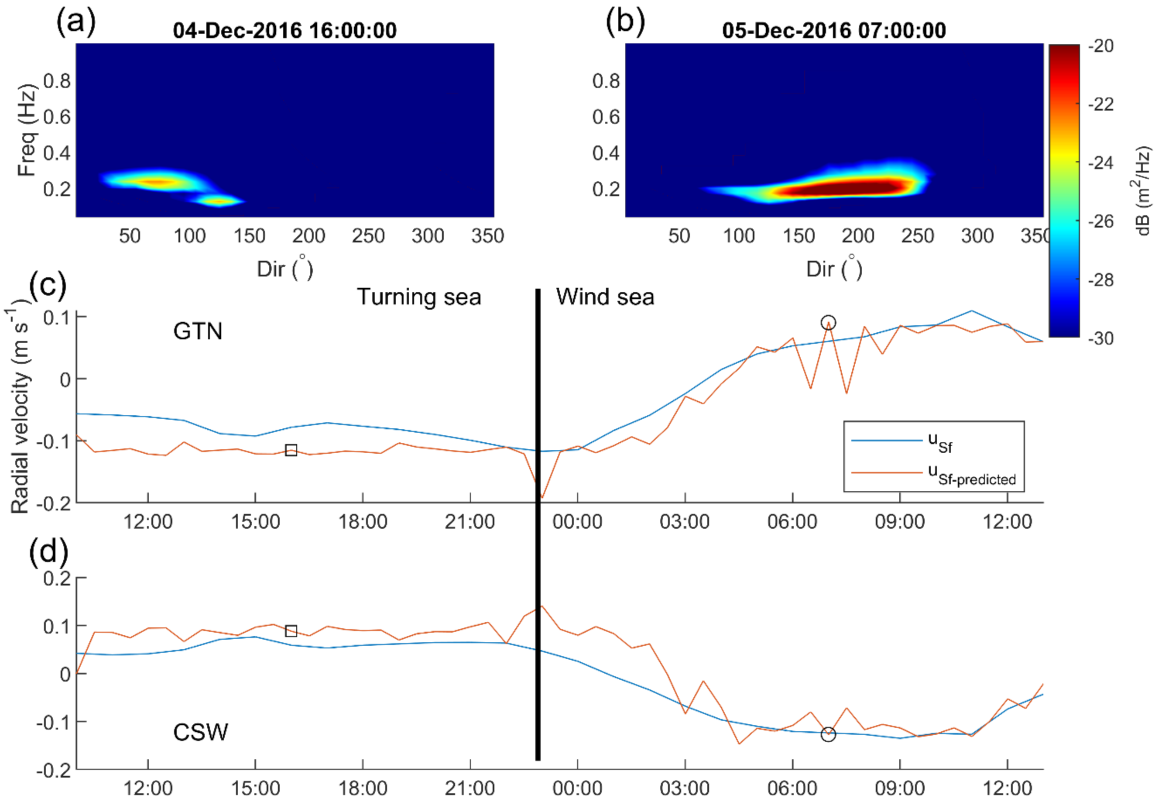

Figure 3.14: Wave model spectra showing swell and wind seas (a) and at a later time only a wind sea (b). Filtered Stokes drift calculated from the wave model are shown in blue for GTN (c) and CSW (d) while the neural network predicted values of filtered Stokes are shown in red

In turning sea conditions, i.e., when the wind changes direction, the higher frequency waves will turn first. This creates the situation where the Bragg peaks will change in direction after higher frequency waves have turned. On Sep 3, 2016, turning seas are visible in the wave model spectra (figure 15a). Later that same day, the high frequency turning sea decayed (figure 15b). The predicted term for both CSW and GTN has a large difference to the wave model results during the turning seas (black squares in figure 14c,d), while they agree with the wave model after conditions return to wind driven seas (black circles in figure 15c,d).

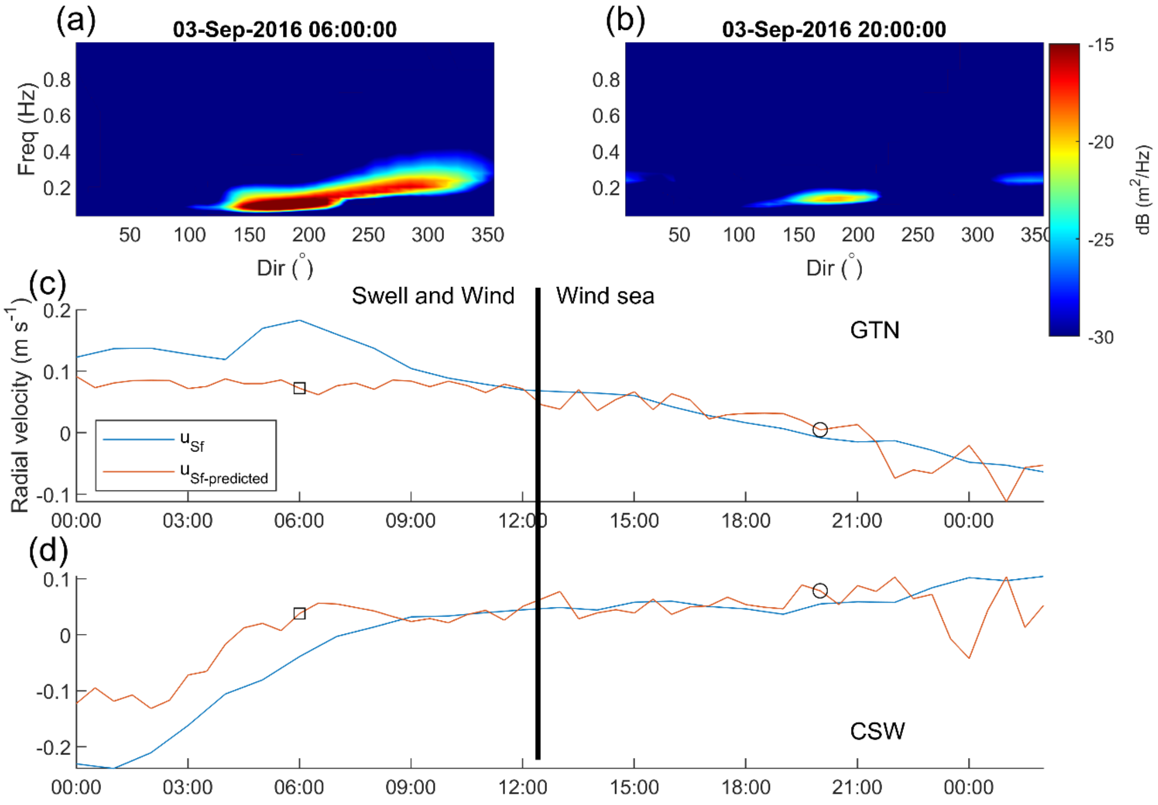

Figure 3.15: Wave model spectra for (a) a turning sea and (b) no-turning wind sea . Filtered Stokes drift calculated from the wave model (blue line) and the neural network (red line) for (c) GTN and (d) CSW

3.6 Conclusion

Our analysis has showed that all Stokes drift contribution terms (filtered, effective, or half surface Stokes) can explain a significant fraction of the difference between the HF radar measurements and the Eulerian in-situ measurements. Although not conclusive, qualitatively it can be argued that filtered or effective Stokes drift is more appealing than half surface Stokes. Unlike half surface Stokes, both filtered and effective Stokes approach zero for long wavelengths and close to full surface Stokes for short wavelengths. Additionally, filtered Stokes is based on sound theoretical underpinnings, while there are arguments that effective Stokes is not. At wave heights over 2 meters, the filtered Stokes term explained roughly 80% of the difference between the HF radar and ADCP radial current measurements, as did effective Stokes and half surface Stokes. However, the standard deviation of filtered Stokes more closely agreed with our data and therefore performed marginally better than the other two.

Finally, it was shown here that it is possible to train a neural network using the Bragg peak amplitudes from 2 radar sites to predict the filtered Stokes drift term with a relatively high accuracy, capable of explaining 60-70% of the difference between the radar and ADCP measurements. This allows the radars to be self-correcting for a much larger area than attempting to use wave inversion for the self-correction methodology, although it would require training data over the entire radar coverage area.

As the method of estimating surface currents through the phase speed measurements of surface gravity waves is utilized on more platforms and gains in popularity, the need to identify what part of Stokes drift is included in the wave phase speed becomes more critical to attain accurate current estimates. Additionally, research that uses multiple wavelengths to determine vertical shear needs to consider the variation of Stokes drift between the different wavelengths in order to accurately determine the Eulerian vertical current shear. Finally, the Bragg wavelengths of operational HF radars correspond to the wavelengths with the most variation in the Stokes drift contribution terms, thereby making them an ideal platform for further research into this question.

While HF radars can provide the phase speed measurements, detailed measurements of the upper water column are needed. The common HF radar operating frequencies have effective depths ranging from 4 m at 3 MHz to 0.24 m at 50 MHz. While currents at the former depth are easily measured with traditional instruments, the latter requires novel techniques, such as the newer small autonomous platforms that sample near the surface.

CHAPTER 4

EDDY IDENTIFICATION AND MOMENTUM FLUX ACROSS THE SHELF BREAK IN LONG BAY SC, USING HF RADARS

Abstract

Data from two HF radar systems covering Long Bay, off South Carolina, USA are used to study eddies and the semi-permanent ocean feature called the Charleston Gyre. The latter is a large eddy occurring in the area as a consequence of the deflection of the Gulf Stream by the Charleston Bump

Eddies are identified using the winding-angle method, which is optimized herein for HF radar data. Over 200 eddies lasting more than 6 hours were identified in the HF radar surface current data set spanning 2013. All but 1 of the eddies lasting over 48 hours were cyclonic upwelling eddies on the shelf break, representing the Charleston Gyre. Most of these 48+ hour eddies moved downstream with the flow of the Gulf Stream, however some propagated onshore or upstream, showing the semi-permanent nature of the Charleston Gyre.

Momentum flux across the shelf break in Long Bay is consistently lower than previous studies where the flux is measured further offshore. Additionally, momentum flux across the shelf correlates to anticyclonic eddies near the shelf break. While there is some correlation ($R^2 \approx 0.2$) of the momentum flux across the shelf in Long Bay SC to the Florida current transport (representative of the Gulf Stream transport), there is more correlation to eddies near the shelf break ($R^2 \approx 0.4$). Additionally, we detail the passage of an anticyclonic eddy near the shelf moving equatorward and its associated momentum flux across the shelf break. Finally, we find that the anticyclonic shelf break eddies in this area tend to propagate to the west-southwest and are preferentially spun up during times of northwards winds that induces Ekman transport to the west.

4.1 Introduction

It is known that the Gulf Stream, after passing through the Florida Straits, flows along the shelf break until encountering the Charleston Bump off the coast of Charleston, SC, where it is deflected as it flows over the bump (Brooks and Bane, 1978; Bane and Dewar, 1988). Meanders, spin-off eddies, and the semi-permanent Charleston Gyre are formed just downstream of the Charleston Bump, near the shelf break in Long Bay, SC and Onslow Bay, NC (McClain and Astkinson, 1985; Bane and Dewar, 1988; Blanton et al., 2003).

The Charleston Gyre is cyclonic (upwelling) and is known to be important for bringing nutrients to the surface (Lee et al., 1991; Govoni et al., 2013), making it an important spawning location for Atlantic Menhaden (Govoni et al., 2013) and Swordfish (Hsu et al., 2015). The former makes up the largest fishery by volume on the east coast of the USA (Anstead et al., 2021) while the latter supports a large sport fishery. Lee et al. (1991) used current meter data to estimate momentum fluxes across the shelf in that region. The results showed a positive cross-shore flux (i.e., momentum towards the Gulf Stream) which may contribute to acceleration of the GS in the area. In that study and in this paper positive flux is defined as downstream (where downstream is in the direction of GS flow, towards east-northeast) momentum going from the shelf towards the GS, or upstream (where upstream is opposite GS flow, towards west-southwest) momentum from the GS going onto the shelf. The same study indicated that although the flux was consistent toward the GS, it did vary in the alongshelf direction by a factor of 8 between 32.5° and 33.5° N (from 50 to 413 $\mathrm{cm^2\ s^{-2}}$).

Two HF radar sites installed on the shores of Long Bay, SC in 2012 provide an opportunity to study eddies and momentum flux across the shelf break, just downstream of the Charleston Bump. The HF radar surface current estimates are known to be accurate (Paduan and Washburn, 2013) and have been used to identify eddies before (e.g., Bagaglini and Zambianchi, 2017; Schaeffer et al., 2017; Savidge et al., 2010). Additionally, they have already been validated in this area (Cahl et al., 2023).

While eddies in surface current data sets produced by HF radars are easily identified visually, several computational methods have been developed that allow automation of the method especially for larger data sets. Traditional methods like the vector geometry method (Nencioli et al., 2010), the Okubo-Weiss parameter (Okubo, 1970; Weiss, 1991), and the winding-angle method (Sadarjoen and Post, 2000) have been widely utilized. More recently, neural network methods (Savidge et al., 2010; Liu et al., 2020) have also been used to identify eddies but they require extensive training data sets. The latter require the involvement either visual identification by humans or the use of one of the more traditional techniques described above. The successful application of a traditional method may provide future neural networks with an automated training data set thereby reducing the time consuming method of training neural networks for eddy identification. However, the application of neural networks for this data set is beyond the scope of this paper.

Although the Okubo-Weiss parameter and vector geometry method have both shown success in eddy identification (Isern-Fontanet et al., 2003; Pasquero et al.,2001; Chelton et al., 2007), more recently comparisons between the Okubo-Weiss parameter, Vector-Geometry and the winding-angle method has shown the winding-angle method to be the most accurate (Chaigneau et al., 2008; Chaigneau et al., 2009; Viikmäe and Torsvik, 2013; Souza et al., 2011; Xing and Yang, 2021). Although there are now many more eddy identification routines available (e.g., Lian et al., 2019), but the winding-angle method has shown good results and is effective with HF radar measurements (Kim, 2010). Therefore, the winding-angle method is used herein and optimized for use with HF radar data sets.

This paper is organized as follows; In section 2, a description of the HF radar surface current data is given. In section 3 the winding-angle method and its application to HF radar surface current measurements is detailed, along with momentum flux calculations across the shelf. The results from eddy identification and momentum flux across the shelf are given in section 4. Finally, discussion are made in section 5 and conclusions in section 6.

4.2 Data

Two 8.3 MHz HF radars sites (blue squares in figure 1), located at Georgetown SC (GTN) and Fort Caswell NC (CSW), provided surface current estimates over Long Bay, SC. Their boresights were directed towards the middle shelf (black arrows in figure 1) and the 12 antenna linear arrays limit the surface current estimates to $\pm 60^\circ$ from their boresights. Both radars use a 50 kHz bandwidth giving a 3km range resolution. The radars operated in FMCW with GTN chirping upwards and CSW chirping downwards allowing simultaneous transmission without interference. The radars use 15 minute acquisitions (repeated every 30 minutes) to estimate radial currents, which are then combined onto a 3x3 km grid (see Cahl et al., 2023 for further details).

Along the baseline (the line connecting the two radar sites), vector currents are not calculated as the geometric dilution of precision (Chapman and Graber, 1997) is too high (GDOP > 2.5) which signifies that the error in the magnitude of the calculated vector currents are ≥ 2.5 times the error of the individual radial currents in the areas where we do not calculate vector currents. Before combining the radial measurements from both sites to calculate vector currents additional QA/QC is performed that included the creation of radial current rime-series at each surface current estimate location, and their comparison with a 5 point median sort filtered timed series (Justusson, 1981) to identify and remove outliers. After this the radial currents are combined to create vector current estimates on a 3x3 km grid (e.g., Paduan and Washburn, 2013).

Since tidal currents may mask underlying eddy features, the radial currents (after QA/QC) are low pass filtered using a low pass filter (Rosenfeld, 1983) with a 33 hour cutoff. These low-pass filtered data are combined to create subtidal vector currents that are used to identify eddies. Offshore winds measured at NDBC buoy 41013 (Frying Pan Shoals, NC) located at $33.441°$ N, $77.764°$ W are used to assess wind conditions (and how these correlate to when and where eddies are detected), data is available at https://www.ndbc.noaa.gov/station_page.php?station=41013.

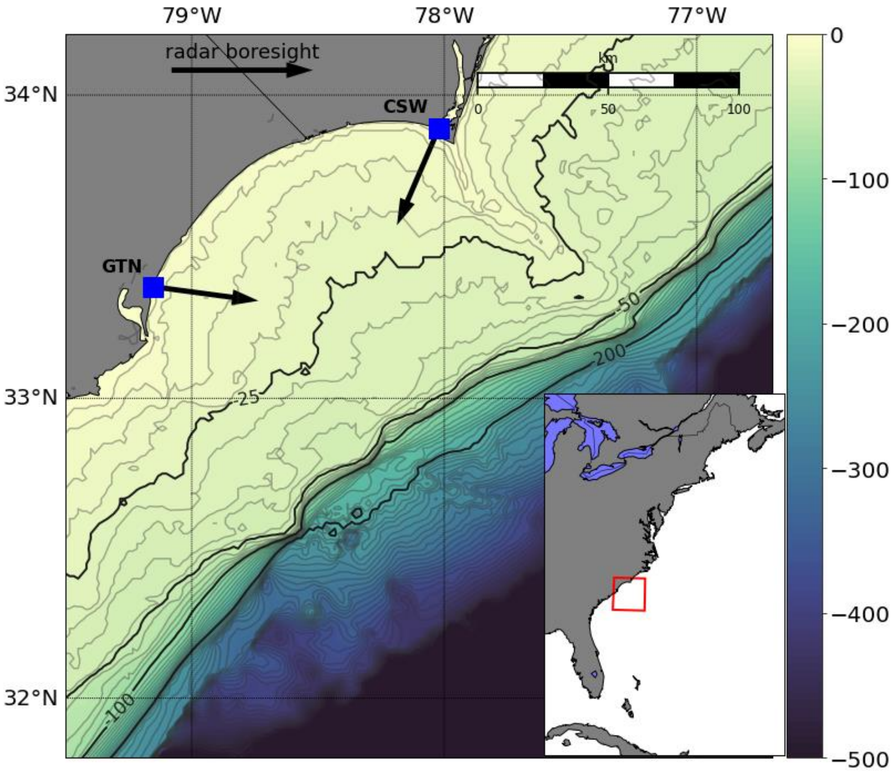

Figure 4.1: Site overview of Long Bay SC. Its location on the east coast of the USA is shown in the inset. The locations of the HF radar sites are shown as blue squares and the direction of the boresights indicated by the black arrows.

4.3 Methods

4.3.1 Eddy

The winding-angle method is perhaps the most straightforward approach to identify eddies. Given a vector field (such as the surface currents measured over Long Bay SC on July 10, 2013, see figure 2a), virtual particles are released and their paths they would take in the vector field are calculated; these are known as instantaneous streamlines (figure 2b). Each streamline is made up of many small segments (figure 2c); the winding-angle is calculated by summing the angle at each vertex $(\theta_1 + \theta_2 + \cdots)$. If the total winding-angle the streamline makes is at least $360°$, and after this $360°$ the streamline is not too far from its starting position (maximum distance d_s), this signifies an eddy (Sadarjoen and Post, 2000). Streamlines (figure 2b) meeting these criteria for the vector field in figure 2a are marked in magenta in figure 2d. Here, we loosen the restrictions to a minimum winding-angle of $270°$. The maximum distance allowed between the starting and ending position of the streamline is 5 km.

Following notation in Sadarjoen and Post (2000), the total number of points on streamline i is given by $|S_i|$. Therefore, the points on streamline i are given by $P_{i,j}$ where $j = 1 \ldots |S_i|$. The streamline center $\left(\overline{S_{i_i}}\right)$ is calculated (eq. 1) as the average position of all points that make up the streamline (streamline centers are shown as red squares in figure 2d). Any streamline center which is close to another streamline center (maximum distance d_C) is considered to represent the same eddy. All the streamlines that make up a single eddy form what is called a cluster ($C_k = \{S_{i,l}\}$ where $l = 1 \ldots |C_k|$). The center of the cluster (black 'x' in figure 2d, $\overline{C_k}$) is calculated as the average of all streamline centers (eq. 2). After this process, all streamlines that represent eddies have been identified and clustered into separate eddies.

The next step is to identify the properties of each eddy. Following Sadarjoen and Post (2000), for each cluster k, the covariance (M_k) of all the points making up the streamlines of that cluster is used to approximate the shape and size of the eddy. The eddy shape is estimated as an ellipse with axis lengths equal to the eigenvalues of M_k and axis directions along the eigenvectors of M_k.

$$\bar{S_i} = \frac{1}{|S_i|} \sum_{j=1}^{|S_i|} P_{i,j} \tag{4.1}$$

$$\overline{C_k} = \frac{1}{|C_k|} \sum_{l=1}^{|C_k|} \bar{S}_{k,l} \tag{4.2}$$

The winding-angle method was developed using model data (Sadarjoen and Post, 2000) and we found that for HF radar data, we need to optimize the three parameters; the minimum winding-angle, the maximum distance between the start and ending of a streamline (d_S), and the maximum distance between streamline centers to be considered the same eddy (d_C). The minimum winding-angle was loosened to $270°$, and we allow the distance between start and ending of the streamline to be almost twice the size of our 3x3 km grid; $d_S = 5$ km. The distance between streamline centers that represent the same eddy that performed best was quite large, $d_C = 10$ km.

Once eddies have been identified in each low passed HF radar vector current estimate (1/2 hourly data sets), tracking eddies through time is performed following the method described in Sadarjoen and Post (2000). For each eddy, if in the previous radar acquisition there was an eddy with its center close to this eddy's center (maximum distance d_T), it is considered to be a continuation of the same eddy. Due to noise and data availability in the HF radar data set, we loosen the previous radar acquisition requirement to be within 2 hours of the current radar acquisition. Additionally, the maximum distance to the previous eddy center, $d_T = 10$ km, is larger than the expected distance an eddy will travel in this 2 hour time period but performs better than when using smaller values of d_T.

We note here that the large eddy further offshore, visible in the instantaneous streamlines in figure 2b, see the black 'x' in figure 2d, is the Charleston Gyre. However, the spotty HF radar data results in almost no closed streamlines (see figure 2b), and therefore this feature, although detected, consists of only a single closed streamline that satisfies the winding-angle criteria. This results in the unrealistic size and shape seen in figure 2d. Optimization techniques to fill in spotty HF radar data is not easily available, since the offshore boundary is the fast moving Gulf Stream and not a coastline where the velocity can be assumed to go to zero (i.e., we cannot use the optimal interpolation method which has been shown to be successful in other HF radar coverage areas (see Kim et al., 2008)). This difficulty is apparent in the data shown here, and we suggest that longer range HF radar systems are deployed in this area or the radar systems currently deployed here operate continuously (which may require some new hardware) so that hourly or longer averages can also be used to provide longer range surface current estimates thereby providing higher data availability over this area.

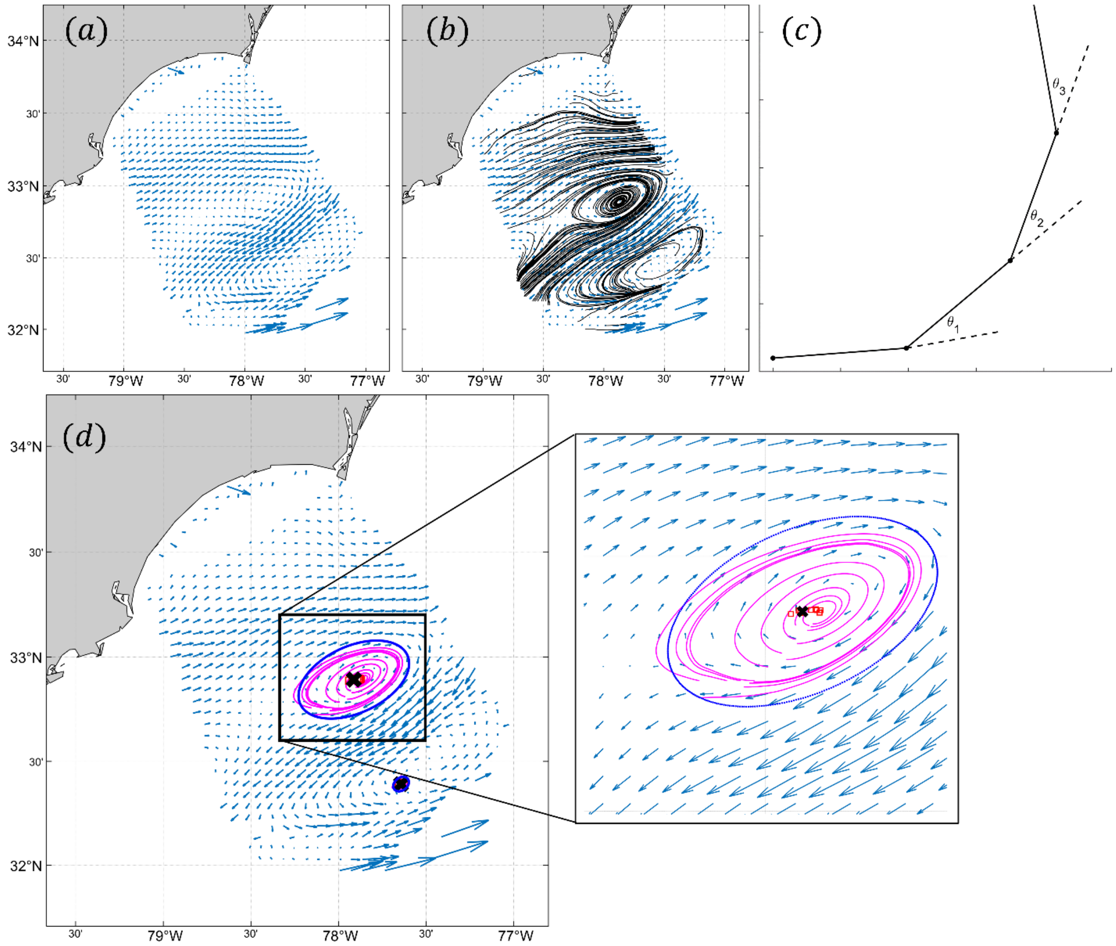

Figure 4.2: (a) HF radar low pass filtered surface currents on July 10, 2013 at 14:30 UTM. (b) Instantaneous streamlines calculated for the surface currents in (a). (c) Diagram of the winding-angle calculation for each streamline. (d) Streamlines that meet the winding-angle criteria are colored in magenta; their centers are marked as red squares, the center of all the streamlines that make up the eddies are shown as black ‘x’’s and the size of the eddies are shown as the blue ellipses (see inset for more details).

4.3.2 Momentum Flux

To calculate momentum flux $< u' \cdot v' >$ across the shelf break, first the u, v HF radar surface currents are rotated to a reference frame where the u component is directed offshore and the v component downstream (towards the Northeast). The isobath direction at the shelf break in Long Bay, SC, at the 100 m isobath is $56°$ N, shown as the red arrow in figure 3. As in Lee et al. (1991), positive flux is in the direction from the shelf to the Gulf Stream, while negative flux is from the Gulf Stream to the shelf. Positive momentum flux signifies that momentum is leaving the shelf towards the GS, which potentially contributes to momentum being added to the GS , thereby possibly accelerating the GS as it travels across Long Bay.

We should note here that this momentum flux across the shelf break (near the 100 meter isobath) may be due to other factors, i.e., winds/tides and that the momentum flux may not be coming directly to or from the GS. Ideally, the entire GS would be covered by longer range HF radar systems which would allow significantly more detailed momentum flux calculations to or from the GS.

To ensure high accuracy and high data availability of HF radar currents, we limit the area of the shelf break where momentum flux is calculated to where both radar sites have a 'look direction' of less than $30°$ from their boresights (these limits are shown as black arrows in figure 3). Therefore, the momentum flux is calculated along the roughly 40 km long section of shelf break near the 100 m isobath, marked by the red arrow, from $78.28\text{ W}, 32.78°$ N to $77.90\text{ W}, 32.99°$ N.

After the coordinate system is rotated by $56°$ N, the current (u, v) can be defined as the mean current $(\bar{u}, \bar{v})$ plus the variability (u', v'), from which the momentum flux $< u' \cdot v' >$ is calculated. Here, we use yearly averages $(\bar{u}, \bar{v})$ for yearly momentum flux (e.g., figure 11) and monthly averages $(\bar{u}, \bar{v})$ for the for monthly momentum flux (e.g., figure 12).

$$u = \bar{u} + v'$$

$$v = \bar{v} + v'$$

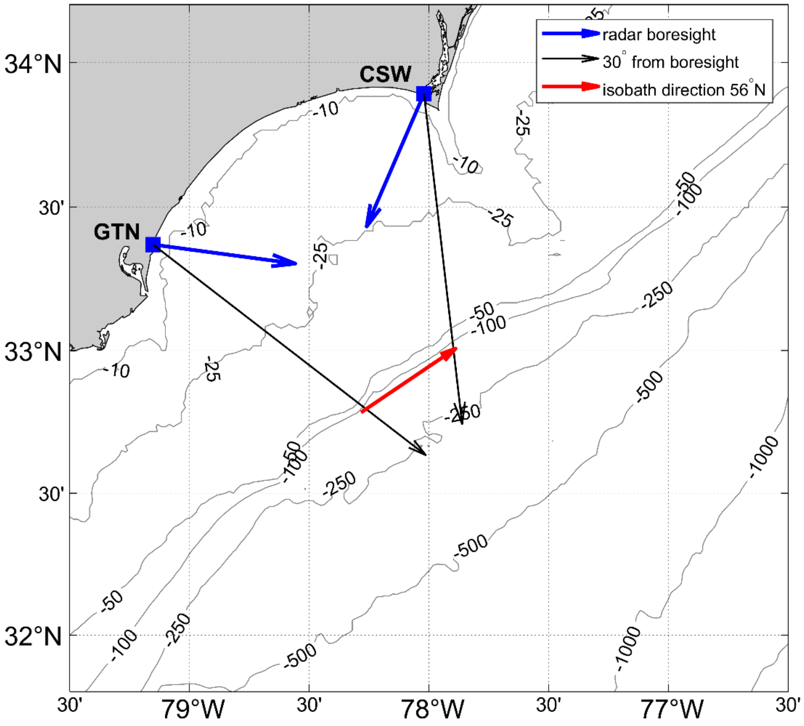

Figure 4.3: Site overview as in figure 1. Black arrows show the 30° look direction from the radar boresights. The red arrow (roughly 40 km in length) shows the isobath direction of 56° N near the shelf break where both radar sites have less than a than 30° look direction from their boresights.

4.4 Results

4.4.1 Charleston Gyre and Gulf Stream

The HF radar vector current data availability after QA/QC for 2013 is shown in figure 4a. The 75% contour (inner dashed white line) includes the shelf break between the HF radar sites, while the 50% contour (dashed black line) extends just past the 250m isobath, and the 25% contour (outer dashed white line) almost reaches the 500 m isobath. The mean yearly currents (figure 4b) show the prominent Charleston Gyre, similar to Lee et al.'s (1991) description of the current in this area, while the GS is further offshore with mean currents > 1m/s (figure 4b). The slight decrease in currents furthest offshore is likely to be an anomaly due to the very low data availability at the edge of the HF radar measurement area. While the mean yearly wind is close to zero (figure 4d), the variance of the wind is large (figure 4d). A Windrose of the winds during the year show predominantly along-shelf winds (see figure 4c) with wind speeds between 5-15 m/s the majority of the time.

The Gulf Stream in this area, just downstream of the Charleston Bump, is known to be either highly deflected or slightly deflected (Bane and Dewar, 1988). The variation in the position of the GS between monthly means in the HF radar data set is significant, for example, in October the GS is deflected so far offshore it is not covered by the HF radar range (see 2013/11 in figure 5). On the other hand, in July and September the GS is slightly deflected with current speeds of 1 m/s just offshore of the 100 m isobath (see figure 5).

While the CG is clearly visible in the yearly mean, there is significant variability in the monthly mean HF radar currents (see figure 5). In February and March, the CG is not visible in the data set at all. In August and December, the center of the CG is much further downstream than in the yearly mean. There is also significant variability in the offshore location, depending on the deflection of the GS. In November, the GS is highly deflected offshore, and the center of the CG is much further offshore than in the yearly mean (figure 4b), while in October the GS is slightly deflected and the center of the CG is further inshore than in the yearly mean.

Although the wind is not believed to control the deflection of the GS, the wind may play a role in the development of the Charleston Gyre (CG). The mean monthly winds and wind variances are shown in the inset in figure 5 (the direction of the arrow shows the direction the wind is blowing to). The Charleston Gyre is completely absent in March, the month with the strongest mean wind blowing to the east. The month with the second strongest mean wind blowing towards the east is February in which the CG is mostly absent, although there is some variable current in the general vicinity of where the CG is expected to be. In July the wind is to the north and coincides with the CG located far inshore while in November the winds are towards the south and coincides with the CG located far offshore; however, the deflection state of the GS controls where the CG may appear and it is difficult to say what effect the winds have in these two months. A longer term study over several years or a decade may be able to tease apart the effect of the wind on the position of the CG, for example, if several months have the same GS deflection but different mean wind velocities, it may be possible to separate the effect of the wind from that of the deflection mode of the GS.

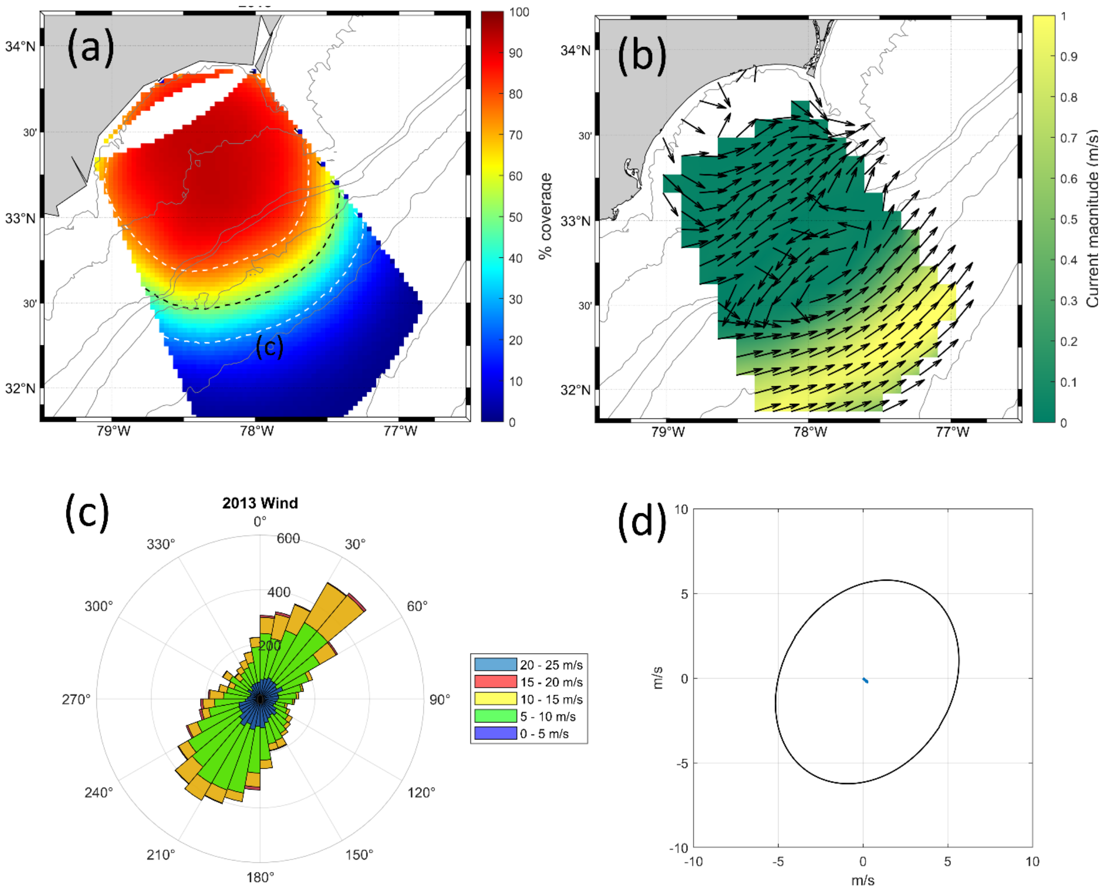

Figure 4.4: (a) HF radar vector surface current data availability for 2013. (b) 2013 mean HF radar surface currents. The 10, 25, 50, 100, 250, 500, and 1000 m isobaths are shown as gray lines (same isobaths as in figure 3). (c) Windrose for winds measured at NDBC buoy 41013 over year 2013. (d) Mean wind for 2013 shown as the blue arrow (the direction the wind is blowing towards) while the black ellipse shows the variance of the winds over 2013.

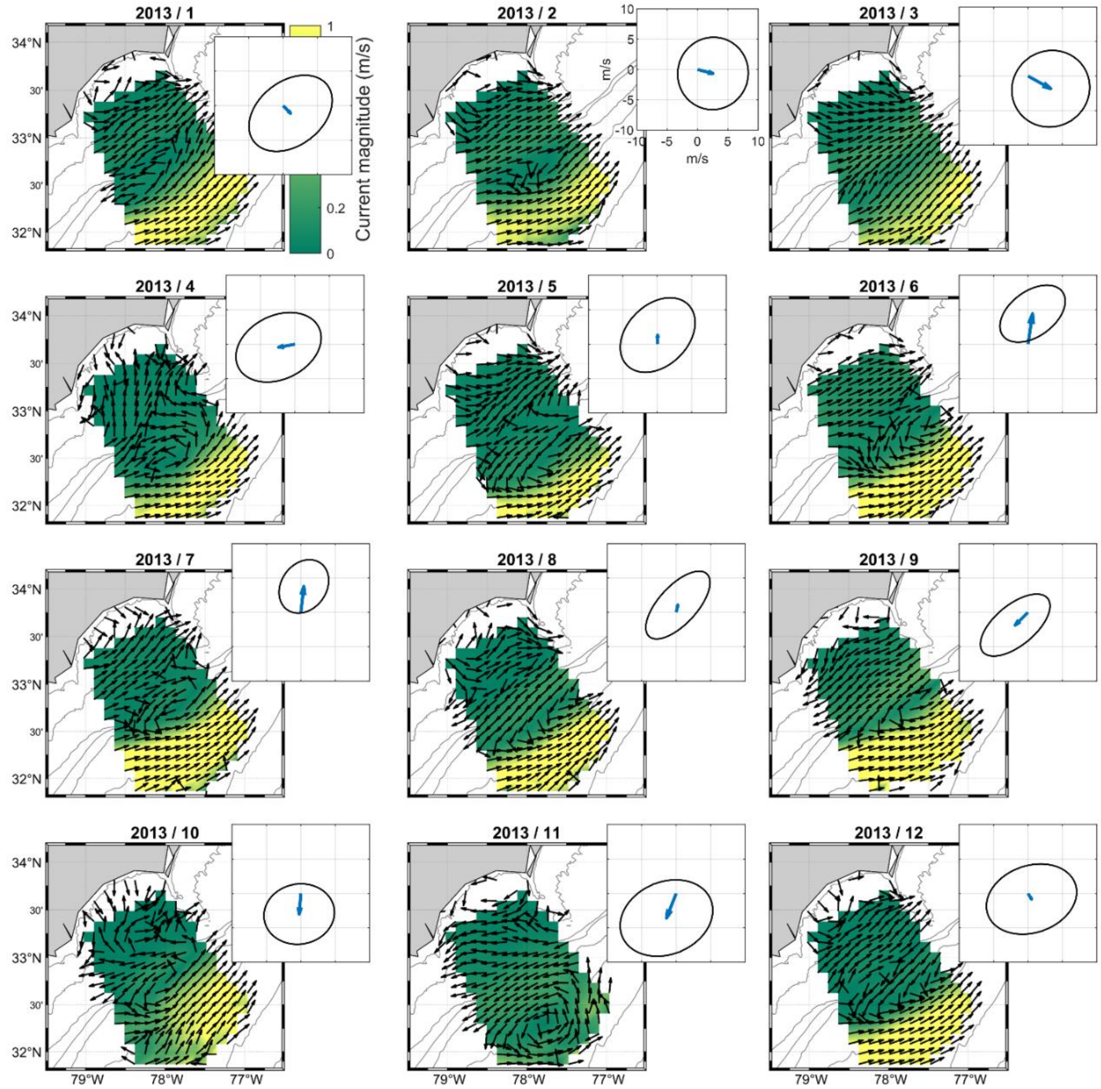

Figure 4.5: HF radar monthly mean currents for 2013. The 10, 25, 50, 100, 250, 500, and 1000 m isobaths are shown as gray lines (same isobaths as in figure 3).The monthly winds are shown in the insets, where the mean wind is shown as the blue arrow (the direction the wind is blowing towards) and the ellipse shows the variance of the wind.

4.4.2 Eddy identification: Charleston Gyre

Eddy identification was performed as described in section 3.1 using the low pass filtered (subtidal) HF radar vector currents. The eddies detected include nearshore small eddies and also the larger semi-permanent CG. Although over 1000 eddies were identified, most were short lived (< 6 hours). A histogram of eddies tracked for 6 or more hours is shown in figure 6. A total of 296 eddies were tracked for at least 6 hours, with most (227) of these eddies tracked for under 24 hours. However, 17 were tracked for more than 48 hours and the longest for 100.5 hours, a little over 4 days. Since data availability falls off steeply after the shelf break (figure 4a), the duration of the eddies may in fact be much longer than the results (figure 6) suggest. Specifically, although the CG is semi-permanent and may be expected to be detected by the winding-angle method for weeks at a time, the lower data availability past the shelf break results in the longest duration the CG was detected to be 100.5 hours.

Of the 17 eddies tracked for more than 48 hours, all but 1 were indicative of the CG. Size and shape of the detected eddies are not given herein due to the fact that optimization techniques using the winding angle method are different for smaller eddies (e.g., 5km diameter) and the much larger CG (e.g., 50+ km diameter). This is due to the fact that the CG, at times, exhibits significant convergence/divergence which results in the instantaneous streamlines ending positions to be significantly far from their starting positions, which in addition to the lack of data availability offshore results in few closed streamlines around the CG (see figure 2d). If we optimize this method for the CG, we also create a large amount of false positives in other areas that have significant vorticity but do not contain actual eddies. This problem may be addressed well by neural network eddy identification methods that can be trained to identify eddy features and are malleable enough to account for differing sizes more easily than hard coding an algorithm such as the winding-angle method to account for this large variation in eddy sizes and shapes.

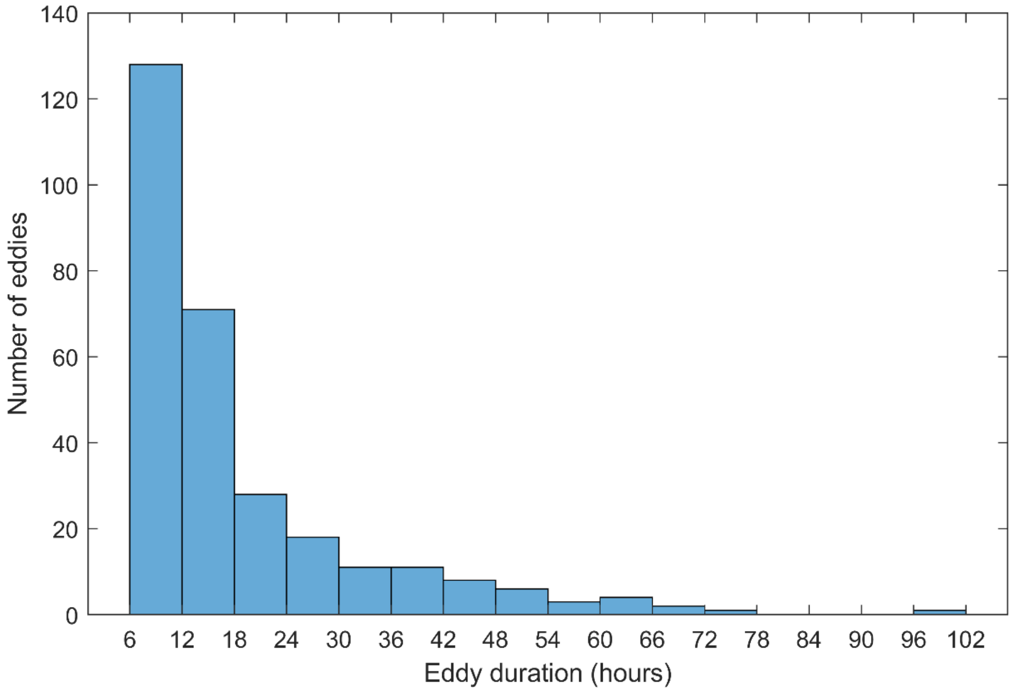

Figure 4.6: Histogram of eddy duration (amount of time tracked in the HF radar currents) for eddies lasting longer than 6 hours in the HF radar surface currents for 2013.

The longest cyclonic eddy was tracked for 74.5 hours, just over 3 days and is clearly the CG (figure 7). It was first identified on Jan 1, 5:30 UTM (see figure 7a) and the last HF radar acquisition it was identified in was on Jan 4, 8:00 UTM (see figure 7b). As the CG travelled downstream, it grew significantly in size and its shape became a much wider ellipse, stretched in the along-stream direction (compare figure 7a/b). As it travelled downstream, it covered a straight line distance of roughly 60 km in 74.5 hours, resulting in an average speed of 0.2 m/s. This speed is roughly an order of magnitude lower than the Gulf Stream current. Although the CG does travel downstream here (figure 7), it is propagating far slower than the GS. The offshore side of the CG has current velocities over 1 m/s (downstream) while the inshore side has velocities ~0.5 m/s upstream, signifying the speed of the CG is not simply due to the shear between these offshore and inshore flows. Additionally, the downstream offshore velocity of the GS is always greater than the inshore side of the CG that flows upstream, yet the CG is shown here to move in all directions (shown in figure 10 and discussed further below).

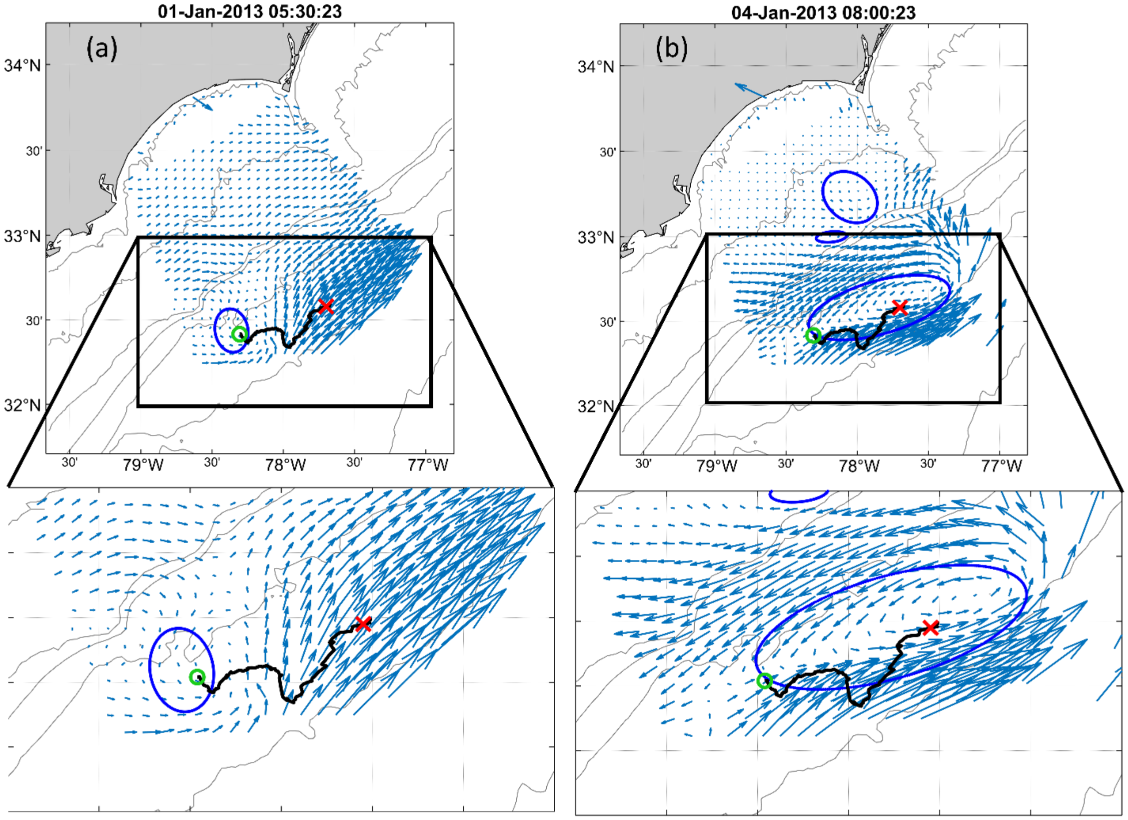

Figure 4.7: The path of the cyclonic eddy is shown as the black line with the starting position shown as the green circle and the ending position as the red ‘x’. The shape of eddies identified using the winding angle method are shown as the blue ellipses. (a) The first HF radar acquisition where this eddy was identified. (b) The last HF radar acquisition where this eddy was identified. See insets for more details. The 10, 25, 50, 100, 250, 500, and 1000 m isobaths are shown as gray lines (same isobaths as in figure 3).

The paths the eddies that were tracked for at least 48 hours are shown as arrows from their starting to ending position in figure 8. The blue arrows represent the CG which is a cyclonic (upwelling) eddy feature, while the red arrow represents an anticyclonic (downwelling) eddy. Although most of the time the CG is detected (blue arrows), it propagates downstream, other times it does not move much at all over the time it was tracked for (48+ hours). Additionally, there is a blue (CG) track moving onshore instead of downstream, and one track moving upstream instead of downstream, showing the CG can propagate in any direction. Additionally, the CG (blue arrows) moves slowly, with speeds of 0.2 m/s or less, showing the semi-permanent nature of the CG and that the CG does not always propagate with the flow of the Gulf Stream. The anticyclonic eddy (red arrow) is near the shelf break and is the longest lived and furthest offshore of the anticyclonic shelf break eddies which are discussed in further detail below.

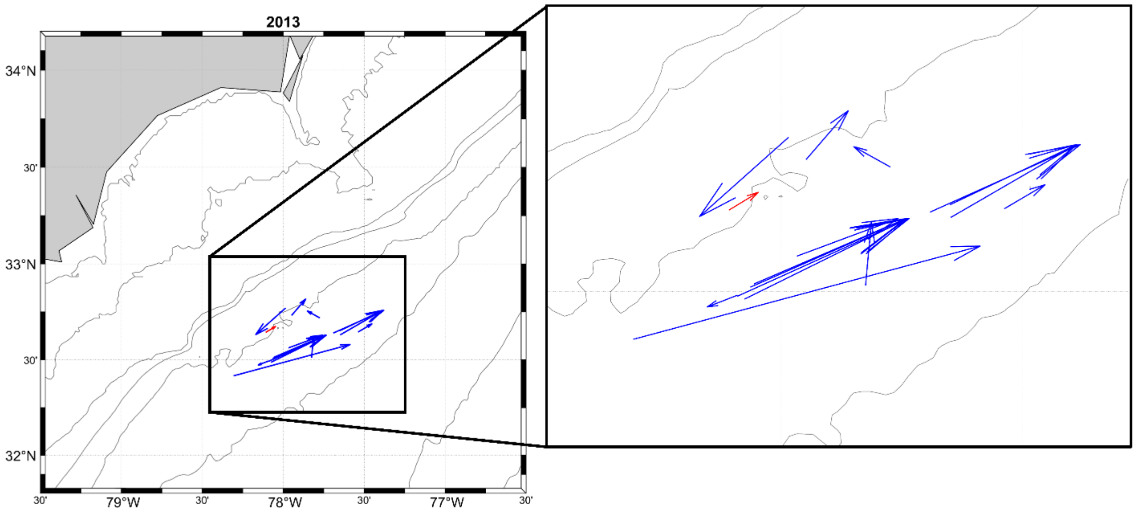

Figure 4.8: Eddies tracked for over 48 hours where blue arrows represent cyclonic (upwelling) eddies and red arrows represent anticyclonic (downwelling) eddies. The arrows are drawn from the starting and ending position of the eddies identified. The 10, 25, 50, 100, 250, 500, and 1000 m isobaths are shown as gray lines (same isobaths as in figure 3).

4.4.3 Eddy identification: Overview

The paths of all eddies tracked for at least 6 hours are shown in figure 9a. As in figure 8, the blue and red arrows represent cyclonic (upwelling) and anticyclonic (downwelling) eddies, respectively while the start and end points of the arrows themselves connect the starting to ending position of the eddy identified. Offshore the CG is detected as a cyclonic eddy, between the 250 and 500 m isobaths. Near the shelf break, most of the eddies are anticyclonic (red arrows) and travel upstream (towards the west-southwest), both just offshore and onshore of the shelf break at the 100 m isobath. These shelf break eddies travel equatorward similar to the shelf break eddies found by Savidge et al. (2010), except, they are anticyclonic and not related to tidal flows as the analysis presented in here uses subtidal currents only. Further inshore (between the 25 and 50 m isobath) both cyclonic and anticyclonic eddies are identified with large variability in direction. We are most interested in the anticyclonic eddies near the shelf break, as they are likely a significant driver of cross shelf momentum flux, as found in Savidge et al. (2010). However, before we discuss the eddies near the shelf break, it is more appropriate to first discuss the momentum flux across the shelf break.

4.4.4 Momentum flux and shelf break eddies

The mean yearly momentum flux (see section 3.2 for calculation details) along the shelf break (black line in figure 9a) is shown in figure 9b. The flux is consistently near 100 $\mathrm{cm}^2\ \mathrm{s}^{-2}$, with little variability along the roughly 40 km section of the shelf break where it is calculated. Although the momentum flux shows little along shelf variability for the yearly mean, there is significant monthly variation (figure 10). In April, July and October, the flux is close to or below 0, while in May and August the flux is consistently above the yearly mean of 100 $\mathrm{cm}^2\ \mathrm{s}^{-2}$. There is also significant along shelf variation of the momentum flux in the months of January, March, and September.

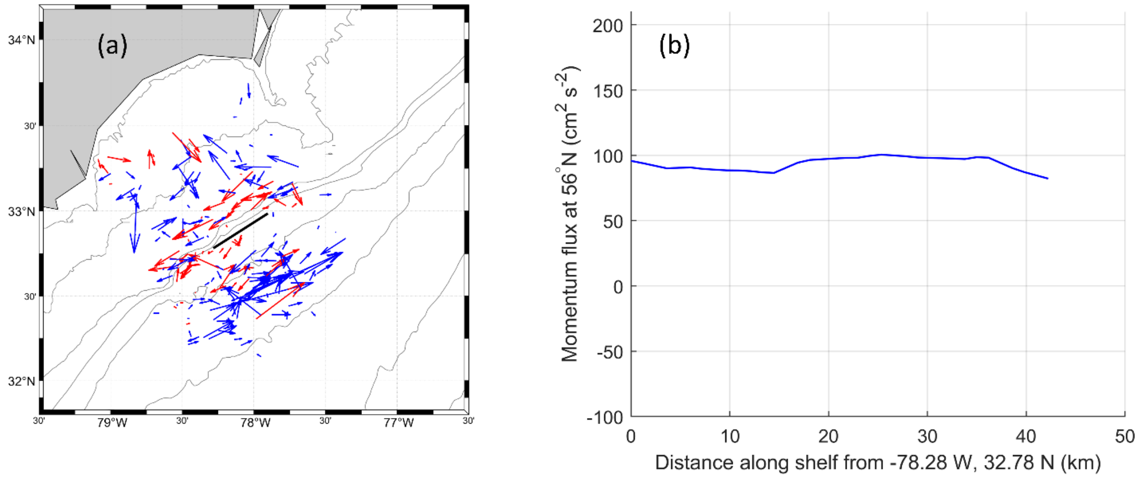

Figure 4.9: (a) Paths for eddies lasting 6 hours or more, where the red (anticyclonic) and blue (cyclonic) arrows are drawn from the starting and ending position of the eddies (as in figure 8). The 10, 25, 50, 100, 250, 500, and 1000 m isobaths are shown as gray lines (same isobaths as in figure 3). (b) Mean momentum flux across the shelf break (marked as the black line in (a)) in Long Bay, SC in 2013. The black and green box in (a) signifies the area where shelf break eddies are counted.

Momentum flux is also calculated for the entire HF radar coverage area (see figure 11). We note however, that the 56° N rotation is only applicable at the shelf break marked as the black line in figure 11a; the shelf break is curved and has a different orientation both southwestwards and northeastwards. The momentum flux changes rapidly towards these edges of the shelf break, however, the HF radar may have less accurate surface current estimates at these locations since the they are more than 30° from the radar boresights (see figure 3). There are, however, striking features, such as in March and December, there is a small area of increased flux at shelf break. In January, February, September, and November there is a filament like feature of flux intruding from the western edge of the shelf break. In August, there is significant momentum flux across the majority of the shelf break and inner shelf.

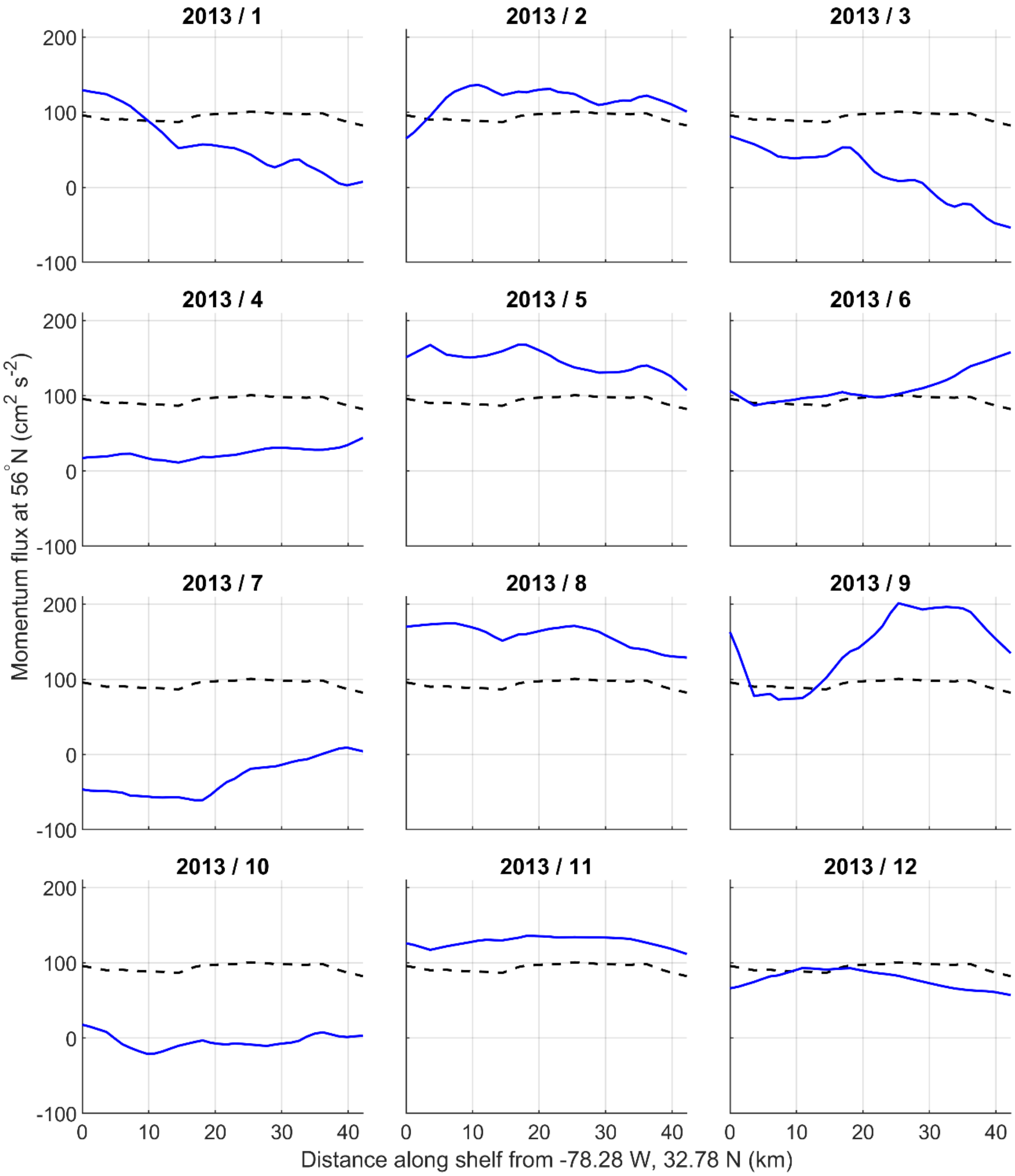

Figure 4.10: Momentum flux (monthly mean in blue, 2013 mean in dashed black) across the shelf break in Long Bay, SC.

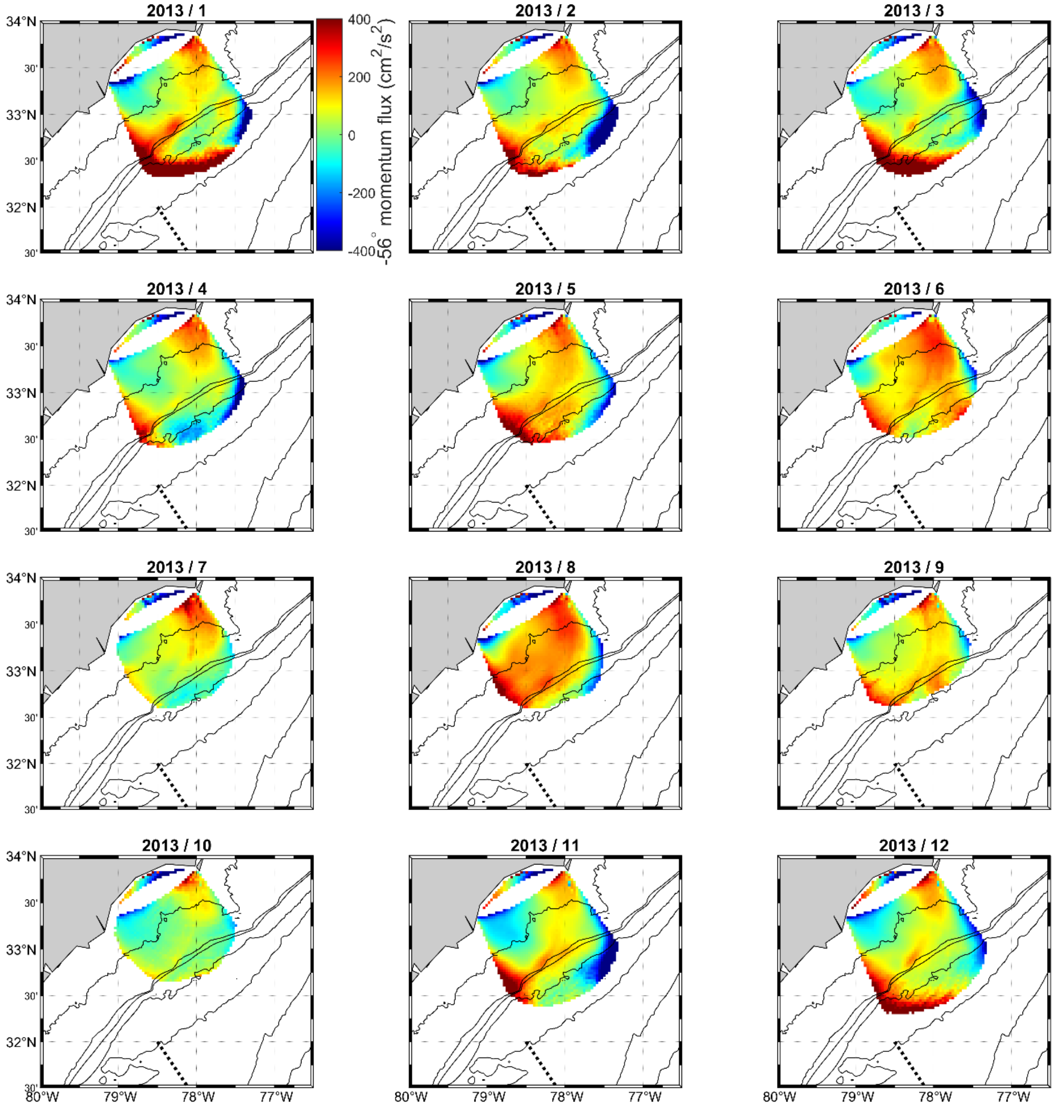

Figure 4.11: Monthly momentum flux (where the coordinate system has been rotated by 56° N) up to 50% HF radar data availability. The 10, 25, 50, 100, 250, 500, and 1000 m isobaths are shown as gray lines (same isobaths as in figure 3).

The eddy kinetic energy (EKE: defined as $\sqrt{u'^2 + v'^2}$) has similar features to the momentum flux and is shown in figure 12. In both March and December there is a small area on the shelf break of increased EKE. In January, September and November there are also filaments of EKE intruding towards the shelf break, however unlike the momentum flux (figure 13), the EKE does not show a strong filament in February near the shelf break. Additionally, in August, the EKE is generally low across the inner shelf and shelf break, in opposition to the momentum flux (compare figure 2013/8 in figures 11 and 12).

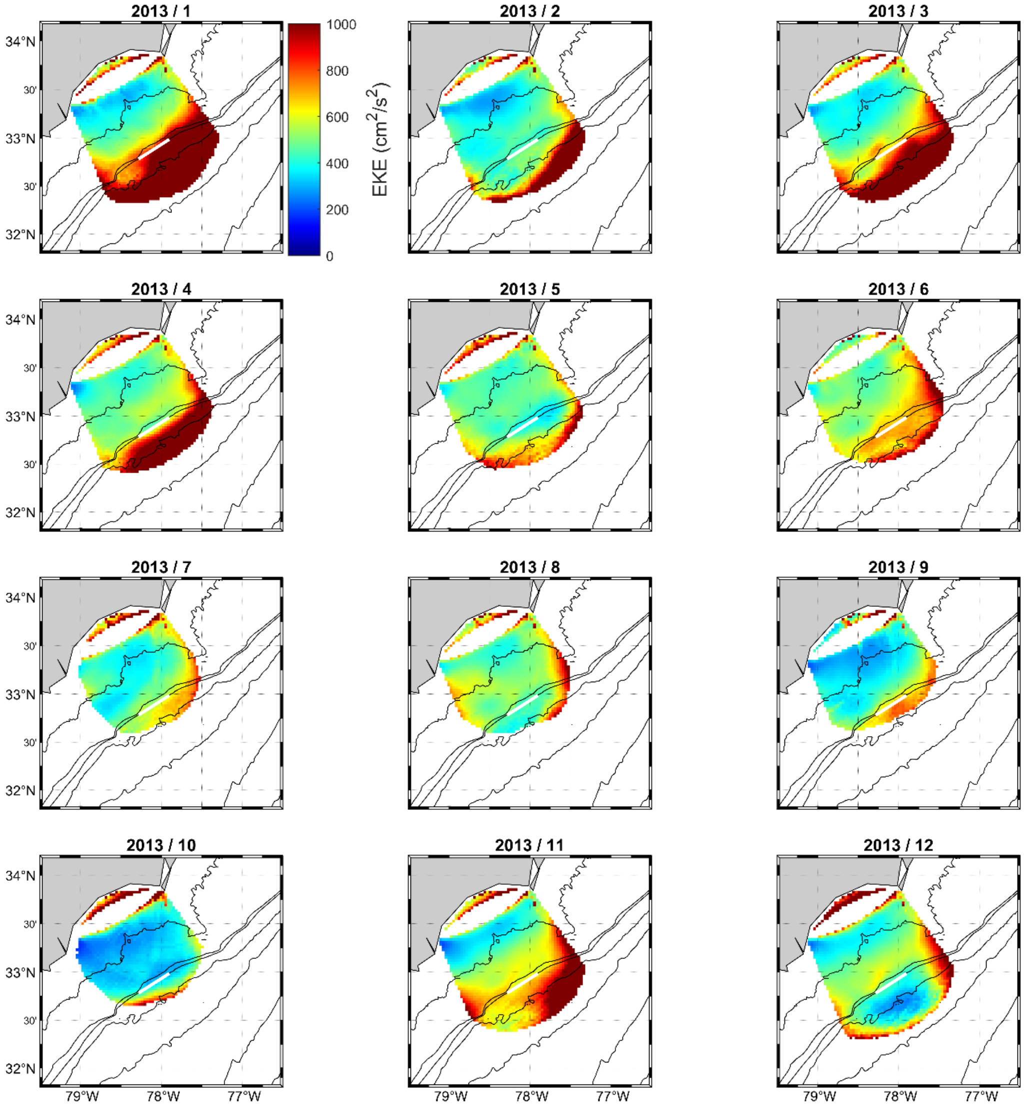

Figure 4.12: Monthly eddy kinetic energy calculated up to the 50% HF radar data availability contours. The 10, 25, 50, 100, 250, 500, and 1000 m isobaths are shown as gray lines (same isobaths as in figure 3).

The number of eddies identified between months also has significant variability (figure 13). At the shelf break where the momentum flux is calculated (black line in figure 13), there are several anticyclonic eddies (shown in red) in February, May and August, and in June at the downstream limit of momentum flux calculations. There is some correlation here, February, May and August all have more than the yearly average flux to the GS, and in June, there is more flux at the downstream side than the upstream (figure 10), which is where an anticyclonic eddy is identified (see red track in June in figure 13). In April, July and October, there are few anticyclonic eddies close to where the momentum flux is calculated, although in April there an anticyclonic eddy nearby the downstream side of the shelf break (figure 13). These months have the lowest momentum flux (figure 10), and in April, there is an increase in momentum flux on the downstream side of the shelf break, where the anticyclonic eddy was identified.

A closer examination of an anticyclonic eddy near the shelf break in early January is shown in figure 14a-c. This eddy was first identified on Jan 4 6:30 UTM (figure 14a) and as it travelled upstream (equatorward) it grew in size. Around Jan 4 23:00 (figure 14b) it became more stationary and lasted into the afternoon of Jan 5 (figure 14c). The along-shelf position of this eddy is shown as the black line in figure 14d. The low pass filtered (subtidal) momentum flux across the shelf break between Jan 2 and Jan 6 (figure 14d) shows a strong band of positive momentum flux (off the shelf) coinciding with the position of this anticyclonic eddy.

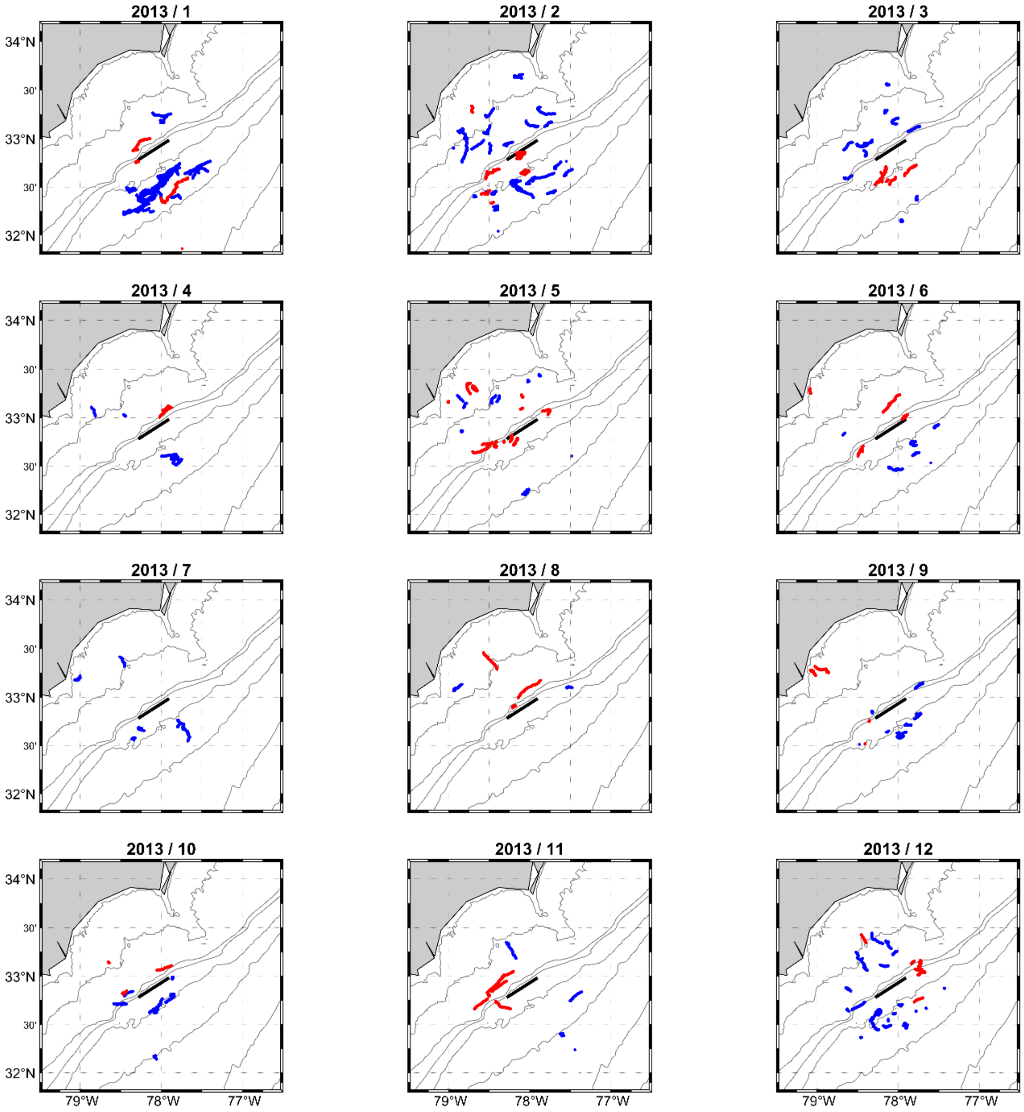

Figure 4.13: Monthly eddy paths for eddies lasting 6 hours or more, where the red (anticyclonic) and blue (cyclonic) lines are as in figure 7. The 10, 25, 50, 100, 250, 500, and 1000 m isobaths are shown as gray lines (same isobaths as in figure 3).

The monthly average momentum flux (averaged along the 40km length) is shown in red in figure 15a,b while the transport of the Florida current is shown in blue in figure 15a and the number of eddies identified within 10 km of the shelf break where momentum flux is calculated (see black and yellow box in figure 9a) is shown in blue in figure 15b. The variability of the momentum flux is correlated to the Florida current

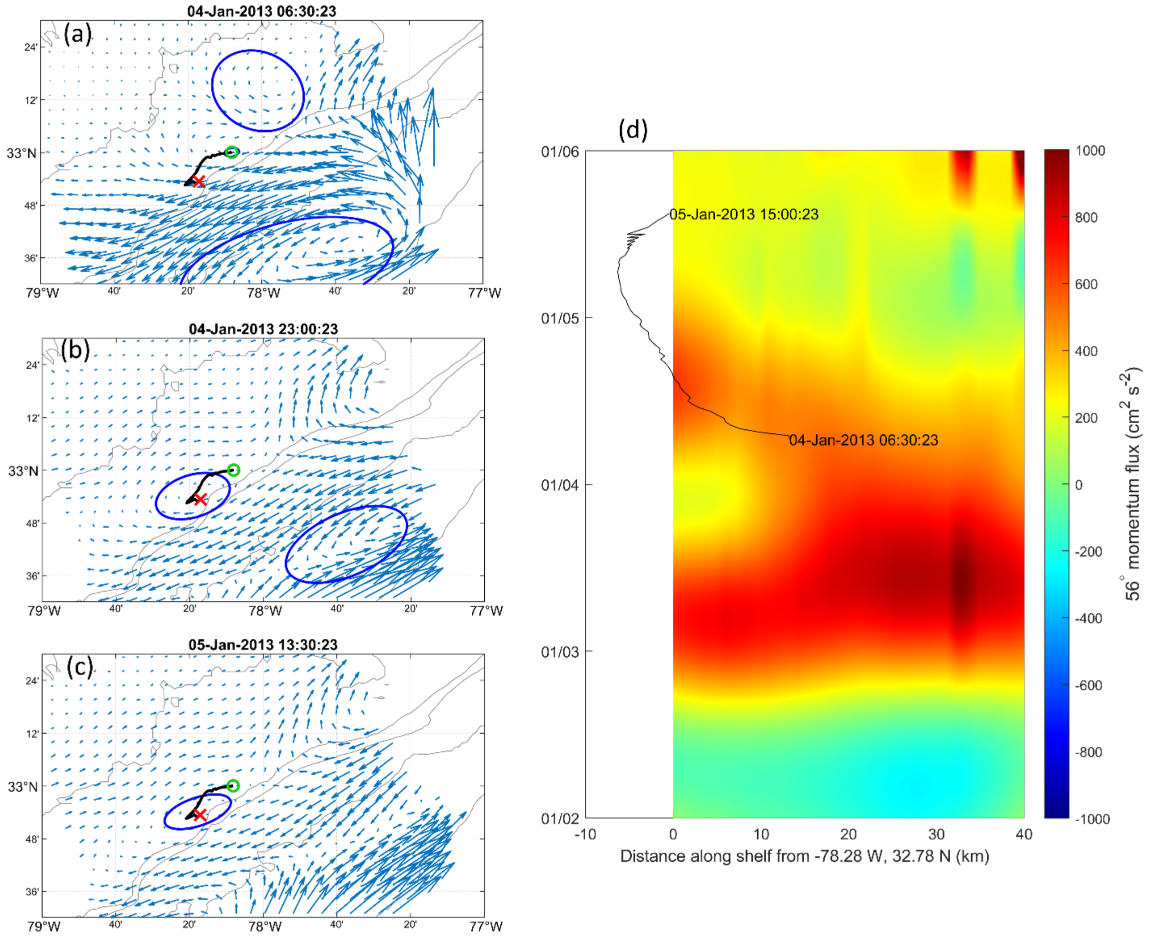

Figure 4.14: Anticyclonic eddy near the shelf break detected early Jan 4 (a) which moves upstream by the end of Jan 4 (b) and is stationary for the morning and early afternoon on Jan 5 (c). (d) Low pass filtered (subtidal) momentum flux across the shelf break is shown between Jan 2 and Jan 6, 2013. The along shelf position of the anticyclonic eddy in (a-c) is shown as the black line for the duration it was tracked for in the HF radar currents.

(measured by the submarine cable; data available at www.aoml.noaa.gov/phod/floridacurrent/) with $R^2 \approx 0.2$, signifying that majority of the variation in the momentum flux is not directly related to Florida current transport. Although this data is limited, a longer data series may increase or reduce the correlation between the two. For example, from August to January, they appear highly correlated, while between April and July the correlation appears much lower. The number the eddies identified within 10 km of the shelf break where momentum flux was calculated (red arrow in figure 3), correlates at a higher level, $R^2 \approx 0.4$. This signifies the importance of eddies in transferring momentum across the shelf break in this area.

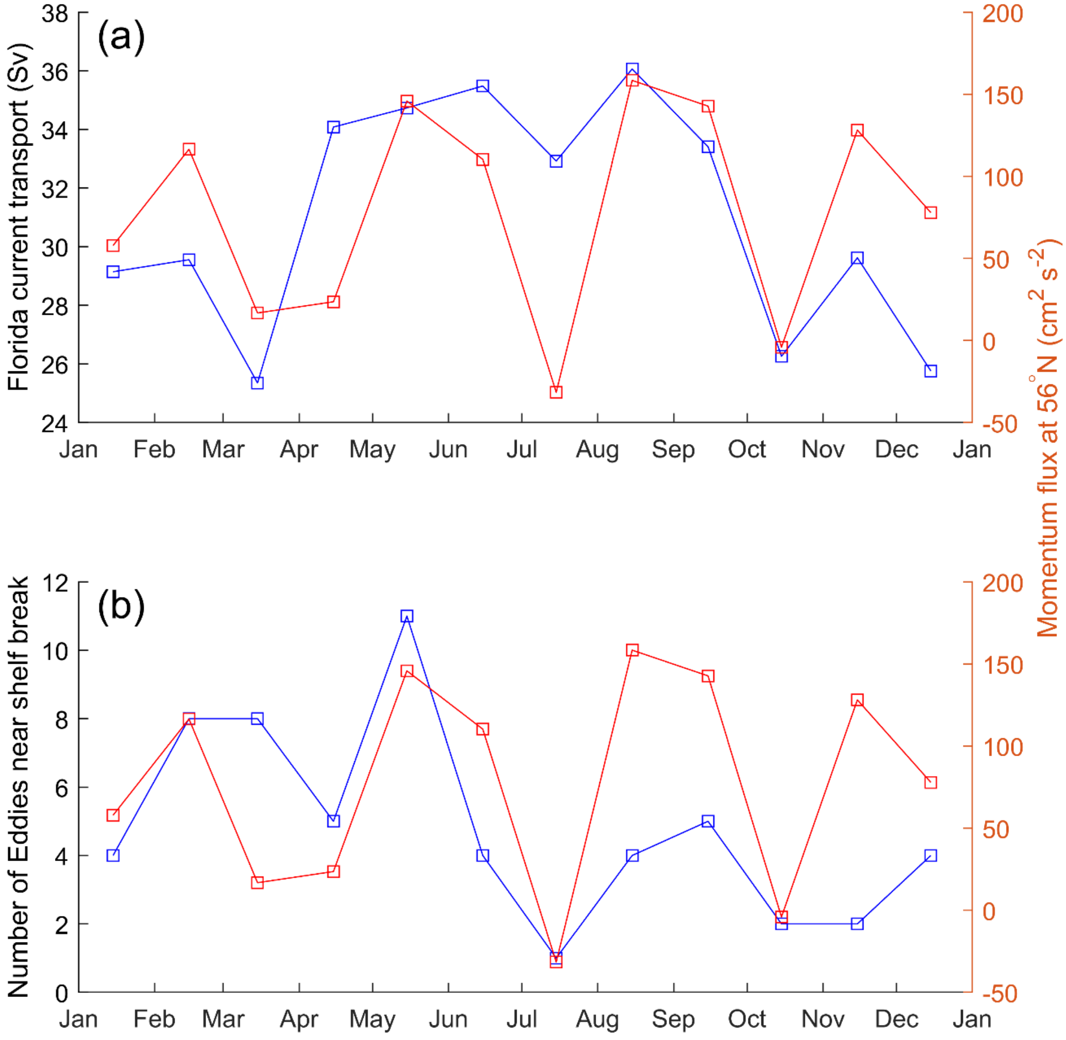

Figure 4.15: (a) Monthly averaged Florida Current time series in blue and mean monthly momentum flux across the shelf break in Long Bay, SC in red. (b) The number of eddies identified (per month) within 10 km of the shelf break where momentum flux is calculated in blue and mean monthly momentum flux across the shelf break in Long Bay, SC in red.

4.5 Discussion

Although our analysis suggests that momentum flux is correlated to eddy occurrence near the shelf break (figure 15a) and less correlated to the strength of the Florida Current (figure 15b), we do not think it is the excess of momentum flux that drives eddy formation, but rather it is the eddies that transport the momentum flux estimated (see figure 14). Here we assess both wind and tides during the times eddies are found near the shelf break. As before, we count the number of eddies within 10 km of the shelf break where momentum flux is calculated (see black and green box in figure 9a).

Tidal analysis (Pawlowicz et al., 2002) was performed on the vector HF radar currents for the HF radar coverage area. The M2 tidal constituent is the dominant tidal constituent in this area (Blanton, 2004) and is 5-10 times larger than N2 or K1, depending on the area of HF radar coverage. Therefore, we focus here on M2; a subset of the tidal ellipses for year 2013 are shown in figure 16a. The tidal amplitude falls off sharply after the shelf break. The tidal amplitude of the major axis on the shelf is roughly 0.25 m/s, which drops to 0.1 m/s at the shelf break and to 0.05 m/s just past the shelf break (see most offshore tidal ellipse in figure 16a). In order to evaluate monthly variability of the tides, the M2 tidal ellipse at a location near the shelf break (see black arrow in figure 16a) is estimated using monthly HF radar currents and the results are shown in figure 16b.

Although monthly tidal amplitude variation is insignificant (the major axis varies from 0.23 m/s to 0.25 m/s), the phase exhibits a higher variability. Using the monthly M2 tidal analysis (figure 16b), we identify the phase of the M2 tide when the shelf break eddies are first (figure 17a) and last (figure 17b) identified. The HF radar data availability is much higher in this area than further offshore where the CG is located and additionally, the shelf break eddies paths do not leave the HF radar coverage area (figure 9a). We assume that the first identification of the shelf break eddies is when they initially form and the last location of the eddy is when it dissipates. No correlation with the tides is found, in opposition to shelf break eddies found off the coast of Georgia (Savidge et al., 2010), although shorter lived shelf break eddies may not be apparent in the subtidal data set used here.

Although there seems to be little correlation to the tidal phase and the shelf break eddies, we show the winds measured at NDBC buoy 41013 during the first time the shelf break eddies are identified (figure 17c) and the winds at the last time the shelf break eddies are identified (figure 17d). While it is hard to see what drives the end/destruction of these eddies (figure 17d), there is an emerging pattern suggesting that shelf break

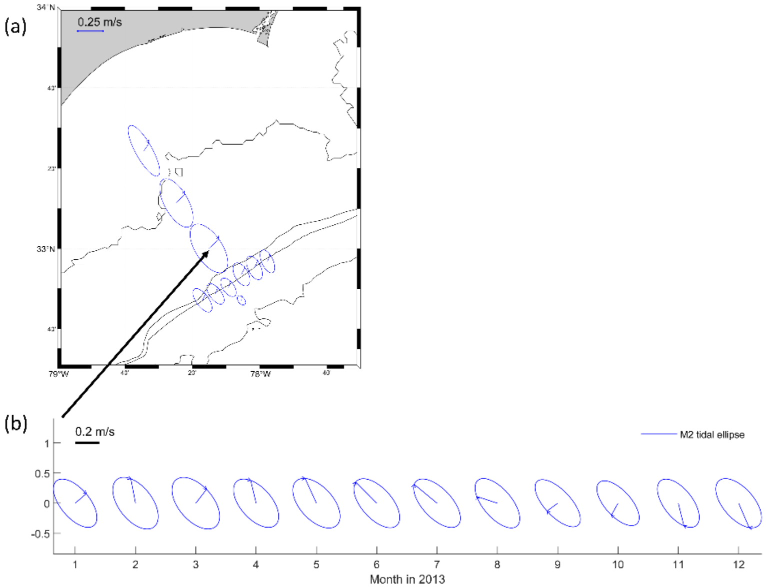

Figure 4.16: (a) Yearly tidal ellipses for M2 at select locations. (b) Monthly M2 tidal ellipses at the location marked in (a).

eddies get initiated (figure 17c) under northerly winds with speeds between 0-10 m/s. The northerly winds drive Ekman transport to the west, which is consistent with the direction of propagation of these shelf break eddies (see figure 9a).

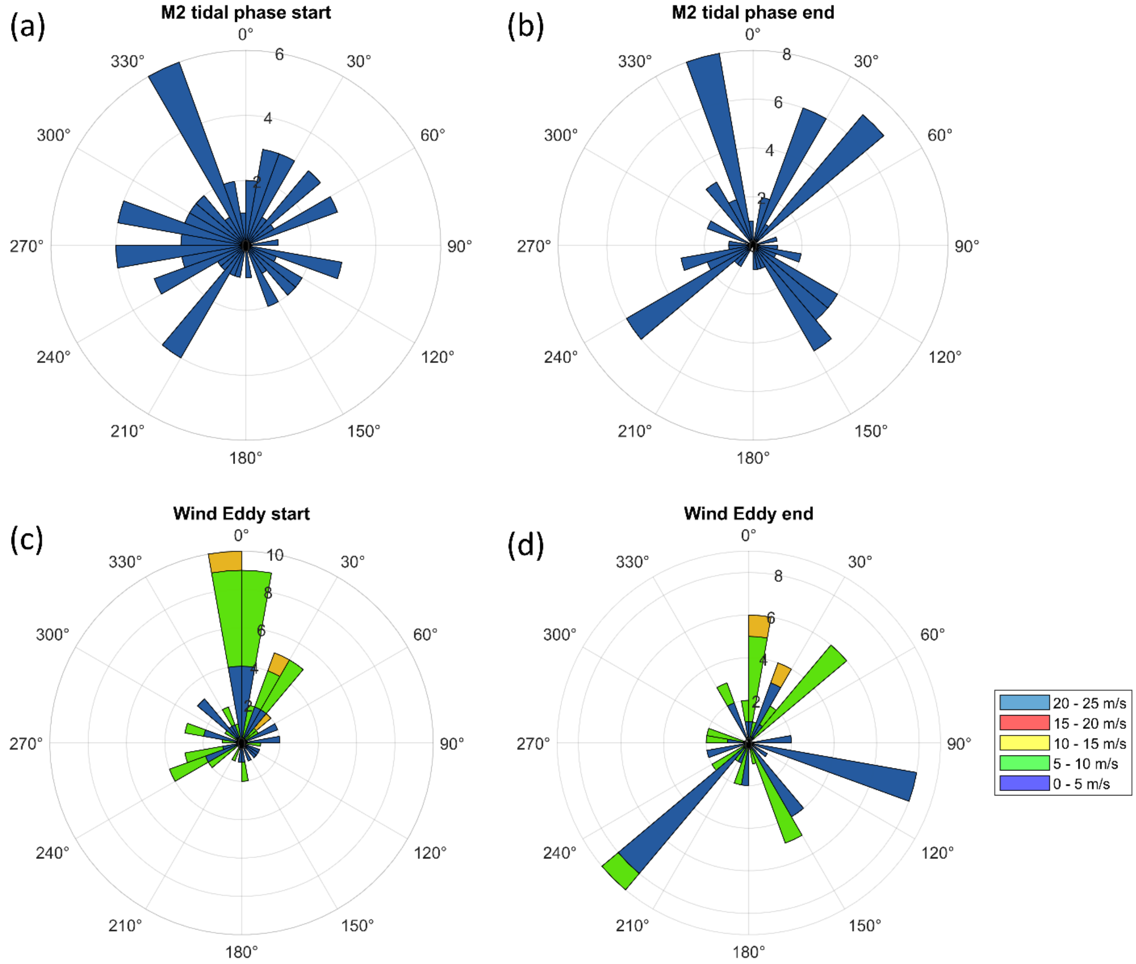

Figure 4.17: (a) Tidal phase for the starting position of eddies detected near the shelf break. (b) Tidal phase for the ending position of eddies detected near the shelf break. (c) Wind velocities for the starting position of eddies detected near the shelf break. (d) Wind velocities for the ending position of eddies detected near the shelf break. Eddies near the shelf break are limited to eddies within the black and green box in figure 11a.

4.6 Summary

In this study we have shown the potential of the winding-angle method to identify eddies within HF radar data. We optimized the parameters for noisy HF radar data (noisy in comparison to models) by loosening the winding-angle minimum to $270°$; the maximum distance between the streamline starting and ending position $d_S = 5$ km and the streamline clustering distance $d_C = 10$ km. For the HF radar data set covering 2013, over 1000 eddies were identified. Although most were short lived, 17 eddies were tracked for more than 2 days. Of these longer lived eddies (≥48 hr), all except for one were cyclonic (signifying the CG) and they were all located between the 200 and 500 m isobaths. Most of these propagated downstream with the GS, however some propagate onshore or upstream, showing that the CG can move in almost any direction but does have a preference to propagate downstream, at an order of magnitude slower speed than the GS.

Although there were only 17 eddies lasting more than 48 hours, over 200 lasted more than 6 hours. Near the shelf break, many anticyclonic eddies propagating upstream were identified. The momentum flux across the shelf break has variability that correlates to when and where these anticyclonic eddies are identified. During times when little to no anticyclonic eddies are detected near the shelf break, there is significantly less momentum flux across the shelf break. Additionally, the variability of momentum flux along shelf coincides with the position of the anticyclonic eddies and it is shown here that northerly winds between 0-10 m/s are the most common conditions when these shelf break eddies to form

The across shelf momentum flux measurement between $32.78°$ and $32.99°$ N near the 100 m isobath has a yearly average for 2013 of $100\ \mathrm{cm}^2\ \mathrm{s}^{-2}$, from the shelf to the GS. The variability within the year ranged from -50 to $200\ \mathrm{cm}^2\ \mathrm{s}^{-2}$. Lee et al.'s (1991) measurements were further offshore, near the 250 m isobath, measured at $32.5°$ and $33.5°$ N, with momentum flux of 50 – 370 and 115 – 413 $\mathrm{cm}^2\ \mathrm{s}^{-2}$, respectively. The yearly average found herein ($100\ \mathrm{cm}^2\ \mathrm{s}^{-2}$) lies within the range of values found at $32.5°$ N by Lee et al. (1991) but not at $33.5°$ N. The range of values found by Lee et al. (1991) do exceed the values found here, especially at $33.5°$ N. If more long range HF radar sites are deployed along the coastline to extend HF radar coverage between $32.5°$ and $33.5°$ N, a more appropriate comparison to Lee et al.'s (1991) measurements could be made.

Finally, the momentum flux across the shelf is correlated to the Florida Current transport $(R^2 \approx 0.2)$ but more strongly correlated to eddies near the shelf break $(R^2 \approx 0.4)$. There is significant momentum flux (offshore flux of momentum to the GS) during the passage of an anticyclonic eddy. Although the momentum flux corresponds to the subtidal eddies identified herein, future studies should also consider more transient (short lived) shelf break eddies that can be spun up during tidal cycles and contribute to cross shelf momentum flux (Savidge et al., 2010).

CHAPTER 5

CONCLUSION

We introduced the HF radar system and surface current estimates that these systems provide in Chapter 1, along with three areas of research that are critical: Increasing the accuracy of HF radar surface current estimates via implementing direction finding routines for linear array HF radar systems (Chapter 2), understanding the fundamental physics of ocean waves (what their phase speed is) and therefore what the HF radar measurement is (Chapter 3) and a contribution of an easily implemented technique to identify eddies which has been optimized for use on HF radar data sets (Chapter 4). In Chapter 2, we assess three different algorithms that can be used for HF radar systems to identify where (which direction) it is measuring ocean currents from. In Chapter 3, we address the underlying principle that is used to estimate ocean currents using HF radars (the phase speed of ocean waves and how it is affected by Stokes drift). After optimizing both the HF radar processing algorithm (Chapter 2) and gaining some insight into the actual phase speed of the ocean waves that HF radars measure (Chapter 3). Finally, in Chapter 4 an optimized eddy identification algorithm was presented for use with HF radar data. In this Chapter we briefly review the findings in Chapter 2-4, discuss their possible benefits to the field and our opinion future research along these three research paths (Chapters 2-4).

In Chapter 2 HF radar algorithms were compared and the application of MUSIC and Beamscan to beamforming linear array systems was described. An open source algorithm for MUSIC, Beamscan and beamforming were developed with the goal of easy implementation of all three algorithms to other HF radar systems (specifically targeting beamforming linear array HF radar systems, but they may also be used for grid arrays with slight modification to the code). The analysis showed that all three algorithms

(Beamforming, Beamscan and MUSIC) perform well and similarly at a location near the boresight of the HF radars, however, significant differences between the methods occur at locations significantly far from the radar boresights ($> 40°$), especially during times when there is significantly more wave energy near the radar boresights that far from the boresight, or when some of the receiving antennas are performing poorly. During these times, the scattered HF radar signal from near the boresights is very strong and overwhelms the beamforming algorithm to this when 'looking' at locations far from the radar boresights. Therefore, beamforming mistakenly still 'sees' the signal near the radar boresights when trying to calculate the surface current far from the boresights, which results in erroneous surface current estimates. It was found that during these sea states the surface current estimates far from the radar boresights correlate to the signal near the radar boresights and not the surface current at the intended location ($> 40°$ from the radar boresight).

Both Beamscan and MUSIC are direction finding routines, and therefore, effectively suppress all the energy from near the radar boresights if it is a different frequency than that far from the boresights. This allows the smaller scattered energy far from the boresights to be detected. If the surface currents were identical at both locations (and therefore the scattered return signal would have the same frequency at both locations) Beamscan would suffer the same problems as Beamforming does, described above. Since this was not the case in our study, Beamscan outperformed MUSIC and did not require as significant tuning/optimization as MUSIC does. For future research applications, we suggest that Beamscan can be easily implemented in other linear array

HF radar systems and differences between Beamscan and Beamforming may alert the HF radar operator to areas containing erroneous or inaccurate surface current estimates.

Regarding MUSIC, the radar systems used here use 15 minute acquisitions to estimate the surface currents, while systems designed for MUSIC generally use 30-60 minutes, as MUSIC requires more samples than Beamforming or Beamscan. Therefore, it is premature to claim that Beamscan is ‘better’ than MUSIC on the linear array HF radar systems used here. For future research we see optimizing music for linear array HF radars with longer acquisition times and detailed optimization parameters for different HF radar site locations published in order to make implementing MUSIC on these systems easier for the HF radar operators as an important contribution to increase the accuracy of HF radar surface current measurements.

In Chapter 3 we assess a fundamental ocean physics question, what is the phase speed of an ocean wave in the ocean (i.e., surrounded by other waves that all contribute to Stokes’ drift). The analysis surmised that previously published results suggesting that there is no effect on the phase speed (REF), or that to the phase speed includes the full surface Stokes’ drift (REF). are both flawed. The two most commonly assessed effects, ‘filtered Stokes drift’ and ‘effective Stokes drift’, which vary depending on the wavelength both seem to offer an explanation of the previously published results; the phase speed of very short waves (e.g., Bragg waves measured by 50 Mhz HF radar systems) include the full surface Stokes drift while very long waves (e.g., Bragg waves measured by 5 MHz HF radar systems) don’t include any.

After theoretical calculations of the three most commonly suggested additions to the phase speed of the Bragg wave (filtered Stokes drift, effective Stokes drift and half surface Stokes drift) and how these relate to different wave spectra (theoretical wave spectra using different wind speeds) and different HF radar operating frequencies, we assess their validity by comparing the HF radar surface current measurements to measurements from in situ current measurements. The location of the in situ current measurements is near the radar boresights, which in Chapter 2 we showed to be a location where the HF radar system provided highly accurate surface current estimates. Using wave spectra provided by a wave model, we found that filtered Stokes drift could explain over 60% of the difference between the HF radar surface current estimate and the in situ measurements when significant wave heights were greater than 2 meters.

Since wave spectra measurements are not always available for HF radar site operators, and since wave spectra estimates from HF radar systems cover a much smaller area than surface current estimates, we provide a methodology to estimate the filtered Stokes' drift term directly from HF radars using the first order Bragg peaks from both radar sites (the same Bragg peaks used to estimate the surface currents). We follow a similar methodology of that used for wind estimates from HF radar systems by training a neural network. The trained neural network was able to estimate the filtered Stokes' drift term at almost the same level of accuracy as using the wave model, capable of explaining just over 50% of the difference between the HF radar surface current estimates and the in situ measurements when significant wave heights were over 2 meters.

In Chapter 3 we also suggest future paths of research and that HF radar systems which measure the phase speed of Bragg waves cover the range of wavelengths where filtered Stokes and effective Stokes drift have the most variation in terms of percentage of total surface Stokes drift. Dedicated long term studies in areas where significant wave heights are greater 2 meters and where there are times of significant swell, combined with HF radar systems operating across multiple frequency bands (and therefore measure the phase speed of a large range of different Bragg wavelengths) should be able to tease apart the two most favorable phase speed correction terms, filtered Stokes drift and effective Stokes drift, and identify which is correct. Since estimating surface currents by measuring the phase speed of ocean waves is increasing in popularity, not only are HF radar sites expanding, but satellite systems, aerial video systems and X-band radar systems using this methodology are also becoming common place, we feel this is an important area of research that is needed to provide accurate surface current estimates across oceanographic research and operational oceanography.

In Chapter 4 we optimize an eddy identification algorithm for use on HF radar surface current data. After optimizing the winding-angle algorithm to detect eddies in the HF radar data set, we identify the Charleston Gyre (CG) just offshore of the shelf break in Long Bay, SC. Although the HF radar data availability is below 50% in this area, and the CG cannot be identified continuously, we are able to track it at up to 4 days at a time. We find its propagation can be in any direction and that it propagates at <.2 m/s. Its position is highly variable and correlates to the position of the Gulf Stream (GS). The GS can be highly deflected offshore just after it passes the Charleston Bump or only slightly deflected. When the GS is highly deflected offshore the CG is located significantly far from the shelf break while when the GS is only slightly deflected the CG is almost against the shelf break near the 100 m isobath.

HF radar data availability is greater than 50% near the shelf break and here we focus on smaller eddies identified near the shelf break. We find a majority of anticyclonic eddies near the shelf break that correlate to momentum flux across the shelf break. Although the monthly mean speed of the GS (measured at the Florida straits) correlates to momentum flux across the shelf break in Long Bay, SC with $R^2 \approx 0.2$ we show that the number of anticyclonic eddies near the shelf break correlate at higher level $(R^2 \approx 0.4)$. Additionally, we track an anticyclonic eddy as it propagates near the shelf break and show that the momentum flux across the shelf break coincides with the position of this eddy. Finally, we find that these shelf break eddies are not correlated to the tidal phase but instead correlate to northerly winds, which induces Ekman transport in the preferred propagation direction of the shelf break eddies (towards the southwest).

We remark on the difficulties in eddy identification and tracking in HF radar data sets, where data availability may be low, and in this area where eddies may differ in size by more than an order of magnitude, with eddy diameters ranging from roughly 5 km to well over 50 km. Although size and shape analysis is difficult with the large range of eddy sizes in this area, and additionally, the strong convergence seen in the CG, we are still able to accurately identify the eddies. We suggest using this optimized winding-angle algorithm to produce data sets for training neural network methods of eddy identification and hope that this tool is a useful method that can reduce manually training neural networks for eddy identification.

In this thesis we addressed three areas of research that we feel are key areas in the oceanographic community. In Chapter 2, we focus on increasing the accuracy and reliability of HF radar surface current estimates and provide future studies and future HF radar systems the ability to implement these algorithms in order to identify areas where these systems may be providing inaccurate surface current estimates. We feel this contribution is important in two ways, first to identify locations where surface currents may be inaccurate, and we also show that using Beamscan (the easiest direction finding implementation) can provide more accurate surface current far from the radar boresight during certain sea states. In Chapter 3, we address a fundamental ocean physics question that remote systems exploit to estimate surface ocean currents. We feel this is a key research topic not only for fundamental research but also as these remote measuring systems proliferate, it is important to know what the surface current measurements actually are and how much Stokes' drift is included in the measurement, especially for predicting trajectories for surface objects on time scales greater than one day. Finally, in Chapter 4, we optimize an eddy identification routine for HF radar systems and show the important factors that eddies contribute to, in this case, momentum flux across the shelf break. Additionally, we hope this optimized method can be used as a basis for further advancement in eddy identification (providing automated training data for neural networks) in surface current data sets.

REFERENCES

Alattabi, Z. R., D. Cahl, and G. Voulgaris, 2019: Swell and Wind Wave Inversion Using a Single Very High Frequency (VHF) Radar. *Journal of Atmospheric and Oceanic Technology*, **36**, 987–1013, https://doi.org/10.1175/JTECH-D-18-0166.1.

Al-Attabi, Z. R., G. Voulgaris, and D. C. Conley, 2021a: Evaluation and Validation of HF Radar Swell and Wind wave Inversion Method. *Journal of Atmospheric and Oceanic Technology*, https://doi.org/10.1175/JTECH-D-20-0186.1.

——, ——, and ——, 2021b: Evaluation and Validation of HF Radar Swell and Wind wave Inversion Method. *Journal of Atmospheric and Oceanic Technology*, https://doi.org/10.1175/JTECH-D-20-0186.1.

Anstead, K. A., and Coauthors, 2021a: The Path to an Ecosystem Approach for Forage Fish Management: A Case Study of Atlantic Menhaden. *Front. Mar. Sci.*, **8**, 607657, https://doi.org/10.3389/fmars.2021.607657.

——, and Coauthors, 2021b: The Path to an Ecosystem Approach for Forage Fish Management: A Case Study of Atlantic Menhaden. *Front. Mar. Sci.*, **8**, 607657, https://doi.org/10.3389/fmars.2021.607657.

Ardhuin, F., L. Marié, N. Rascle, P. Forget, and A. Roland, 2009: Observation and Estimation of Lagrangian, Stokes, and Eulerian Currents Induced by Wind and Waves at the Sea Surface. *Journal of Physical Oceanography*, **39**, 2820–2838, https://doi.org/10.1175/2009JPO4169.1.

——, and Coauthors, 2019: SKIM, a Candidate Satellite Mission Exploring Global Ocean Currents and Waves. *Front. Mar. Sci.*, **6**, 209, https://doi.org/10.3389/fmars.2019.00209.

Ari Sadarjoen, I., and F. H. Post, 2000a: Detection, quantification, and tracking of vortices using streamline geometry. *Computers & Graphics*, **24**, 333–341, https://doi.org/10.1016/S0097-8493(00)00029-7.

——, and ——, 2000b: Detection, quantification, and tracking of vortices using streamline geometry. *Computers & Graphics*, **24**, 333–341, https://doi.org/10.1016/S0097-8493(00)00029-7.

Bagaglini, L., P. Falco, and E. Zambianchi, 2019: Eddy Detection in HF Radar-Derived Surface Currents in the Gulf of Naples. *Remote Sensing*, **12**, 97, https://doi.org/10.3390/rs12010097.

Bane, J. M., and W. K. Dewar, 1988: Gulf Stream bimodality and variability downstream of the Charleston bump. *J. Geophys. Res.*, **93**, 6695, https://doi.org/10.1029/JC093iC06p06695.

Barrick, D. E., and B. L. Weber, 1977: On the Nonlinear Theory for Gravity Waves on the Ocean's Surface. Part II: Interpretation and Applications. *J. Phys. Oceanogr.*, **7**, 11–21, https://doi.org/10.1175/1520-0485(1977)007<0011:OTNTFG>2.0.CO;2.

Bellomo, L., and Coauthors, 2015: Toward an integrated HF radar network in the Mediterranean Sea to improve search and rescue and oil spill response: the TOSCA project experience. *Journal of Operational Oceanography*, **8**, 95–107, https://doi.org/10.1080/1755876X.2015.1087184.

Blanton, B. O., 2003: Monthly climatology of the continental shelf waters of the South Atlantic Bight. *J. Geophys. Res.*, **108**, 3264, https://doi.org/10.1029/2002JC001609.

Booij, N., R. C. Ris, and L. H. Holthuijsen, 1999: A third-generation wave model for coastal regions: 1. Model description and validation. *J. Geophys. Res.*, **104**, 7649–7666, https://doi.org/10.1029/98JC02622.

Breivik, Ø., A. A. Allen, C. Maisondieu, and M. Olagnon, 2013: Advances in search and rescue at sea. *Ocean Dynamics*, **63**, 83–88, https://doi.org/10.1007/s10236-012-0581-1.

van den Bremer, T. S., and Ø. Breivik, 2018: Stokes drift. *Phil. Trans. R. Soc. A.*, **376**, 20170104, https://doi.org/10.1098/rsta.2017.0104.

Brooks, D. A., and J. M. Bane, 1978: Gulf Stream Deflection by a Bottom Feature off Charleston, South Carolina. *Science*, **201**, 1225–1226, https://doi.org/10.1126/science.201.4362.1225.

Bushnell, M., R. Heitsenrether, J. Thomas, C. Galvarino, E. Burger, J. Dorton, and L. Leonard, 2018: Status and Near-Term Plans for the U.S. IOOS Quality Assurance / Quality Control of Real-time Oceanographic Data (QARTOD) Project. *OCEANS 2018 MTS/IEEE Charleston*, Charleston, SC, IEEE, 1–6.

Cahl, D., and G. Voulgaris, 2015: Sub-mesoscale Eddies and Their Propagation Paths in Long Bay, SC Observed in HF Radar Surface Currents. **2015**, OS11A-1987.

Cahl, D., G. Voulgaris, and L. Leonard, 2022: A Comparison of Beamforming and Direction Finding Algorithms (Beamscan and MUSIC) on a Linear Array HF Radar in a Medium to Low Wave Energy Environment. *Journal of Atmospheric and Oceanic Technology*, https://doi.org/10.1175/JTECH-D-22-0005.1.

——, ——, and ——, 2023: A Comparison of Beamforming and Direction Finding Algorithms (Beamscan and MUSIC) on a Linear Array HF Radar in a Medium to Low Wave Energy Environment. *Journal of Atmospheric and Oceanic Technology*, **40**, 191–218, https://doi.org/10.1175/JTECH-D-22-0005.1.

Cai, J., H. Zhou, W. Huang, and B. Wen, 2021: Ship Detection and Direction Finding Based on Time-Frequency Analysis for Compact HF Radar. *IEEE Geosci. Remote Sensing Lett.*, **18**, 72–76, https://doi.org/10.1109/LGRS.2020.2967387.

Chapman, R., and H. Graber, 1997a: Validation of HF Radar Measurements. *oceanog*, **10**, https://doi.org/10.5670/oceanog.1997.28.
Chapman, R. D., and H. C. Graber, 1997b: Validation of HF Radar Measurements. *Oceanography*, **10**, 76–79.

Chapman, R. D., L. K. Shay, H. C. Graber, J. B. Edson, A. Karachintsev, C. L. Trump, and D. B. Ross, 1997: On the accuracy of HF radar surface current measurements: Intercomparisons with ship-based sensors. *J. Geophys. Res.*, **102**, 18737–18748, https://doi.org/10.1029/97JC00049.

Chavanne, C., 2018: Do High-Frequency Radars Measure the Wave-Induced Stokes Drift? *Journal of Atmospheric and Oceanic Technology*, **35**, 1023–1031, https://doi.org/10.1175/JTECH-D-17-0099.1.

Churchill, J. H., and G. T. Csanady, 1983: Near-Surface Measurements of Quasi-Lagrangian Velocities in Open Water. *J. Phys. Oceanogr.*, **13**, 1669–1680, https://doi.org/10.1175/1520-0485(1983)013<1669:NSMOQL>2.0.CO;2.

Crombie, D. D., 1955a: Doppler Spectrum of Sea Echo at 13.56 Mc./s. *Nature*, **175**, 681–682, https://doi.org/10.1038/175681a0.

——, 1955b: Doppler Spectrum of Sea Echo at 13.56 Mc./s. *Nature*, **175**, 681–682, https://doi.org/10.1038/175681a0.

Dugan, J. P., C. C. Piotrowski, and J. Z. Williams, 2001: Water depth and surface current retrievals from airborne optical measurements of surface gravity wave dispersion. *J. Geophys. Res.*, **106**, 16903–16915, https://doi.org/10.1029/2000JC000369.

Dussol, A., C. Chavanne, S. Gregorio, and D. Dumont, 2022: Experimental Confirmation of Stokes Drift Measurement by High-Frequency Radars. *Journal of Atmospheric and Oceanic Technology*, **39**, 1541–1559, https://doi.org/10.1175/JTECH-D-21-0025.1.

Essen, H.-H., K.-W. Gurgel, and T. Schlick, 1999: Measurement of ocean wave height and direction by means of HF radar: An empirical approach. *Deutsche Hydrographische Zeitschrift*, **51**, 369–383, https://doi.org/10.1007/BF02764161.

Essen, H.-H., K.-W. Gurgel, and T. Schlick, 2000: On the accuracy of current measurements by means of HF radar. *IEEE J. Oceanic Eng.*, **25**, 472–480, https://doi.org/10.1109/48.895354.

Falcon, E., and N. Mordant, 2022: Experiments in Surface Gravity–Capillary Wave Turbulence. *Annu. Rev. Fluid Mech.*, **54**, 1–25, https://doi.org/10.1146/annurev-fluid-021021-102043.

Fernandez, D. M., J. F. Vesecky, and C. C. Teague, 1996: Measurements of upper ocean surface current shear with high-frequency radar. *J. Geophys. Res.*, **101**, 28615–28625, https://doi.org/10.1029/96JC03108.
Ferrari, R., and C. Wunsch, 2009: Ocean Circulation Kinetic Energy: Reservoirs, Sources, and Sinks. *Annu. Rev. Fluid Mech.*, **41**, 253–282, https://doi.org/10.1146/annurev.fluid.40.111406.102139.

Gemmrich, J. R., and D. M. Farmer, 2004: Near-Surface Turbulence in the Presence of Breaking Waves. *J. Phys. Oceanogr.*, **34**, 1067–1086, https://doi.org/10.1175/1520-0485(2004)034<1067:NTITPO>2.0.CO;2.

Govoni, J. J., J. A. Hare, E. D. Davenport, M. H. Chen, and K. E. Marancik, 2010: Mesoscale, cyclonic eddies as larval fish habitat along the southeast United States shelf: a Lagrangian description of the zooplankton community. *ICES Journal of Marine Science*, **67**, 403–411, https://doi.org/10.1093/icesjms/fsp269.

——, ——, and ——, 2013: The Distribution of Larval Fishes of the Charleston Gyre Region off the Southeastern United States in Winter Shaped by Mesoscale, Cyclonic Eddies. *Marine and Coastal Fisheries*, **5**, 246–259, https://doi.org/10.1080/19425120.2013.820245.

Gurgel, K.-W., G. Antonischki, H.-H. Essen, and T. Schlick, 1999a: Wellen Radar (WERA): a new ground-wave HF radar for ocean remote sensing. *Coastal Engineering*, **37**, 219–234, https://doi.org/10.1016/S0378-3839(99)00027-7.

——, ——, ——, and ——, 1999b: Wellen Radar (WERA): a new ground-wave HF radar for ocean remote sensing. *Coastal Engineering*, **37**, 219–234, https://doi.org/10.1016/S0378-3839(99)00027-7.

——, H.-H. Essen, and S. P. Kingsley, 1999c: High-frequency radars: physical limitations and recent developments. *Coastal Engineering*, **37**, 201–218, https://doi.org/10.1016/S0378-3839(99)00026-5.

Gurgel, K.-W., H.-H. Essen, and T. Schlick, 2006: An Empirical Method to Derive Ocean Waves From Second-Order Bragg Scattering: Prospects and Limitations. *IEEE J. Oceanic Eng.*, **31**, 804–811, https://doi.org/10.1109/JOE.2006.886225.

Hanson, B., K. Klink, K. Matsuura, S. M. Robeson, and C. J. Willmott, 1992: Vector Correlation: Review, Exposition, and Geographic Application. *Annals of the Association of American Geographers*, **82**, 103–116, https://doi.org/10.1111/j.1467-8306.1992.tb01900.x.

Harlan, J., and Coauthors, 2011: National IOOS high frequency radar search and rescue project. *OCEANS'11 MTS/IEEE KONA*, Waikoloa, HI, IEEE, 1–9.

Hasselmann, D. E., M. Dunckel, and J. A. Ewing, 1980: Directional Wave Spectra Observed during JONSWAP 1973. *J. Phys. Oceanogr.*, **10**, 1264–1280, https://doi.org/10.1175/1520-0485(1980)010<1264:DWSODJ>2.0.CO;2.

Hasselmann, K., 1971: Determination of Ocean Wave Spectra from Doppler Radio Return from the Sea Surface. *Nature Physical Science*, **229**, 16–17, https://doi.org/10.1038/physci229016a0.

——, and Coauthors, 1973: Measurements of wind-wave growth and swell decay during the Joint North Sea Wave Project (JONSWAP). *Ergänzungsheft 8-12*,.
Hildebrand, P. H., and R. S. Sekhon, 1974: Objective Determination of the Noise Level in Doppler Spectra. *J. Appl. Meteor.*, **13**, 808–811, https://doi.org/10.1175/1520-0450(1974)013<0808:ODOTNL>2.0.CO;2.

Hsu, A. C., A. M. Boustany, J. J. Roberts, J. Chang, and P. N. Halpin, 2015: Tuna and swordfish catch in the U.S. northwest Atlantic longline fishery in relation to mesoscale eddies. *Fisheries Oceanography*, **24**, 508–520, https://doi.org/10.1111/fog.12125.

Huang, W., X. Liu, and E. Gill, 2017: Ocean Wind and Wave Measurements Using X-Band Marine Radar: A Comprehensive Review. *Remote Sensing*, **9**, 1261, https://doi.org/10.3390/rs9121261.

Ivonin, D. V., 2004: Validation of HF radar probing of the vertical shear of surface currents by acoustic Doppler current profiler measurements. *J. Geophys. Res.*, **109**, C04003, https://doi.org/10.1029/2003JC002025.

——, V. I. Shrira, and P. Broche, 2006: On the Singular Nature of the Second-Order Peaks in HF Radar Sea Echo. *IEEE J. Oceanic Eng.*, **31**, 751–767, https://doi.org/10.1109/JOE.2006.886080.

Justusson, B. I., 1981: Median Filtering: Statistical Properties. *Two-Dimensional Digital Signal Prcessing II*, Vol. 43 of, Springer-Verlag, 161–196.

Kenyon, K. E., 1969: Stokes drift for random gravity waves. *J. Geophys. Res.*, **74**, 6991–6994, https://doi.org/10.1029/JC074i028p06991.

Kirincich, A., 2016: Remote Sensing of the Surface Wind Field over the Coastal Ocean via Direct Calibration of HF Radar Backscatter Power. *Journal of Atmospheric and Oceanic Technology*, **33**, 1377–1392, https://doi.org/10.1175/JTECH-D-15-0242.1.

Kirincich, A. R., T. de Paolo, and E. Terrill, 2012: Improving HF Radar Estimates of Surface Currents Using Signal Quality Metrics, with Application to the MVCO High-Resolution Radar System. *Journal of Atmospheric and Oceanic Technology*, **29**, 1377–1390, https://doi.org/10.1175/JTECH-D-11-00160.1.

Kuang, L., A. F. Blumberg, and N. Georgas, 2012: Assessing the fidelity of surface currents from a coastal ocean model and HF radar using drifting buoys in the Middle Atlantic Bight. *Ocean Dynamics*, **62**, 1229–1243, https://doi.org/10.1007/s10236-012-0556-2.

Kudryavtsev, V., V. Shrira, V. Dulov, and V. Malinovsky, 2008: On the Vertical Structure of Wind-Driven Sea Currents. *Journal of Physical Oceanography*, **38**, 2121–2144, https://doi.org/10.1175/2008JPO3883.1.

Kumar, N., G. Voulgaris, J. C. Warner, and M. Olabarrieta, 2012: Implementation of the vortex force formalism in the coupled ocean-atmosphere-wave-sediment transport (COAWST) modeling system for inner shelf and surf zone applications. *Ocean Modelling*, **47**, 65–95, https://doi.org/10.1016/j.ocemod.2012.01.003.

——, D. L. Cahl, S. C. Crosby, and G. Voulgaris, 2017: Bulk versus Spectral Wave Parameters: Implications on Stokes Drift Estimates, Regional Wave Modeling, and HF Radars Applications. *Journal of Physical Oceanography*, **47**, 1413–1431, https://doi.org/10.1175/JPO-D-16-0203.1.

Lai, Y., H. Zhou, Y. Zeng, and B. Wen, 2017: Quantifying and Reducing the DOA Estimation Error Resulting from Antenna Pattern Deviation for Direction-Finding HF Radar. *Remote Sensing*, **9**, 1285, https://doi.org/10.3390/rs9121285.

Largier, J. L., 2003: CONSIDERATIONS IN ESTIMATING LARVAL DISPERSAL DISTANCES FROM OCEANOGRAPHIC DATA. *Ecological Applications*, **13**, 71–89, https://doi.org/10.1890/1051-0761(2003)013[0071:CIELDD]2.0.CO;2.

Laws, K. E., D. M. Fernandez, and J. D. Paduan, 2000: Simulation-based evaluations of HF radar ocean current algorithms. *IEEE J. Oceanic Eng.*, **25**, 481–491, https://doi.org/10.1109/48.895355.

Laxague, N. J. M., and Coauthors, 2018: Observations of Near-Surface Current Shear Help Describe Oceanic Oil and Plastic Transport: VERY NEAR SURFACE CURRENT SHEAR. *Geophys. Res. Lett.*, **45**, 245–249, https://doi.org/10.1002/2017GL075891.

Lee, T. N., J. A. Yoder, and L. P. Atkinson, 1991: Gulf Stream frontal eddy influence on productivity of the southeast U.S. continental shelf. *J. Geophys. Res.*, **96**, 22191, https://doi.org/10.1029/91JC02450.

Lenain, L., and N. Pizzo, 2020: The Contribution of High-Frequency Wind-Generated Surface Waves to the Stokes Drift. *Journal of Physical Oceanography*, **50**, 3455–3465, https://doi.org/10.1175/JPO-D-20-0116.1.

Lipa, B. J., and D. E. Barrick, 1986: Extraction of sea state from HF radar sea echo: Mathematical theory and modeling. *Radio Sci.*, **21**, 81–100, https://doi.org/10.1029/RS021i001p00081.

Liu, F., H. Zhou, and B. Wen, 2020: DEDNet: Offshore Eddy Detection and Location with HF Radar by Deep Learning. *Sensors*, **21**, 126, https://doi.org/10.3390/s21010126.

Liu, Y., R. H. Weisberg, and C. R. Merz, 2014: Assessment of CODAR SeaSonde and WERA HF Radars in Mapping Surface Currents on the West Florida Shelf*. *Journal of Atmospheric and Oceanic Technology*, **31**, 1363–1382, https://doi.org/10.1175/JTECH-D-13-00107.1.

Longuet-Higgins, M. S., and O. M. Phillips, 1962: Phase velocity effects in tertiary wave interactions. *J. Fluid Mech.*, **12**, 333–336, https://doi.org/10.1017/S0022112062000245.

Lund, B., H. C. Graber, H. Tamura, C. O. Collins, and S. M. Varlamov, 2015: A new technique for the retrieval of near-surface vertical current shear from marine X -band radar images. *J. Geophys. Res. Oceans*, **120**, 8466–8486, https://doi.org/10.1002/2015JC010961.

Mantovani, C., and Coauthors, 2020: Best Practices on High Frequency Radar Deployment and Operation for Ocean Current Measurement. *Front. Mar. Sci.*, **7**, 210, https://doi.org/10.3389/fmars.2020.00210.

Mao, Y., and M. L. Heron, 2008: The Influence of Fetch on the Response of Surface Currents to Wind Studied by HF Ocean Surface Radar. *Journal of Physical Oceanography*, **38**, 1107–1121, https://doi.org/10.1175/2007JPO3709.1.

McClain, C. R., and L. P. Atkinson, 1985: A note on the Charleston Gyre. *J. Geophys. Res.*, **90**, 11857, https://doi.org/10.1029/JC090iC06p11857.

Mujiasih, S., D. Hartanto, J.-M. Beckers, and A. Barth, 2021: Reducing the error in estimates of the Sunda Strait currents by blending HF radar currents with model results. *Continental Shelf Research*, **228**, 104512, https://doi.org/10.1016/j.csr.2021.104512.

Nencioli, F., C. Dong, T. Dickey, L. Washburn, and J. C. McWilliams, 2010: A Vector Geometry–Based Eddy Detection Algorithm and Its Application to a High-Resolution Numerical Model Product and High-Frequency Radar Surface Velocities in the Southern

California Bight. *Journal of Atmospheric and Oceanic Technology*, **27**, 564–579, https://doi.org/10.1175/2009JTECHO725.1.

Okubo, A., 1970: Horizontal dispersion of floatable particles in the vicinity of velocity singularities such as convergences. *Deep Sea Research and Oceanographic Abstracts*, **17**, 445–454, https://doi.org/10.1016/0011-7471(70)90059-8.

Paduan, J. D., and L. Washburn, 2013a: High-Frequency Radar Observations of Ocean Surface Currents. *Annu. Rev. Mar. Sci.*, **5**, 115–136, https://doi.org/10.1146/annurev-marine-121211-172315.

——, and ——, 2013b: High-Frequency Radar Observations of Ocean Surface Currents. *Annu. Rev. Mar. Sci.*, **5**, 115–136, https://doi.org/10.1146/annurev-marine-121211-172315.
Richman, J. G., R. A. De Szoeke, and R. E. Davis, 1987: Measurements of near-surface shear in the ocean. *J. Geophys. Res.*, **92**, 2851, https://doi.org/10.1029/JC092iC03p02851.

Röhrs, J., A. K. Sperrevik, K. H. Christensen, G. Broström, and Ø. Breivik, 2015: Comparison of HF radar measurements with Eulerian and Lagrangian surface currents. *Ocean Dynamics*, **65**, 679–690, https://doi.org/10.1007/s10236-015-0828-8.

Rubio, A., and Coauthors, 2017: HF Radar Activity in European Coastal Seas: Next Steps toward a Pan-European HF Radar Network. *Front. Mar. Sci.*, **4**, https://doi.org/10.3389/fmars.2017.00008.

Savidge, D. K., J. Norman, C. Smith, J. A. Amft, T. Moore, C. Edwards, and G. Voulgaris, 2010: Shelf edge tide correlated eddies along the southeastern United States: SETC EDDIES. *Geophys. Res. Lett.*, **37**, n/a-n/a, https://doi.org/10.1029/2010GL045236.

Schaeffer, A., A. Gramoulle, M. Roughan, and A. Mantovanelli, 2017: Characterizing frontal eddies along the E ast A ustralian C urrent from HF radar observations. *JGR Oceans*, **122**, 3964–3980, https://doi.org/10.1002/2016JC012171.

Schmidt, R., 1986: Multiple emitter location and signal parameter estimation. *IEEE Trans. Antennas Propagat.*, **34**, 276–280, https://doi.org/10.1109/TAP.1986.1143830.

Sentchev, A., P. Forget, and P. Fraunié, 2017: Surface current dynamics under sea breeze conditions observed by simultaneous HF radar, ADCP and drifter measurements. *Ocean Dynamics*, **67**, 499–512, https://doi.org/10.1007/s10236-017-1035-6.

Shchepetkin, A. F., and J. C. McWilliams, 2005: The regional oceanic modeling system (ROMS): a split-explicit, free-surface, topography-following-coordinate oceanic model. *Ocean Modelling*, **9**, 347–404, https://doi.org/10.1016/j.ocemod.2004.08.002.

Shen, W., K.-W. Gurgel, G. Voulgaris, T. Schlick, and D. Stammer, 2012: Wind-speed inversion from HF radar first-order backscatter signal. *Ocean Dynamics*, **62**, 105–121, https://doi.org/10.1007/s10236-011-0465-9.

Shrira, V. I., D. V. Ivonin, P. Broche, and J. C. de Maistre, 2001: On remote sensing of vertical shear of ocean surface currents by means of a Single-frequency VHF radar. *Geophys. Res. Lett.*, **28**, 3955–3958, https://doi.org/10.1029/2001GL013387.

Smeltzer, B. K., E. Æsøy, A. Ådnøy, and S. Å. Ellingsen, 2019: An Improved Method for Determining Near-Surface Currents From Wave Dispersion Measurements. *J. Geophys. Res. Oceans*, **124**, 8832–8851, https://doi.org/10.1029/2019JC015202.

Stewart, R. H., and J. W. Joy, 1974: HF radio measurements of surface currents. *Deep Sea Research and Oceanographic Abstracts*, **21**, 1039–1049, https://doi.org/10.1016/0011-7471(74)90066-7.
Streser, M., R. Carrasco, and J. Horstmann, 2017: Video-Based Estimation of Surface Currents Using a Low-Cost Quadcopter. *IEEE Geosci. Remote Sensing Lett.*, **14**, 2027–2031, https://doi.org/10.1109/LGRS.2017.2749120.

Teague, C., 1986: Multifrequency HF radar observations of currents and current shears. *IEEE J. Oceanic Eng.*, **11**, 258–269, https://doi.org/10.1109/JOE.1986.1145178.

Ullman, D. S., J. O'Donnell, J. Kohut, T. Fake, and A. Allen, 2006: Trajectory prediction using HF radar surface currents: Monte Carlo simulations of prediction uncertainties. *J. Geophys. Res.*, **111**, C12005, https://doi.org/10.1029/2006JC003715.

Van Der Mheen, M., C. Pattiaratchi, S. Cosoli, and M. Wandres, 2020: Depth-Dependent Correction for Wind-Driven Drift Current in Particle Tracking Applications. *Front. Mar. Sci.*, **7**, 305, https://doi.org/10.3389/fmars.2020.00305.

Voulgaris, G., B. K. Haus, P. Work, L. K. Shay, H. E. Seim, R. H. Weisberg, and J. R. Nelson, 2008: Waves Initiative within SEACOOS. *mar technol soc j*, **42**, 68–80, https://doi.org/10.4031/002533208786842507.

Wang, W., P. Forget, and C. Guan, 2014: Inversion of swell frequency from a 1-year HF radar dataset collected in Brittany (France). *Ocean Dynamics*, **64**, 1447–1456, https://doi.org/10.1007/s10236-014-0759-9.

Warner, J. C., B. Armstrong, R. He, and J. B. Zambon, 2010: Development of a Coupled Ocean–Atmosphere–Wave–Sediment Transport (COAWST) Modeling System. *Ocean Modelling*, **35**, 230–244, https://doi.org/10.1016/j.ocemod.2010.07.010.

Weber, B. L., and D. E. Barrick, 1977: On the Nonlinear Theory for Gravity Waves on the Ocean's Surface. Part I: Derivations. *J. Phys. Oceanogr.*, **7**, 3–10, https://doi.org/10.1175/1520-0485(1977)007<0003:OTNTFG>2.0.CO;2.

Weiss, J., 1991: The dynamics of enstrophy transfer in two-dimensional hydrodynamics. *Physica D: Nonlinear Phenomena*, **48**, 273–294, https://doi.org/10.1016/0167-2789(91)90088-Q.

Wu, X., G. Voulgaris, and N. Kumar, 2017: Parameterization of synoptic weather systems in the South Atlantic Bight for modeling applications. *Ocean Dynamics*, **67**, 1231–1249, https://doi.org/10.1007/s10236-017-1084-x.

Wyatt, L. R., G. Liakhovetski, H. C. Graber, and B. K. Haus, 2005: Factors Affecting the Accuracy of SHOWEX HF Radar Wave Measurements. *Journal of Atmospheric and Oceanic Technology*, **22**, 847–859, https://doi.org/10.1175/JTECH1728.1.

——, J. J. Green, A. Middleditch, M. D. Moorhead, J. Howarth, M. Holt, and S. Keogh, 2006: Operational Wave, Current, and Wind Measurements With the Pisces HF Radar. *IEEE J. Oceanic Eng.*, **31**, 819–834, https://doi.org/10.1109/JOE.2006.888378.

Zeng, Y., H. Zhou, H. Roarty, and B. Wen, 2016: Wind Speed Inversion in High Frequency Radar Based on Neural Network. *International Journal of Antennas and Propagation*, **2016**, 1–8, https://doi.org/10.1155/2016/2706521.